Title
Probing Inflation from the South Pole: A Measurement of the B-mode Polarization of the Cosmic Microwave Background with SPT-3G

Author
Zebrowski, Jessica Avva

Publication Date
2022

Peer reviewed|Thesis/dissertation

Probing Inflation from the South Pole: A Measurement of the B-mode Polarization of the Cosmic Microwave Background with SPT-3G

by

Jessica Avva Zebrowski

A dissertation submitted in partial satisfaction of the

requirements for the degree of

Doctor of Philosophy

in

Physics

in the

Graduate Division

of the

University of California, Berkeley

Committee in charge:

Professor William Holzapfel, Chair
Professor Adrian Lee
Professor Martin White

Fall 2022

Probing Inflation from the South Pole: A Measurement of the B-mode Polarization of the Cosmic Microwave Background with SPT-3G

Abstract

Probing Inflation from the South Pole: A Measurement of the B-mode Polarization of the Cosmic Microwave Background with SPT-3G

by

Jessica Avva Zebrowski

Doctor of Philosophy in Physics

University of California, Berkeley

Professor William Holzapfel, Chair

The Cosmic Microwave Background, the oldest light in the universe, provides a powerful tool to test the theory of inflation and constrain the standard ΛCDM cosmological model. The theory of inflation describes a period of rapid, exponential growth in the early Universe. A measurement of r, the tensor-to-scalar ratio of CMB polarization, would provide evidence for inflation and measure its energy scale. However, this is an extremely difficult measurement to make due to the faintness of the signal. Historically, Small Aperture Telescopes (SATs) have been used to constraint inflation. However, there is immense power that can be gained by combining the low-ℓ (large angular scale) measurements from Large Aperture Telescopes (LATs), such as the South Pole Telescope (SPT), with SATs.

The first part of this dissertation describes the design, characterization, and deployment of the SPT-3G receiver on the SPT. There is special emphasis placed on the development and characterization of the frequency-multiplexed readout, and characterization of system crosstalk. The second part of this dissertation uses data from the 2019 and 2020 austral observing season over a 1500 deg^2 patch of sky to make low-noise maps of the B-mode polarization of the CMB. This delves into techniques used for mitigating low-ℓ noise sources, including polarized atmosphere. These include weighting schemes, and an unbiased method to remove this noise source from data utilizing co-pointing detectors of different frequencies and the fixed spectral scaling of polarized atmosphere in accordance with Rayleigh scattering. This work serves both as demonstration of a LAT achieving high sensitivity at low-ℓ and as a study of atmospheric noise that will inform the design and operation of future LAT and SAT telescopes. This shows a path for producing competitive r constraints from a LAT optimized for high-ℓ science, and is a proof-of-concept for using LAT data in the search for primordial gravitational waves with next-generation CMB experiments.

To all the Nicks who helped me get through graduate school

Contents

Contents **ii**

List of Figures **iv**

List of Tables **x**

1 Scientific Motivation **1**
1.1 Big Bang Theory and the History of Our Universe 1
1.2 Measurements of The Cosmic Microwave Background 3
1.3 Inflation 7
1.4 Detecting r 13

2 The South Pole Telescope **20**
2.1 Readout 23

3 Development and Characterization of Frequency-Domain Multiplexed Readout **26**
3.1 Assembly of the SPT-3G Cold Readout Hardware 27
3.2 Characterization and Performance of the SPT-3G Cold Readout Hardware . 27
3.3 Current Sharing Noise 33

4 CMB Mapmaking **37**
4.1 SPT-3G Survey 37
4.2 Calibration 38
4.3 Time-Ordered Data Processing 40
4.4 Mapmaking with HEALPix 44

5 Polarized Atmosphere **47**
5.1 Characterization of Polarized Atmosphere 47
5.2 Removal of Polarized Atmosphere 50
5.3 Alternate Mitigation Methods 56

6 Null Tests **67**

7 BB Power Spectrum **72**
7.1 Bandpower Estimation with PolSpice 74
7.2 Foreground Removal 78
7.3 Power Spectrum 79
7.4 Discussion 80

Bibliography **82**

List of Figures

1.1 Edwin Hubble's measurement of Cepheid variables showing the correlation between the distance and the velocity of a galaxy, implying the expansion of the universe. The distance was determined by measuring their period and using the known relationship between a Cepheid variable's period and luminosity. The apparent luminosity compared to the absolute luminosity determined the distance. The velocity was determined from spectroscopic redshifts. Figure from [37] . . . 2
1.2 An artists rendering of the evolution of the universe. Figure from NASA / WMAP Science Team . . . 3
1.3 Maps of microwave radiation at 53 GHz, as seen by the Differential Microwave Radiometers (DMR) instrument on COBE instrument at different sensitivities. Figure from NASA / COBE Science Team . . . 4
1.4 The CMB, as measured by the FIRAS instrument on COBE, with a 2.725 K blackbody theory curve overplotted. They line up exquisitely well. Figure from NASA / FIRAS Science Team . . . 5
1.5 Planck Satellite measurements of the CMB. Figure from ESA and the Planck Collaboration . . . 6
1.6 Current measurements of the CMB Temperature power spectrum. Figure from NASA / LAMBDA Archive Team . . . 6
1.7 The purple line shows the radius of the region that will become the presently observed universe, as described by the standard cosmological model. The red line shows the corresponding curve if you take into account inflation. The numbers describing inflation are illustrative, since there are many theoretical possibilities. Figure from [28] . . . 9
1.8 A scalar field trapped in a false vacuum. The y-axis is the potential. Figure from [22] . . . 11
1.9 A simple model of slow-roll inflation. Figure from [30] . . . 12
1.10 Thompson scattering leading to net linear polarization. Figure from Wayne Hu [36] . . . 13
1.11 Even-parity E-mode polarization patterns and odd parity B-mode polarization patterns. Figure from [11] . . . 14
1.12 Scalar mode. Figure from Wayne Hu [36] . . . 14
1.13 Tensor mode. Figure from Wayne Hu [36] . . . 15

1.14 Theoretical predictions for the power spectra of Temperature (TT), E-mode (EE) and B-mode (BB) in the CMB. Figure from Neil Goeckner-Wald 16
1.15 Experimental landscape of the best constraints on the B-mode power spectrum. Figure from [3] 16

2.1 The South Pole Telescope 20
2.2 Frequency response of the SPT-3G receiver for the three frequency bands of 95, 150, and 220 GHz. The total atmospheric absorption is shown shaded in grey. Figure from [54] 21
2.3 *Left:* A cross-sectional diagram of the SPT-3G optics on the SPT, with a ray trace overlaid. *Right:* Cross-sectional view of the SPT-3G receiver and cold optics cryostat. Figure from [54] 22
2.4 *Left:* A photograph of the SPT-3G focal plane on the bench in Dark Sector Laboratory before being mounted in the receiver cryostat. On top, the 10 white hexagonal detector wafer modules can be seen. *Right:* One detector module, face down, with the LC readout boards mounted vertically on top of it. NbTi striplines in orange connect to the PCBs that will connect to the SQUIDs. Figure from [54] 23
2.5 One pixel from the SPT-3G focal plane. The dual-polarization sinuous antenna is in the middle surrounded by the 6 bolometers around the edge. Figure from [54] 24
2.6 *Left:* Basic schematic of the digital frequency-division multiplexing system. The stripline location is the shaded orange box. *Right Top:* Picture of the cold readout hardware, courtesy of Amy Bender [13]. Two LC boards on the left are connected to the PCB on the right that will connect to the SQUIDs. *Right Bottom:* Network analysis of one readout module. The resonant peaks of each individual bolometer's LCR circuit form a "comb" of resonances. Figure from [10] 25
2.7 Components of the warm readout. Figure from Amy Bender 25

3.1 *Left:* Cross-sectional diagram of the layers of the NbTi stripline. *Center:* Top of the LC Board PCB connected to the stripline with ultrasonic solder joints. *Right:* Bottom of the LC Board PCB connected to the stripline with ultrasonic solder joints. Figure from [10] 26
3.2 *Left:* Data (points) and fit (line) relating the power deposited on the stripline to the difference between the temperature at the center of the stripline, T_1, and the temperature at the edge, T_o. *Right:* Two resonances formed by the LC circuit of the cold electronics including the stripline terminated with a 33 nF capacitor (left peak) and the cold electronics terminated with a 33 nF capacitor before the stripline at the SQUID (right peak). The inductance of only the stripline is measured by finding the shift of the resonant frequency due to the change in inductance. Figure from [10] 29

3.3 Diagram of the stripline thermal conductivity measurement. A stack of 8 striplines is thermally sunk at each edge to 525 mK, and a heater is applied at the suspended center of the stack. Power is applied at the center, and the temperatures T_1 and T_0 are measured at the center and edge, respectively. Figure from [10] . 30
3.4 Projected crosstalk from measured parameters of a readout module in the SPT-3G receiver. Two resistances are plotted, to compare to previous simulations of design specifications (0.8 Ω), and representative SPT-3G bolometers (2 Ω). The outlier points that scatter above the design specification of 0.5% crosstalk are due to fabrication scatter in frequency peaks and increased bolometer resistance. Figure from [10] 31
3.5 The measured distribution of crosstalk coefficients in the SPT-3G receiver (orange line). The blue dashed line shows the noise expectation for the measurement. Figure from [14] 33
3.6 The dependence of the crosstalk coefficients on the spacing between the two AC bias frequencies. The points are the median value across 14 observations with the error bars showing the uncertainty in the mean of the distribution. The blue dashed line represents the designed minimum frequency spacing that predicted crosstalk coefficients $< 0.5\%$. Figure from [14] 34
3.7 A schematic of the SPT-3G readout highlighting different parts of the circuit – the green line shows the circuit after the SQUID, the blue line shows the path of the nuller, and the red and blue line at the nulling junction show two paths to ground. Figure from Amy Bender 35
3.8 Noise improvements in the SPT-3G Receiver from Year 1 to Year 2 due to the replacement of the SQUID amplifiers. 36

4.1 Noise Equivalent Temperature for the 90, 150, and 220 GHz bolometers in the SPT-3G focal plane. Figure from [54] 37
4.2 The SPT-3G survey patch, with the BICEP3 patch highlighted as well to show the overlap. Figure from [54] 39
4.3 Detector response to an elevation nod 40
4.4 Transfer Function showing the roll-off from the 10th-order polynomial filter . . . 42
4.5 This plot was created as a quick test of the elnod gain matching. It uses ∼half of the 2019 winter season's data, and calculates the noise by using the difference between the left-going and right-going scans. The 220 GHz detectors see ∼20% improvement in noise. 43
4.6 This plot was created as a quick test of the pair-difference gain matching. The three different bands are shown for the lowest subfield (where the atmosphere should be brightest, so any leakage should manifest strongest). Blue is labeled "Normal Weight" which is weighting detector timestreams by the inverse variance of the 0.1-1 Hz regime. In green is plotted "PD wts", the pair-differenced weighting scheme described in this section. This figure shows the dramatic improvement in noise from changing to a pair-difference weighting scheme. 45

4.7 Partitions of the first three steps of HEALpix resolutions. Figure from [27] . . . 46

5.1 One observation that is a great example of the discrepancy between the Q and U noise – both plots are on the same (arbitrary power) color scale, yet U looks like pristine white noise, while Q is extremely noisy, especially on large angular scales. 48
5.2 The "smoking gun" plot that something funny was up with our noise. There is no a-priori reason that we expect polarized noise to be asymmetric for a CMB experiment – nothing astrophysical should be preferentially in one polarization state. To see this level of asymmetry (Q/U ratios of 200!!) is a red flag, especially with such a strong band dependence. 48
5.3 Ice crystals in the atmosphere scattering thermal radiation from the ground should produce a horizontally-polarized signal, which aligns with Q. Figure from [56] 49
5.4 Polarized high Q noise as a function of elevation, showing higher Q/U ratios as a function of atmosphere thickness. 50
5.5 Low-ℓ T power as a function of Q/U ratio. High Q/U does not show a pattern of T dependence. This exonerates temperature leakage as the dominant source of polarized noise. 51
5.6 Percentage of high Q/U ratio observations as a function of ℓ range and band, showing that this noise source shows up strongest at low-ℓ and high frequency. . 51
5.7 Q/U ratio as a function of scan (proxy for time) and band for one observation, showing the "burst-like" structure of the noise, and highlighting how little a dramatic "burst" in the 150 GHz and 220 GHz data can effect the 90 GHz data, underscoring the strong frequency dependence of this noise source. 52
5.8 Spectral index of the Q noise for observations with a Q/U ratio > 3. Figure from Anna Coerver 52
5.9 *Left Top and Bottom:* The level of correlation between SPT-3G frequency bands during high Q/U ratio days is obvious from this figure. The color scale is different, but the spatial anisotropy is the same. *Right Top and Bottom:* Once the scaled 220 GHz map has been subtracted from the 150 GHz map, the Q noise can be seen to be visibly much reduced, and very similar to the U noise below. 53
5.10 The effect the 220 subtraction (both with the Butterworth filter and without) has on the 150 GHz Q noise. The black dashed line, labeled "smoothed" refers to the Butterworth filter being applied. 56
5.11 For one observation, the scaling factor with which the 220 GHz map was subtracted was optimized by sweeping around the minimum. The resulting noise power for each sweep can be seen on the y-axis. This figure shows that the optimization is quite a soft minimum (in this case, only a 1% difference from the true minimum), and that .15 works for most cases. 57
5.12 This figure shows the distribution of crossover points for all of the 2019 data. An example for one observation is shown in figure 5.10. 58

5.13 The three colored curves are the final map noise for the 2019-2020 SPT-3G BB analysis. The 90 GHz and 150 GHz curves are almost identical, proving the success of the combination of polarized atmosphere subtraction and map-based renormalization. The black dashed line shows the 150 GHz data before polarized atmosphere subtraction and map-based renormalization, which highlights the almost order of magnitude improvement by using these techniques. 59
5.14 *Left:* Three bolometer's TOD are plotted. The T common mode solution solved with all the detectors in that scan scan neatly lines up, as expected. *Right:* The Q and U common mode for this scan is shown. The difference in amplitude between the Q common mode, where the polarized atmosphere signal manifests, and the U common mode is apparent. An additional thing to note – the Q common mode does not have the same structure as the T common mode, again proving that this polarized signal is not leakage. 59
5.15 The effect of Q common mode subtraction for one observation of 220 GHz data. 60
5.16 The effect of Q common mode subtraction for 220 GHz 2019 data. 60
5.17 The effect of Q array-based common mode subtraction for 220 GHz 2019 data vs map-based subtraction. In both cases, the filtering transfer function has been accounted for. 61
5.18 The Signal and Noise of Q data shown in 2D Fourier space. 62
5.19 Improvements to the noise power in Q from reweighting the 2D Fourier modes based on their signal to noise when doing power spectrum estimation. The red line, p4, refers to the data having a 4th order polynomial subtracted from it as the time-domain filter. The blue line is also 4th-order-polynomial subtracted, but additionally includes the 2D reweighting of the modes before power spectrum estimation. 64
5.20 Polarization variance as a function of the number of subtracted common mode components This plot shows that there is substantial improvement in continuing to subtract modes up to about 15 modes, after which the improvement has diminishing returns. 65
5.21 This plot compares the previously published SPTpol E-mode power spectrum noise to the noise levels achieved for this same dataset in this exploratory work. [33] 66

6.1 The final T, Q, and U maps for 90, 150, and 220 GHz for this analysis. 68
6.2 An example of a null tests for each band. *Left:* Sun Up or Down null spectrum (red) and expectation spectra (black), for the 90 GHz detectors. *Center:* Azimuth null spectrum (red) and expectation spectra (black), for the 150 GHz detectors. *Right:* Moon Up or Down null spectrum (red) and expectation spectra (black), for the 220 GHz detectors. 69

7.1 One input bin of the mode mixing matrix. *Left:* The spectrum of one bin of the mode mixing matrix. *Right:* One simulated realization of the spectrum on the left. Both figures from Riccardo Gualtieri. 73
7.2 Output of mock observations of the $E-$mode input $\ell = 33$-58 bin of the mixing matrix. The input is only the $\ell = 33$-58 bin EE ΛCDM theory spectrum, seen in black in the top middle panel, and all the resulting power in the rest of the spectra are from mode-mixing. Figure from Riccardo Gualtieri 73
7.3 Preliminary Mode Mixing Matrix for the 90 GHz band. Figure from Riccardo Gualtieri 76
7.4 Preliminary Transfer Function 77
7.5 SPT-3G beam, as stitched together from both planet rasters and point sources in the field observations. Figure from [54] 77
7.6 Beam response as a function of ℓ, normalized to 1 at $\ell = 800$. Figure from [54] . 78
7.7 Galactic dust and synchrotron BB power at from a bin centered at $\ell = 69.5$ for the mm-wave band. Figure from [8] 79
7.8 A comparison between the BB error bars and a gravitational wave BB theory curve, showing the constraining power of this data set. 80

List of Tables

1.1 The symbols and descriptions of the main parameters of ΛCDM, the big bang cosmological model from a combination of CMB, gravitational lensing, and baryon-acoustic oscillation measurements [6]. 8
1.2 Current and future CMB experiment's noise projections. 18

3.1 Measured parameters of NbTi striplines 28

4.1 Full survey noise projections for SPT-3G [54] 38

5.1 Number of 150 GHz maps that are 220 GHz subtracted 56
5.2 Observations with $Q/U > 2$ for the baseline (no common mode) case, an array-based common mode, and a wafer common mode over different ℓ ranges 61

6.1 PTE values for null tests for 90, 150 and 220 GHz data with and without EE. These values need to exceed 0.01 to pass, which they all do regardless of whether the EE data is included. 71
6.2 Values to satisfy passing criterion 3 for each null test, with and without the EE data. 71

Acknowledgments

First and foremost, I would like to take this opportunity to thank my advisor Bill Holzapfel. Throughout graduate school, he was an infinite source of creativity and ideas. Bill has always treated me with respect and held me to a high intellectual standard, and the best parts of my work in this dissertation are due to me trying to live up to his expectation of excellence.

I also extend my gratitude to my other committee members, Adrian Lee, Martin White, and Aaron Parsons. They all have been an integral part of my greater Berkeley cosmology community, and I am grateful for how generous they have been with their time and expertise.

I also had the great fortune to work with fantastic postdocs when I started at Berkeley. Tijmen de Haan was a great source of readout knowledge, and Nathan Whitehorn taught me the value of doing a quick test to decide if something is worth doing. Graduate students Anna Coerver and Sam Guns were fun and smart labmates who made it a true joy to go to work. Likewise, Neil Goeckner-Wald's expertise was crucial for my understanding of power spectrum analyses, and his work on the null test code was an essential part of this work. I would also like to thank my housemate and fellow physics graduate student Margaret McCarter. It turns out running a marathon *was* easier than getting a PhD in physics.

The other major component of my graduate school was the time I spent at the South Pole. I learned how to drive a telescope, play cribbage, and deploy an instrument from our fearless deployment leaders Brad Benson, Adam Anderson and Amy Bender. I am also thankful for John Carlstrom, the PI of SPT, who helped me make the decision to come to Berkeley for graduate school in the first place. I would be remiss if I didn't thank the original crew of "SPTweens," the graduate students who made my deployment years fun – Matt "The Toronto 10" Young, Daniel "Christmas in McMurdo" Dutcher, Milo "God's Plan" Korman, Allen "Second Dinner" Foster, Joshua "I miss my wife" Sobrin, and Zhaodi "Z-pan" Pan. I also must thank our winterovers for spending the dark months at the South Pole to take all of the data in this dissertation. This is a small fraction of my SPT collaborators, without whom the telescope wouldn't exist. It truly is a group effort, and it has been a great team to be part of.

I would also like to thank my parents: my computer scientist mother, who made women excelling at STEM a fact of life I grew up with, and my wonderful father, who encouraged me to cold knock onto doors as an undergrad, leading to my first physics research position.

Last but not least, I'd like to thank all the Nicks who helped me through graduate school in chronological order that they came into Nick Harrington's life, as is the Berkeley way. Nick 1[1] was crucial to my understanding of CMB science. His equal parts excellent and kind scientific explanations are something that I greatly admire and hope to one day emulate. Nick 2[2] was a fantastic sounding board for discussing scientific problems and a wonderful friend. I couldn't have asked for a better CMBFF. I also am very grateful to him for looking over this manuscript, though I suspect that I will return the favor in a few months when he writes

[1]Nick Harrington
[2]Nick Huang

his dissertation. Finally, Nick 3[3]. Throughout graduate school, he went from boyfriend to McMaster-Carr same-day parts courier to husband. He has supported my career from the very beginning – bringing me food to the library while I studied for physics finals as an undergrad, writing silly letters to my address at the South Pole, listening to many many practice talks, and now moving to Chicago for my postdoc. Grad school was full of ups and downs, but I'm so lucky that Nick kept my time in California a consistent upswing.

[3]Nick Zebrowski

Chapter 1

Scientific Motivation

Modern cosmology was kicked off by a simple fact: the universe we live in is expanding. This stemmed from observational evidence. Hubble, famously first, and many others since have measured the velocity of galaxies as a function of distance, and they noticed something curious [37]. As seen in Figure 1.1, the greater a distance between a galaxy and Earth, the greater its recessional velocity. From this fact, one of two conclusions can be drawn:

1. Earth is the center of the Universe and everything is accelerating away from us.
2. The universe is expanding homogeneously and isotropically. Specifically, the distance between any two points in the universe is growing with time.

Scientists generally believe the latter. Once faced with the proposition that the universe is expanding, the natural inclination is to then turn the clock backwards. Lemaître first suggested that the observation that the Universe is currently expanding implies that at one time, everything existed at one point [45]. Scientists have built a model of cosmology around this simple paradigm: The Universe began in a hot, dense state, and subsequently expanded and cooled off.

1.1 Big Bang Theory and the History of Our Universe

At the far left of Figure 1.2 is a small point symbolizing the Big Bang. At the very beginning, the universe was a hot, dense, radiation-dominated plasma. As the universe adiabatically expanded, it consequently cooled off. About 2 minutes in to the universe's life, subatomic particles like protons, neutrons, photons, or baryons started forming. However since everything (including photons) was so hot and energetic, everything stayed ionized and opaque for another 400,000 years. Finally the universe cooled off enough due to expansion such that neutral atoms could form in an event called "recombination." Due to this, the mean free path of a photon for photon scattering became larger than the size of the observable universe. Finally, photons could propagate freely. This made a "surface" of last scattering

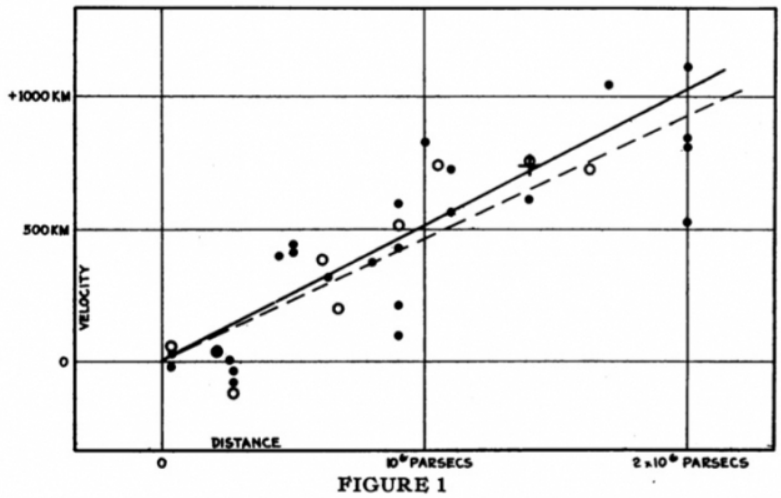

FIGURE 1
Velocity-Distance Relation among Extra-Galactic Nebulae.

Figure 1.1: Edwin Hubble's measurement of Cepheid variables showing the correlation between the distance and the velocity of a galaxy, implying the expansion of the universe. The distance was determined by measuring their period and using the known relationship between a Cepheid variable's period and luminosity. The apparent luminosity compared to the absolute luminosity determined the distance. The velocity was determined from spectroscopic redshifts. Figure from [37]

where photons were emitted from, which is referred to as the Cosmic Microwave Background (CMB). These photons have been free-streaming across the universe since 400,000 years after the Big Bang, and can now be observed by CMB cosmologists and telescope builders today. Immediately after being emitted, the photons that made up the CMB followed a blackbody spectrum with T $\approx$ 3000 K. Of course, these photons were emitted 400,000 years after the Big Bang, and they are observed now, $\sim$13 billion years later. Since the last scattering they passed through all of the rest of time - the dark ages, a time when the universe was full of neutral gas and dark matter slowly collapsing into the structure we see today. The first stars turning on and reionizing the universe. These photon are now at present time, near the flare at the end of the cone at the far right of Figure 1.2. This flare is meant to symbolize dark energy accelerating the expansion of the universe. Through all that time, the universe was expanding. This caused CMB photons to redshift from the infrared frequencies where they were last scattered to microwave frequencies where they can be observed now with a blackbody spectrum corresponding to a temperature of T = 2.726 K [25].

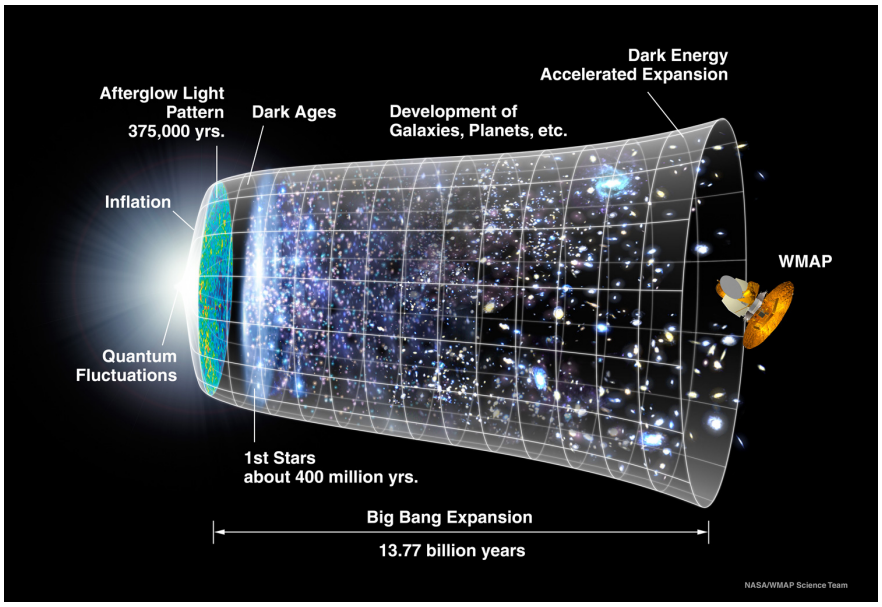

Figure 1.2: An artists rendering of the evolution of the universe. Figure from NASA / WMAP Science Team

1.2 Measurements of The Cosmic Microwave Background

The CMB was first detected by Penzias and Wilson in 1965 [51] as an excess source of microwave noise in their radio antenna, and correctly interpreted as having cosmological origin by Dicke, Peebles, Roll and Wilkinson [20]. Decades later, the first precision CMB satellite, the Cosmic Background Explorer (COBE) [47], confirmed the blackbody nature of the CMB with measurements between 60 GHz to 3 THz, and made exquisite maps of intensity fluctuations at 31.5, 53, and 90 GHz.

At a basic level, mapping out the microwave sky as COBE did results in the top panel of Figure 1.3. The exceptional feature is its featurelessness. It is remarkably uniform! This is because, as stated before, the CMB is blackbody radiation emitted from a mostly uniform plasma. Figure 1.4 shows that the blackbody prediction holds up remarkably well as measured by the FIRAS instrument on COBE. The error bars in Figure 1.4 were inflated to be 400σ to even be seen on this plot. However, the top panel of Figure 1.3 and Figure 1.4 only highlights what we have already posited about the early universe - that it's a hot, dense, blackbody plasma. The interesting bit lies in the spatial deviations from the mean of 2.726 K.

If instead of viewing this image on a 0-4 K scale, it's put on a scale that shows contrast (the middle image of Figure 1.3), interesting features pop out. The first and most obvious

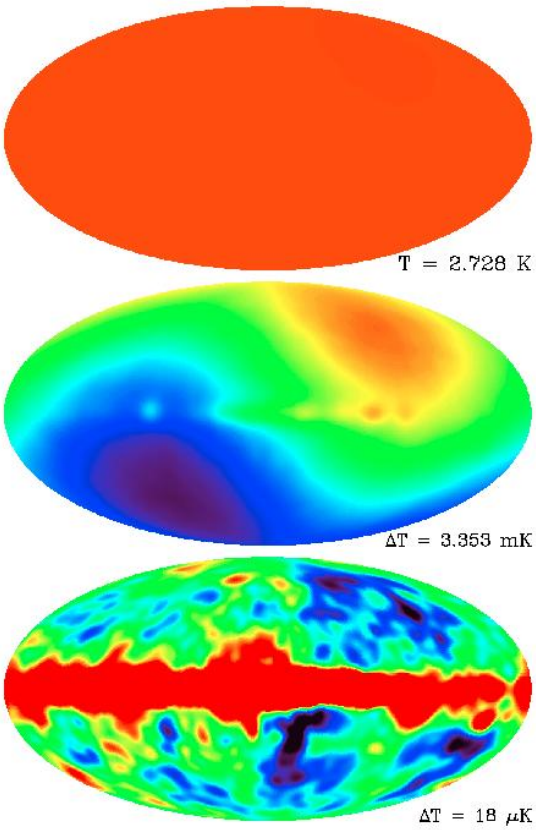

Figure 1.3: Maps of microwave radiation at 53 GHz, as seen by the Differential Microwave Radiometers (DMR) instrument on COBE instrument at different sensitivities. Figure from NASA / COBE Science Team

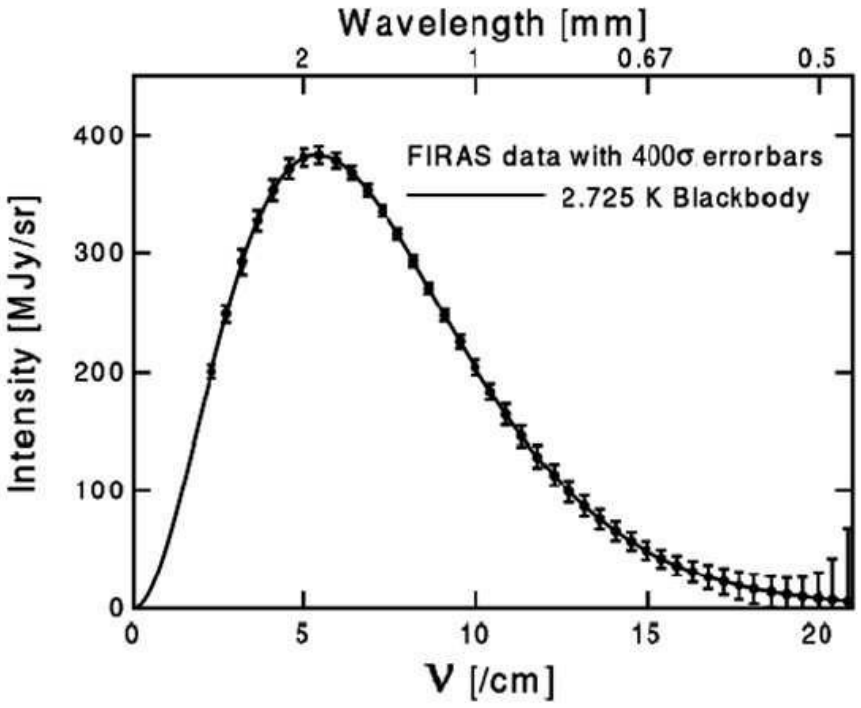

Figure 1.4: The CMB, as measured by the FIRAS instrument on COBE, with a 2.725 K blackbody theory curve overplotted. They line up exquisitely well. Figure from NASA / FIRAS Science Team

one is the CMB dipole. This feature is due to our current motion on Earth relative to the CMB. However this only tells us about Earth's motion, not the early universe.

To go one step further, the CMB dipole can be subtracted off of the middle image of Figure 1.3 to show the residual in the bottom image. In this way, the true early-universe anisotropy of the CMB off of the horizontal plane of the galaxy becomes apparent.

Precision measurements of the CMB have come a long way since COBE, and now the state-of-the-art is high-resolution maps like Figure 1.5 from the Planck satellite [6]. This figure is a beautiful picture of the young universe, however in this form it's hard to glean information. Cosmologists generally study CMB sky maps by taking their angular power spectrum, as seen in Figure 1.6. The axes on the plots are the multipole moment (ℓ) on the x-axis, or going from large scales on the sky on the left to small scales on the right. The y-axis is fluctuation power[1]. Compared to the sky map, this plot has rich structure from which the early universe can be described in quantitative terms. The modes that are larger than the Hubble radius, which aren't causally connected and are the unadulterated primordial power spectrum, are on the largest scales. Smaller angular scales have a series of peaks and

[1]More details on the mathematical formalism of this can be seen in Chapter 7

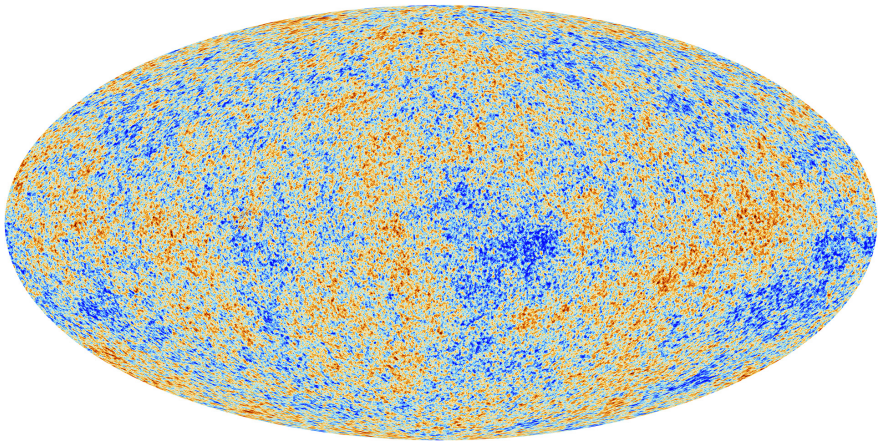

Figure 1.5: Planck Satellite measurements of the CMB. Figure from ESA and the Planck Collaboration

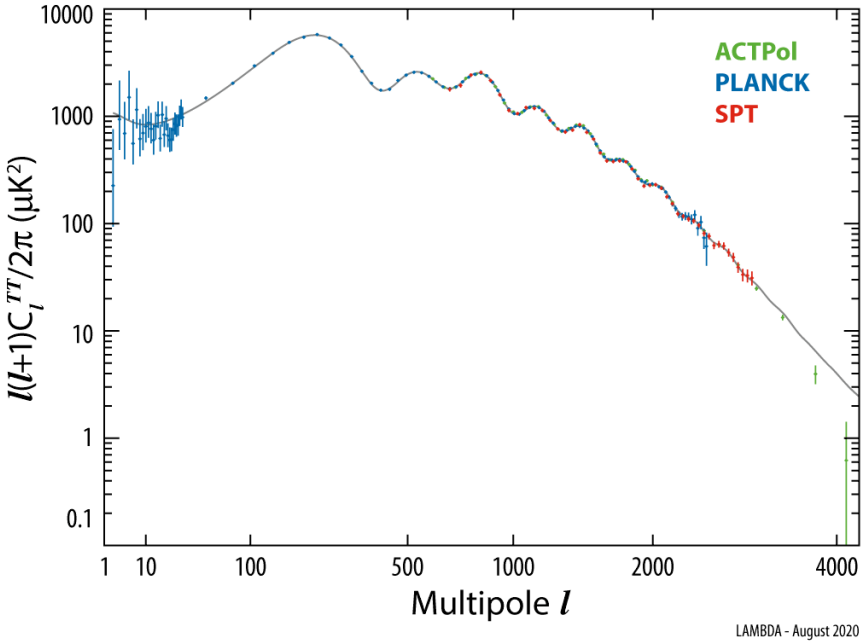

Figure 1.6: Current measurements of the CMB Temperature power spectrum. Figure from NASA / LAMBDA Archive Team

troughs stemming from the compressions and rarefactions in the photon-baryon fluid just before recombination. The first peak corresponds to the mode that had just enough time to compress once before recombination. The second peak corresponds to the mode that just has had time to compress and then rarefy before recombination, and so on for the rest of the peaks[2]. The third main feature of note is the damping of the oscillations on the far right side of Figure 1.6 on the smaller scales. The acoustic peaks are exponentially damped on scales smaller than the distance photons random walk during recombination. This power spectrum constrains the main parameters of ΛCDM, the big bang cosmological model. This model describes a universe with a hot, dense beginning followed by a cosmic expansion consisting of dark energy in the form of a cosmological constant Λ, cold dark matter (CDM), and standard model particles. In Table 1.1, the parameters of this model are listed. They've been divided into 3 categories – free, derived, and fixed parameters. The six free parameters parameterize the ΛCDM model, and from those, the derived parameters can be constructed. The derived parameters characterize the age of the universe, the rate of expansion, and other interesting facets of the universe – I've listed in the table a few select ones. The fixed parameters describe basic ΛCDM, however they can be allowed to vary to probe extension models to ΛCDM. This thesis will heavily focus on an extension in which r (the tensor-to-scalar ratio) is not equal to 0.

1.3 Inflation

The ΛCDM model has proven an overwhelming success, with it's 6 parameters measured to percent-level precision [6], and theoretical predictions are consistent with all current measurements [49]. However, there are a few problems that become apparent when matching up observations, both of the CMB and with the current universe, with just the ΛCDM model.

- **The Horizon Problem:** CMB maps are remarkably, remarkably uniform. To refresh, look back at Figure 1.3 and remember that the scale had to be increased to $\Delta T = 18\mu K$ in the bottom panel to even show the anisotropy. This is particularly shocking because this uniformity is true across distances farther than are causally connected – that is to say, that even if a photon from spot A traveled at the speed of light for the whole history of the universe, it couldn't reach spot B, yet spot B somehow "knows" to be the exact same temperature as spot A. More quantitatively, regions separated by more than a degree were not in causal contact at the time of the CMB, but are uniform to one part in 10^5.

- **The Flatness Problem:** The universe seems to have a perfectly tuned flat geometry – that is to say that photons moving in a parallel line continue to stay the same distance

[2]For a very nice discussion and some animations about this peak structure, I highly suggest Wayne Hu's intermediate cosmology tutorial `http://background.uchicago.edu/~whu/intermediate/intermediate.html`

Free Parameters		
Symbol	**Value**	**Description**
$\Omega_b h^2$	$(2.242 \pm 0.014) \times 10^{-2}$	Physical baryon density
$\Omega_c h^2$	0.11933 ± 0.00091	Physical dark matter density
θ_*	$0.0104119 \pm 2.9 \times 10^{-6}$	Angular scale of sound horizon at recombination
τ	0.0561 ± 0.0071	Optical depth to reionization
A_s	$(2.105 \pm 0.030) \times 10^{-9}$	Amplitude of primordial scalar fluctuations
n_s	0.9665 ± 0.0038	Scalar spectral index
Derived Parameters		
Symbol	**Value**	**Description**
Ω_Λ	(0.6889 ± 0.0056)	Dark energy density
Ω_m	(0.3111 ± 0.0056)	Matter density
H_0	67.66 ± 0.42	Hubble parameter today, in km s^{-1} Mpc^{-1}
t_0	13.787 ± 0.020	Age of the universe today, in Gyr
σ_8	0.8102 ± 0.0060	Matter fluctuation amplitude
Fixed Parameters		
r	0	Tensor-to-scalar ratio
$\sum m_\nu$	0.06 eV/c^2	Sum of the neutrino masses
N_{eff}	3.046	Effective number of relativistic particle species
Ω_{tot}	1	Total energy density
$\frac{dn_s}{d\ln k}$	0	Running of the scalar spectral index
w	1	Dark energy equation of state

Table 1.1: The symbols and descriptions of the main parameters of ΛCDM, the big bang cosmological model from a combination of CMB, gravitational lensing, and baryon-acoustic oscillation measurements [6].

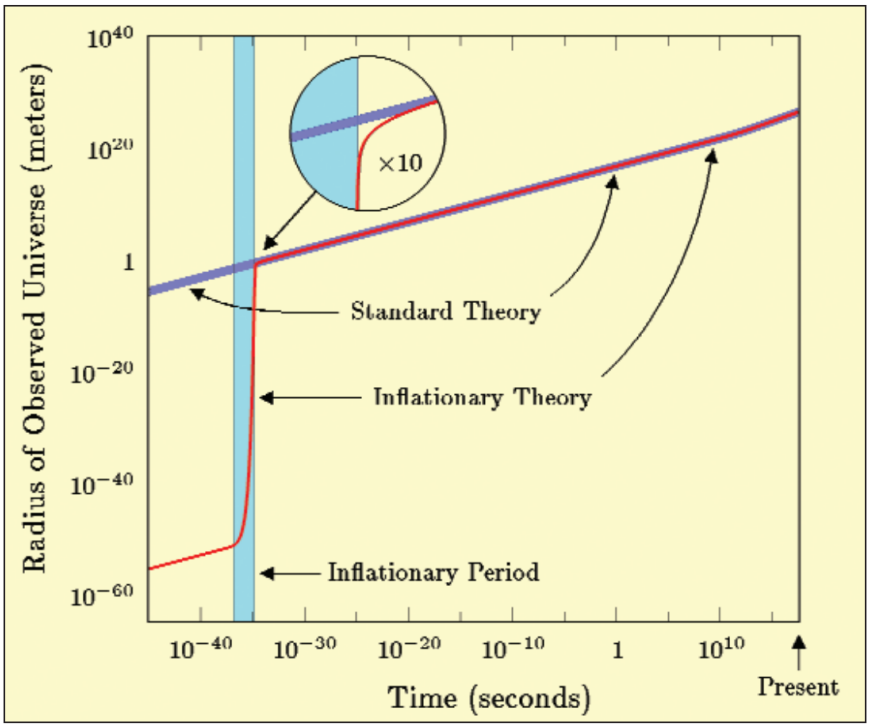

Figure 1.7: The purple line shows the radius of the region that will become the presently observed universe, as described by the standard cosmological model. The red line shows the corresponding curve if you take into account inflation. The numbers describing inflation are illustrative, since there are many theoretical possibilities. Figure from [28]

apart. A closed or open universe would have them converge or diverge due to the curvature of spacetime. This can only be true if the density of the universe is exactly equal to the critical density, which seems to be a very very small chance! It's more preposterous of an exact number because any variations from the critical density in the past would have increased dramatically with expansion.

- **The Magnetic Monopole Problem:** If the early universe was really hot at the beginning, many stable magnetic monopoles should have formed. However, none have been observed.

These problems can be solved with the theory of inflation [29]. The theory of inflation postulates that there was a period of accelerated, exponential, superluminal expansion in the early universe, which would explain the origin of the primordial density perturbations that grew into the CMB anisotropies, and the galaxies and stars we see today. This simple postulate solves the three problems that I laid out before. The horizon problem is solved because the regions were actually in causal contact before inflation. The flatness problem

is solved because inflation stretches any initial curvature to near flatness. The magnetic monopole problem is solved because inflation makes the density of magnetic monopoles reduced to nearly undetectable levels. Another convenient advantage of this model is that it also blows up primordial quantum fluctuations, seeding all of the structure that became the galaxies and stars we see today. There are a few main theoretical points that need to be considered about inflation: First, what caused it? To answer this, we need to look to general relativity.

$$\frac{d^2a/dt^2}{a} = -\frac{4\pi G}{3}(\rho + 3\mathcal{P}) \tag{1.1}$$

Above is a relationship that stems from the Einstein equations[3] relating the geometry of spacetime to the distribution of mass and energy within it. On the left side of the equation, $a(t)$ is a time dependent scale factor, which describes the distance between two objects as a function of time. $a(t)$ is defined by the relationship $d(t) = a(t)d_0$ where d_0 is the distance at a reference time. This relationship describes the separation of objects in an expanding (or contracting) universe. Equation 1.1 describes how a will change over time. On the right side of the equation, we have ρ, the density of mass-energy in the universe, and $\mathcal{P}$, the pressure. For inflation, the universe has to rapidly expand, resulting in a positive $\frac{d^2a/dt^2}{a}$. The condition to satisfy this is :

$$\mathcal{P} < -\frac{\rho}{3} \tag{1.2}$$

Therefore, to have inflation, an accelerating scale factor, negative pressure is required. To source this negative pressure, we write down a generic scalar field, $\phi(\vec{x}, t)$. Writing down the energy-momentum tensor for this field [22], we reach expressions for the pressure and density of this field:

$$\rho = \frac{1}{2}\left(\frac{d\phi^{(0)}}{dt}\right)^2 + V(\phi^{(0)}) \tag{1.3}$$

$$\mathcal{P} = \frac{1}{2}\left(\frac{d\phi^{(0)}}{dt}\right)^2 - V(\phi^{(0)}) \tag{1.4}$$

One intuitive solution could be a large potential, such as a field trapped in false vacuum as seen in Figure 1.8. This figure illustrates a situation where the field is trapped, so has low kinetic energy, however is stuck, so has a high potential energy. This would provide the big potential energy term, a negative pressure, and source inflation. However, when considering the functional form of the scalar field, we also have to ask the question "How did inflation end?". This rules out a huge class of models, for example the false vacuum model, since there's no good way to stop inflation, and we clearly know from observations that it has.

[3]For a more thorough treatment of where exactly this equation came from, please see [22].

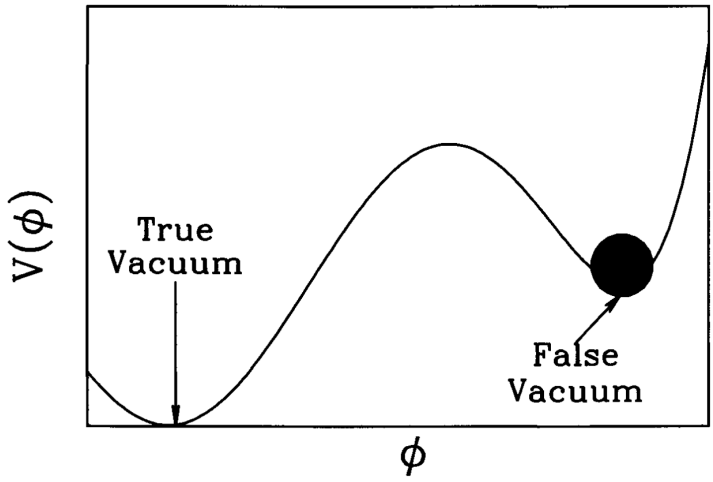

Figure 1.8: A scalar field trapped in a false vacuum. The y-axis is the potential. Figure from [22]

The most popular modern class of theories are of "slow-roll" inflation – fields that slowly roll down it's potential as seen in Figure 1.9. At the bottom, the potential energy goes to zero and inflation stops. As the field reaches the bottom it oscillates and the energy in the scalar field is converted into standard model particles in a process called reheating. From then on, we will return to our usually scheduled program of a hot big bang, neatly solving the problems laid out before, and lining up with what is observed in the universe today.

This is a nice picture to paint, however it is just wishful thinking unless experimental evidence exists. Fortunately, there are a few concrete predictions that we can measure. To do this, we examine perturbations to spacetime, specifically scalar and tensor perturbations. Cosmologists generally study these from their power spectrum, $P(\vec{k})$:

$$\left\langle \delta(\vec{k})\delta(\vec{k'}) \right\rangle \sim \frac{\delta^3(\vec{k}-\vec{k'})}{k^3} P(\vec{k}) \tag{1.5}$$

where $\delta(\vec{k})$ is the Fourier transform of the overdensity field $\delta(\vec{r}) \equiv (\rho(\vec{r}) - \langle\rho\rangle)/\langle\rho\rangle$ and $\delta^3(\vec{x})$ is the three-dimensional Dirac delta function.

The scalar field that drives inflation perturbs the metric and sources a series of scalar perturbations with power spectra P_s as seen in equation 1.6. The parameter k_* is a fiducial scale and conventionally $k_* = 0.05$ Mpc^{-1} [50].

$$P_s = A_s \left(\frac{k}{k_*}\right)^{n_s - 1} \tag{1.6}$$

The first prediction of inflation is that n_s, the primordial spectral tilt, and one of the parameters of the ΛCDM model as seen in Table 1.1, is going to be slightly less than 1.

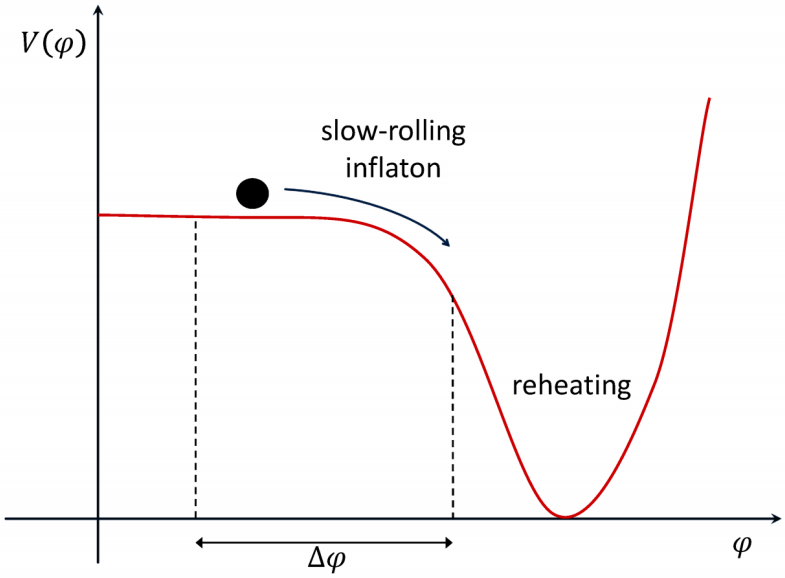

Figure 1.9: A simple model of slow-roll inflation. Figure from [30]

The parameter n_s is defined in equation 1.7 to be the relation which gives $n_s = 1$ for a perfectly flat spectrum. The prediction of a value slightly less than 1 is caused by the degree of departure from complete time-translation invariance during the period of inflation when observed structures were created. Since we know that the inflationary potential evolves with time and inflation ends, we predict this value.

$$n_s - 1 = \frac{d\ln(P_s)}{d\ln(k)} \tag{1.7}$$

There are additionally a series of tensor perturbations, P_t in equation 1.8, which are sourced by degrees of freedom in the metric being excited by the large energy scale of inflation, and manifest as gravitational waves.

$$P_t = A_t \left(\frac{k}{k_*}\right)^{n_t - 1} \tag{1.8}$$

If we can measure r, the ratio of tensors to scalars, we are directly probing the energy scale of inflation.

$$r = \frac{P_t(k_*)}{P_s(k_*)} \approx \frac{V}{(10^{16} GeV)^4} \tag{1.9}$$

For this reason, measuring r is said to be the "smoking gun" of inflation, and making a detection of r with a CMB experiment is seen as one of the great quests of modern cosmology.

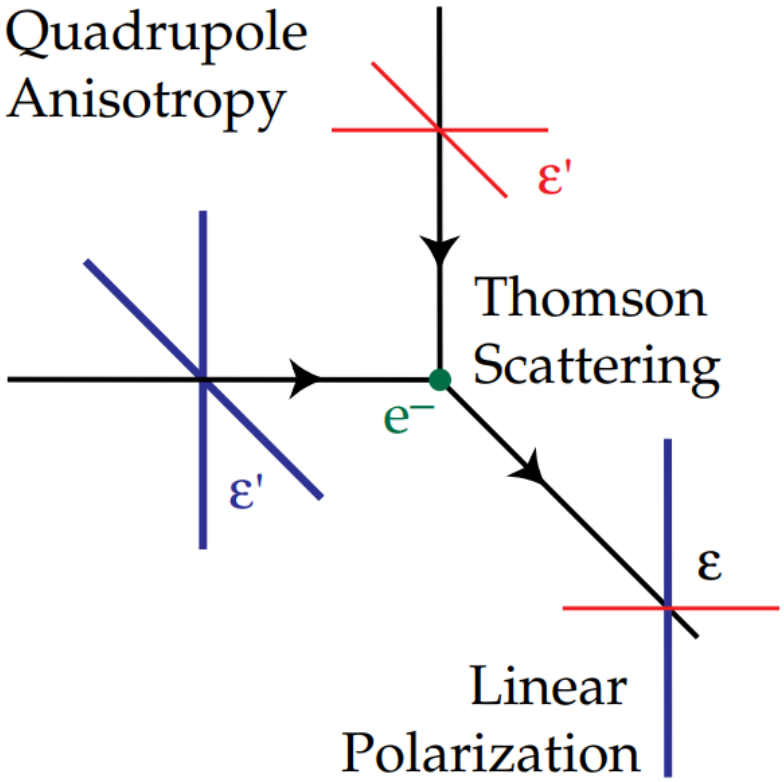

Figure 1.10: Thompson scattering leading to net linear polarization. Figure from Wayne Hu [36]

For the rest of this chapter, and of this thesis, I will discuss the intricate details of how to attempt just that.

1.4 Detecting r

A measurement of r is essentially a measurement of the ratio of the power spectrum of tensor modes to the power spectrum of scalar modes. The tensor modes created by inflation are unmeasureable with current technology. In order to test theories of inflation, we need to observe the imprints of the tensor modes on the polarization of the CMB.

Polarization of the CMB

The CMB is polarized at roughly the 10% level. This is due to Thompson scattering of CMB photons with quadrupole anisotropy [36]. In this case, the quadrupole anisotropy is

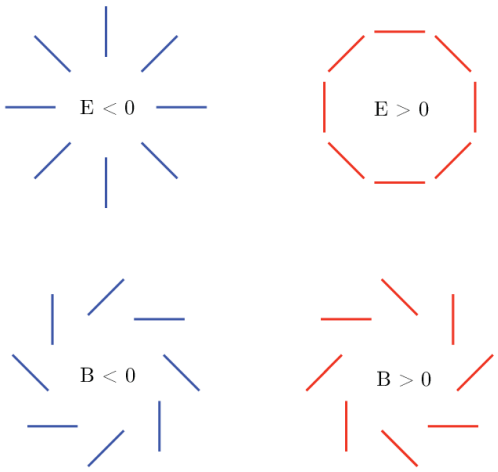

Figure 1.11: Even-parity E-mode polarization patterns and odd parity B-mode polarization patterns. Figure from [11]

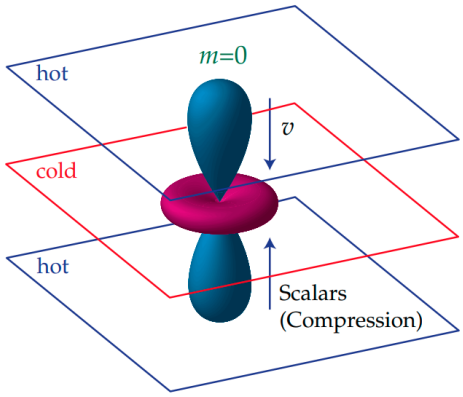

Figure 1.12: Scalar mode. Figure from Wayne Hu [36]

hot spots and cold spots in the CMB, where the hot and cold spots come from (respectively) gravitational underdensities and overdensities. This is demonstrated in Figure 1.10. The electron at the center of the figure scatters unpolarized light from the hot spot at the top of the figure, and the cold spot to the left of the figure, and the result is net linearly-polarized light coming out of the page.

For our discussions of CMB polarization, we will use the decomposition of E-modes and B-modes. This is similar to the familiar electromagnetism analogue for electric vs. magnetic fields. You can see graphically in Figure 1.11: the even-parity E-modes and odd-parity B-modes form an orthonormal basis.

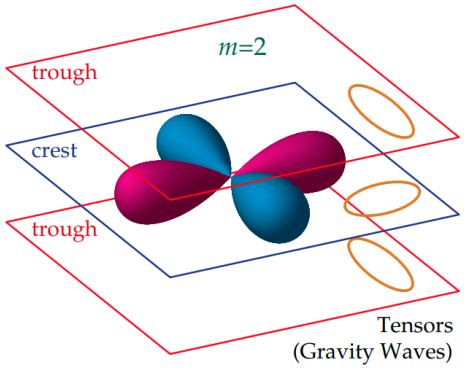

Figure 1.13: Tensor mode. Figure from Wayne Hu [36]

To understand the CMB polarization, there are two important cases of quadrupole anisotropy to consider. A scalar mode, or acoustic wave, travelling towards the top of the page will have alternating hot and cold temperature, as seen in Figure 1.12. If an electron is in the middle, it will see cool light in its plane, but hot above, and this will generate polarization from its quadrupole moment. Note, though, that there is an azimuthal symmetry around the direction of propagation for scalar modes. This even parity produces E-mode polarization, as seen in Figure 1.11.

Additionally in Figure 1.13 is pictured a tensor mode, or a gravitational wave. As it propagates towards the top of the page it does *not* have azimuthal symmetry. There are two directions that are important – both the direction of propagation and the direction of compression of space, which changes with time in the left-right direction in this diagram. This lack of azimuthal symmetry gives tensor perturbations their odd parity, leading to B-mode polarization patterns.

In conclusion, inflation will create gravitational waves (tensor modes), which will create B-mode polarization in the CMB. So, a measurement of r, the ratio of tensor to scalar modes, will provide the "smoking gun" evidence for inflation.

In Figure 1.14 are the projected theory curves of the Temperature (TT), E-mode (EE), and B-mode (BB) power spectra of the CMB. Some features to note are the relative amplitudes – EE is significantly fainter than TT, and BB is significantly fainter than EE. To measure the gravitational modes, the key is the very faint measurement of the B-mode spectrum.

Current Experimental Landscape

Figure 1.15 is a recent plot of the best limits on the B-mode power spectrum, and the feature that draws the eye is the cluster of upper limits. This is evidence of how many generations of experiments it took to even come close to having a low enough noise instrument to make

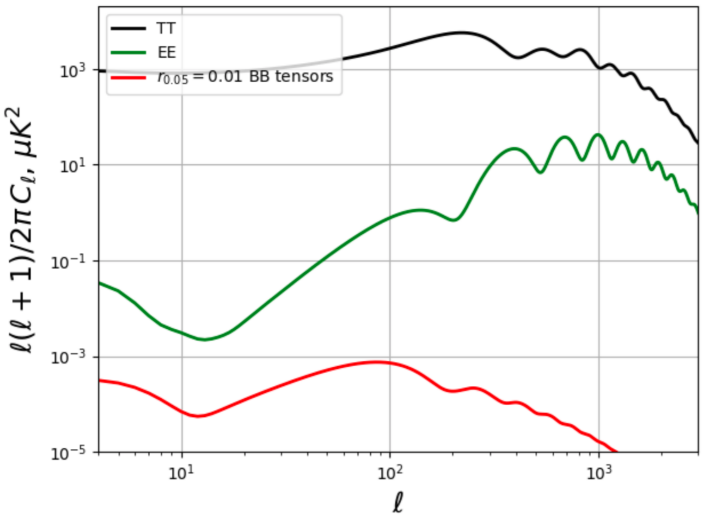

Figure 1.14: Theoretical predictions for the power spectra of Temperature (TT), E-mode (EE) and B-mode (BB) in the CMB. Figure from Neil Goeckner-Wald

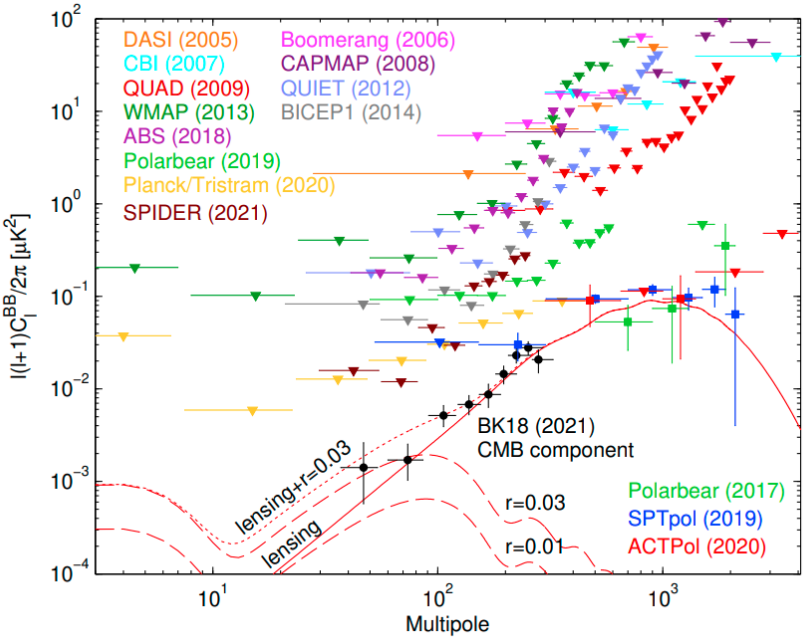

Figure 1.15: Experimental landscape of the best constraints on the B-mode power spectrum. Figure from [3]

this measurement. This only gets harder at larger angular scales where there are more red-spectrum noise sources, and the number of modes to measure become fewer.

Additionally, even if there exists a perfect measurement of B-modes in millimeter wavelengths, it's not an isolated signal of B-modes stemming from primordial gravitational waves. There are other sources of B-modes in millimeter wavelengths. Most notably, galactic dust foregrounds and gravitational lensing of E-modes from large-scale structure. So, to actually detect this faint inflationary signal, it is essential to first have an exquisitely sensitive telescope. Then, have good galactic dust foreground modeling to subtract off this non-inflationary component. Finally, "delensing" must be applied to the data – the technique of using small-angular-scale information about lensing E-modes to subtract off their contribution to B-mode power.

CMB experiments, some of which are listed on Figure 1.15, can be roughly divided into two categories – Large Aperture Telescopes (LATs) and Small Aperture Telescopes (SATs). Some examples of LATs include the South Pole Telescope (SPT) [15] [54] [23], the Atacama Cosmology Telescope (ACT) [31] [7], and POLARBEAR [2]. Examples of SATs include BICEP/Keck [5] and ABS [24]. Typically, LATs optimize their instrumental design and scan strategy to measure the gravitational lensing signal, since a large dish (about 4 meters or greater) is necessary for the fine resolution of that measurement. Smaller telescopes, such as BICEP, are optimized for larger angular scales where the gravitational wave signal peaks and for the control of polarization systematic errors. The rationale behind this division is that smaller telescopes are cheaper, so it's more cost effective to pack the focal plane with detectors in a SAT to get the lower noise necessary for a B-mode detection.

Currently there are two main telescope collaborations on the near horizon - one at the South Pole and one in Chile. The Simons Observatory [4] will take data in the Atacama Desert, and the South Pole Observatory will take data at the South Pole. Both will have 3-4 SATs, and 1 LAT. For the SPO, the LAT is SPT. Table 1.2 lists map depths for all of these experiments.

CMB-S4 will be the next-generation CMB experiment designed to perform an advanced search for the inflationary signal [1]. It will employ both SATs and LATs. Classically, the measurement of the large angular scale comes from the SATs, and the LATs are for delensing because the lensing signal peaks at small angular scales out of the reach of SATs.

However, there is immense power that can be gained by combining the low-ℓ (large angular scale) measurements from the LATs with the SATs, instead of just using them for delensing. There is no known physical reason that LATs cannot make a competitive measurement at large angular scales, just concerns that slower scanning speeds (limited by the telescope drive for a LAT) and far sidelobes could be problematic. For this reason, demonstrating that LATs can make low-noise measurements at large angular scales and developing techniques to achieve that goal has the potential to be massively influential in the years to come. This is the subject of my thesis - using a Large Aperture Telescope, SPT-3G, to make a low-ℓ measurement of the B-mode polarization of the Cosmic Microwave Background.

It has been a question of active discussion within the community whether a LAT could

Experiment	Configuration	**Temperature**	**Polarization**	**Sky Frac.**
SPT	LAT - 150 GHz	2.2 μK-arcmin	3.1 μK-arcmin	4%
SPO [48]	SAT - 150 GHz	1.77 μK-arcmin	2.5 μK-arcmin	4%
Simons Observatory (baseline/goal)	SAT - 145 GHz [4]	3.3/2.1 μK-arcmin	4.6/2.96 μK-arcmin	10%
CMB-S4 [1]	SAT - 145 GHz	1.77 μK-arcmin	2.5 μK-arcmin	3%

Table 1.2: Current and future CMB experiment's noise projections.

ever achieve the low-ℓ performance of a SAT. This work has shown that with careful characterization and mitigation of noise sources, a LAT can achieve high sensitivity at low-ℓ. The techniques presented here combat sources of noise that can limit the constraining power of both SATs and LATs. This work serves both as demonstration of a LAT achieving high sensitivity at low-ℓ and as a study of atmospheric noise that will inform the design and operation of future LAT and SAT telescopes.

Chapter 2

The South Pole Telescope

SPT-3G is the third generation camera on the 10-meter South Pole Telescope located at Amundsen-Scott South Pole Station in Antarctica [15] [54]. It has 16,000 transition edge sensor detectors that operate in three bands: 95, 150, and 220 GHz. Figure 2.2 shows why those band centers were chosen – the band edges neatly fit between atmospheric water and oxygen lines, so it's a clean measurement less contaminated[1] by atmosphere. Additionally,

[1]This contamination manifests in two ways: extra loading on the detectors, and the added fluctuation power in data

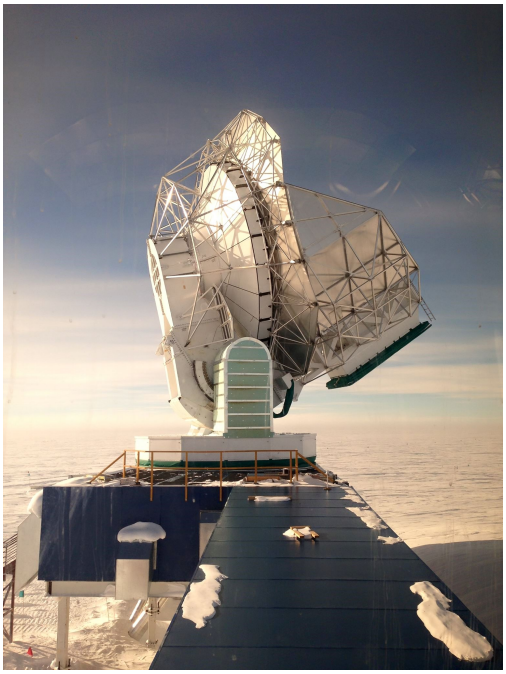

Figure 2.1: The South Pole Telescope

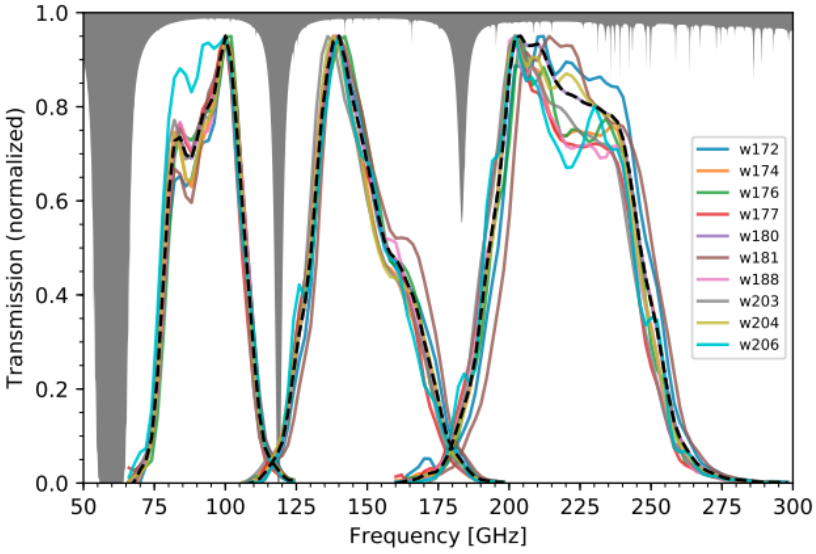

Figure 2.2: Frequency response of the SPT-3G receiver for the three frequency bands of 95, 150, and 220 GHz. The total atmospheric absorption is shown shaded in grey. Figure from [54]

referring back to Figure 1.4, it's sensitive to the peak of intensity of the CMB. SPT-3G is sensitive to both intensity and polarization and has 1 arcminute beams. This makes it ideal for both fine resolution science such as delensing or finding galaxy clusters, but it also is sensitive to large angular scales. SPT-3G has been observing a 1500 $\deg^2$ patch since 2018, and plans to run until the end of 2023. The next few sections will briefly describe an overview of the instrument, but for a more detailed description I refer you to [54].

Optics and Receiver Design

Light from the sky is reflected off the 10-m primary mirror (Figure 2.1) onto the 1.7-m secondary mirror, which in turn reflects to the 0.8-m flat tertiary mirror. This can be seen in the left panel of Figure 2.3. This telescope design is called an off-axis Gregorian, which is more optimal than a conventional on-axis antenna since there's no diffraction, reflection, or blockage from the secondary mirror and its supports. The secondary and tertiary mirrors are in the receiver cabin, a climate controlled box on the SPT. This is additionally shown in Figure 2.1 as the white rectangle on the far right side of the telescope. The optics in the receiver cabin move back and forth on an actuated optics bench, which is used to focus the instrument. From the tertiary the light passes through a high-density polyethylene environmental window into the receiver cryostat, which is pictured in cross-section on the right side of Figure 2.3.

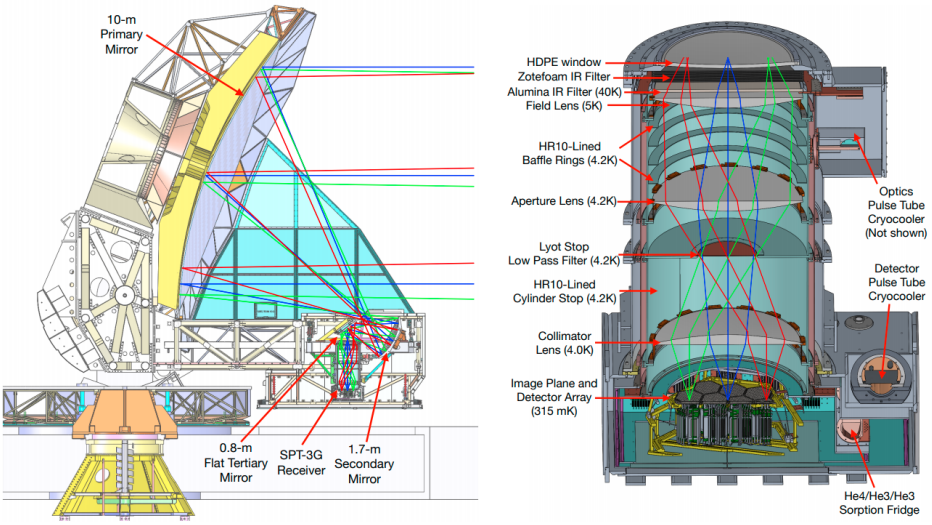

Figure 2.3: *Left:* A cross-sectional diagram of the SPT-3G optics on the SPT, with a ray trace overlaid. *Right:* Cross-sectional view of the SPT-3G receiver and cold optics cryostat. Figure from [54]

Detectors

The bottom of Figure 2.3 shows a rendering of the focal plane, which is pictured in actuality in the left panel of Figure 2.4. Immediately apparent are the 10 hexagonal silicon wafers which house our 16,000 detectors. These wafers operate at 315 mK. We have a three-tier focal plane comprising of the 315 mK (UC) stage, 385 mK (IC) stage, 1 K stage and 4 K stage separated by carbon fiber legs for thermal isolation. Surrounding the detectors, the shiny material in the picture is aluminized mylar which is used for RF shielding. On top of the 10 wafers, there are small hemispheric alumina lenselets which are used to effectively couple light to our detectors.

Underneath the white lenselet is a sinuous antenna connected to transition edge sensors (TES), shown in Figure 2.5. On a close up, the main features stand out. It is a log-periodic broadband sinuous antenna that is sensitive to two polarization states evident by the crossing pattern. The signal passes through in-line filters which define the 3 bands of 95 GHz, 150 GHz, and 220 GHz. The signal is thermalized in a termination resistor at the TES which is connected via a weak thermal link to a cold thermal reservoir. This type of detector is called a bolometer [9] [44] [39] [38]. TES are relatively simple detector technology- they are made from superconductors held in their superconducting transition with a tunable bias voltage operating under electrothermal feedback[2], at a temperature just above absolute zero. When the energy of a photon heats up the bolometer, the steepness of the transition makes that

[2]Two great resources about the details of this: [39] [38]

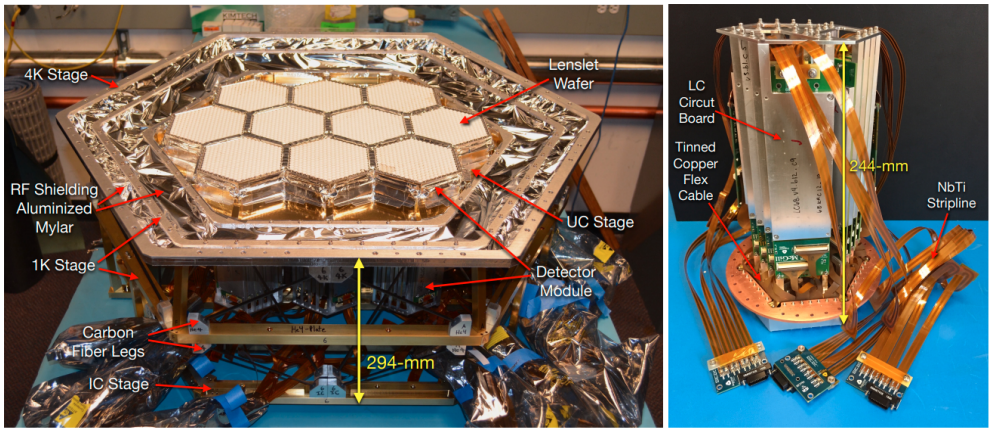

Figure 2.4: *Left:* A photograph of the SPT-3G focal plane on the bench in Dark Sector Laboratory before being mounted in the receiver cryostat. On top, the 10 white hexagonal detector wafer modules can be seen. *Right:* One detector module, face down, with the *LC* readout boards mounted vertically on top of it. NbTi striplines in orange connect to the PCBs that will connect to the SQUIDs. Figure from [54]

small change in temperature turn into a large change in resistance. This leaves us with the relatively simple problem of measuring the change in resistance.

2.1 Readout

The SPT-3G camera is composed of 16,000 TESs. For this number of detectors operating at cryogenic temperatures, multiplexing readout must be implemented. SPT-3G uses frequency-division multiplexing [13] [12] [21] [32]. Each detector is part of a resonant LCR circuit, where the series capacitor and inductor dictate the resonant frequency for each bolometer. An AC current bias provided via direct digital synthesis (the "carrier" in the left panel of Figure 2.6) is passed through a small bias resistor and the parallel combination of the detector comb, thereby providing a stiff voltage bias to each detector at the resonant frequency of its LCR circuit. Baseband feedback on each bolometer reduces the current through the SQUID amplifier by injecting a "nuller" signal to exactly cancel the carrier at the summing junction before the SQUID. After the SQUID, the residuals are demodulated at each carrier frequency. Sky signals modulate the TES' resistance such that they appear as sidebands on the carrier tone. The "nuller" tone needed to cancel the modulated carrier tone at the SQUID is the science signal. Since the readout has a multiplexing factor of 68, when a network analysis is taken of one readout module, a "comb" of resonant peaks appear, as seen in the bottom right panel of Figure 2.6.

The LCR circuit on the left panel of Figure 2.6 maps to physical hardware pictured

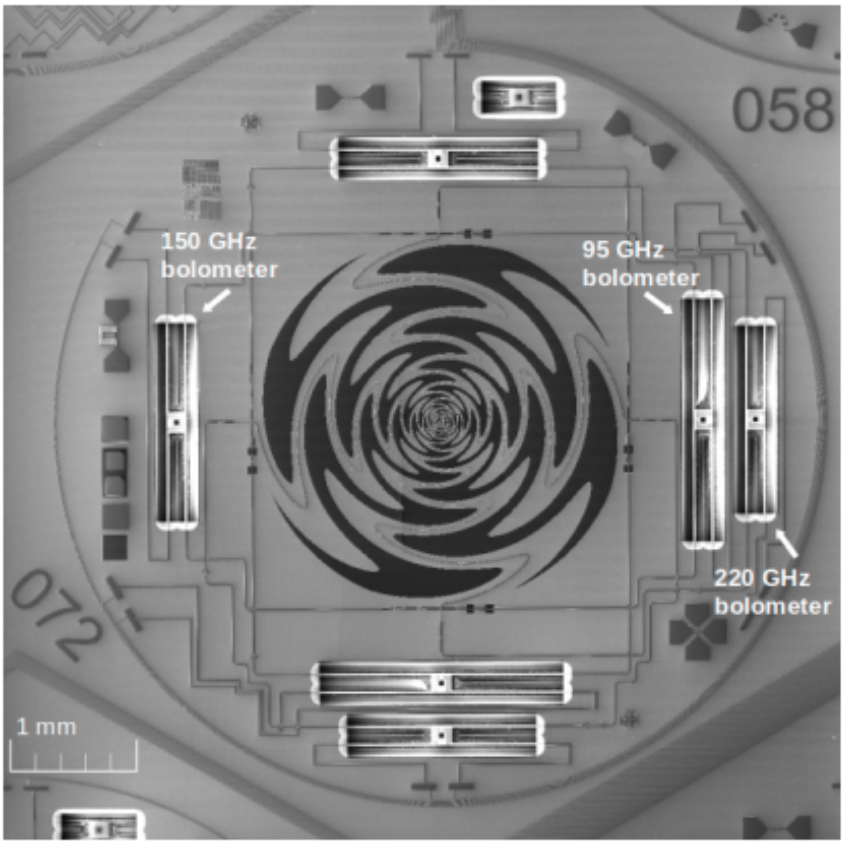

Figure 2.5: One pixel from the SPT-3G focal plane. The dual-polarization sinuous antenna is in the middle surrounded by the 6 bolometers around the edge. Figure from [54]

on the top right panel of Figure 2.6. Each detector is depicted as a variable resistor. The lithographed inductances and capacitances set the resonances of the (LC) circuit (modules on the right side of the hardware photo in Figure 2.6) [52]. The wiring between the 4 K SQUID amplifiers and the ∼300 mK LC boards is a Niobium-Titanium (NbTi) broadside coupled stripline (shaded box on the circuit diagram, right side of the hardware photo in Figure 2.6). The stripline has non-zero inductance and capacitance as well, which manifests as a stray inductance and capacitance in the circuit. Minimizing this stray impedance is crucial to have a low-crosstalk receiver.

SQUID amplifiers are connected to warm readout data acquisition boards (seen in Figure 2.7), where the signal is demodulated and can be then stored on a computer for further data analysis.

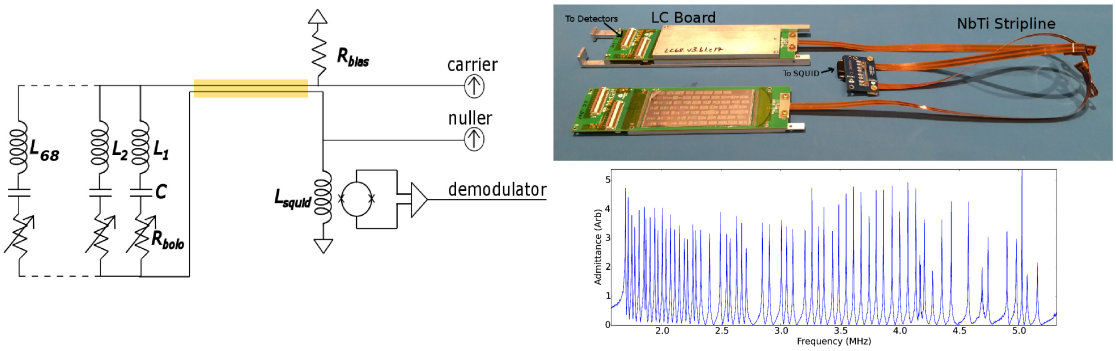

Figure 2.6: *Left:* Basic schematic of the digital frequency-division multiplexing system. The stripline location is the shaded orange box. *Right Top:* Picture of the cold readout hardware, courtesy of Amy Bender [13]. Two *LC* boards on the left are connected to the PCB on the right that will connect to the SQUIDs. *Right Bottom:* Network analysis of one readout module. The resonant peaks of each individual bolometer's *LCR* circuit form a "comb" of resonances. Figure from [10]

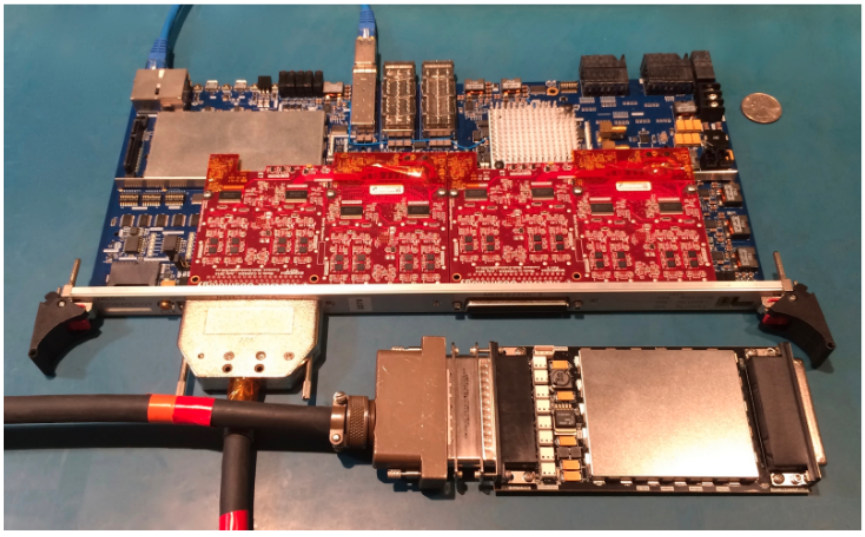

Figure 2.7: Components of the warm readout. Figure from Amy Bender

Chapter 3

Development and Characterization of Frequency-Domain Multiplexed Readout

To get tight inflationary constraints, exquisite noise performance and characterization of the instrument is necessary. First, I will discuss development of the low-impedance striplines and the ultrasonic soldering process used to connect them to the system. Then I will talk about characterizing SPT-3G's crosstalk, both at the component and system level. Finally, I will discuss current sharing noise, the dominant source of noise in SPT-3G data when it was first deployed, and the way it was fixed. Please note that some figures and sections of this chapter were previously published in [10] and [14] with permission of the co-authors.

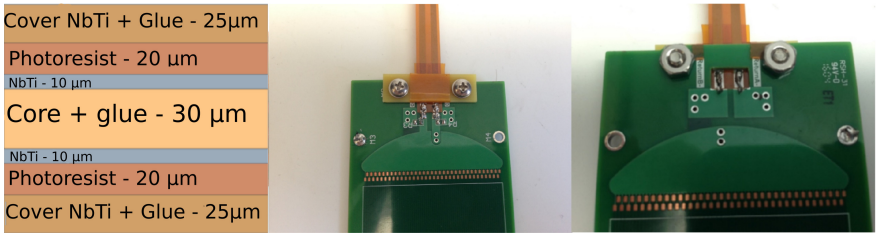

Figure 3.1: *Left:* Cross-sectional diagram of the layers of the NbTi stripline. *Center:* Top of the LC Board PCB connected to the stripline with ultrasonic solder joints. *Right:* Bottom of the LC Board PCB connected to the stripline with ultrasonic solder joints. Figure from [10]

3.1 Assembly of the SPT-3G Cold Readout Hardware

For the SPT-3G receiver, 120 *LC* modules are attached to 120 striplines. The striplines are made of NbTi[1]. NbTi is an attractive low-resistance wiring choice due to its superconducting temperature of 10 K. However, attaching the NbTi stripline to the *LC* module, as seen in Figure 3.1, is non-trivial because NbTi rapidly forms a tough non-conductive oxide layer. To combat this, connection methods utilizing ultrasonic solder are implemented. The method of ultrasonic soldering involves a solder formulated with metallic oxides and a specialized soldering iron[2]. The soldering iron vibrates at ultrasonic frequencies (tens of kHz), which causes cavitation in the molten solder. This disrupts the oxide on the metal and allows the ultrasonic solder to adhere to the NbTi surface. Once the stripline has been tinned with ultrasonic solder, conventional solder can be used to attach the striplines to the pads on the PCB leading to the SQUID or *LC* board. Examples of this connection are shown in Figure 3.1.

3.2 Characterization and Performance of the SPT-3G Cold Readout Hardware

While multiplexed readout minimizes the thermal load from wiring, control of stray resistances, capacitances, and inductances is essential to minimize crosstalk. Here, we present characterization of the NbTi striplines to show the value of inductance meets the targeted maximum parasitic series inductance of 60 nH [13], and that the stripline and solder joint resistance are zero within measurement error. Values for the capacitance, inductance, resistance, and thermal conductivity are given in Table 3.1.

Characterization of Niobium-Titanium Striplines

Broadside-coupled NbTi striplines connect the 4K SQUIDs to the ∼300 mK *LC* boards. Each line is 60 cm long and 2 mm wide, with a 30 μm core between each differential pair, as seen in the cross sectional diagram in Figure 3.1. To minimize the wiring inductance, the wires are close together so that the magnetic fields from their currents maximally cancel.

Two resonant circuits are compared to measure the inductance of the NbTi stripline. The first circuit terminates the SQUID with a 33 nF capacitor. The second attaches the stripline to the SQUID and terminates the stripline with a 33 nF capactior. The capacitance value was chosen to create a resonance within the readout bandwidth of the electronics, and because it is a much larger value than the stripline capacitance of 1.47 nF. Measuring the resonant peak location, ν_L, determines the inductance L for the circuit, as seen in Equation 3.1.

[1] NbTi rolled by Rikazai Co., Ltd, and stripline manufactured by PrimeTech Corporation

[2] We used the Cerasolzer USS-9210 Ultrasonic Soldering System and Cerasolzer CS297-150 solder.

Table of parameters for NbTi striplines	
Parameter	**Value**
Capacitance (at 100 Hz)	110 pF
Inductance	21 ± 1 nH
Resistance	$< 10^{-4} \Omega$
Thermal Conductivity $\times$ Cross-sectional Area	$kA = 6.0 \pm 0.3\ T^{0.92 \pm 0.04} \mu$W mm K^{-1}for .5 to 5 K

Table 3.1: Measured parameters of NbTi striplines

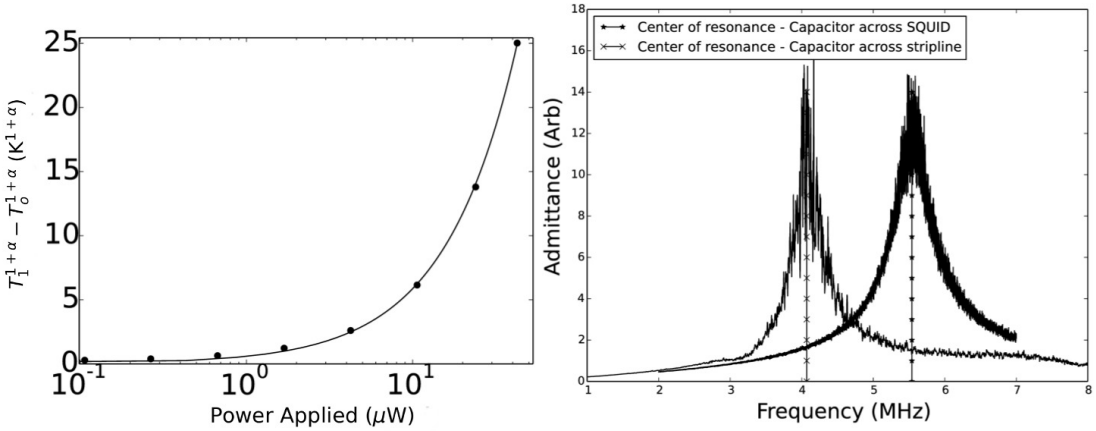

Figure 3.2: *Left:* Data (points) and fit (line) relating the power deposited on the stripline to the difference between the temperature at the center of the stripline, T_1, and the temperature at the edge, T_o. *Right:* Two resonances formed by the LC circuit of the cold electronics including the stripline terminated with a 33 nF capacitor (left peak) and the cold electronics terminated with a 33 nF capacitor before the stripline at the SQUID (right peak). The inductance of only the stripline is measured by finding the shift of the resonant frequency due to the change in inductance. Figure from [10]

$$\nu_L = \frac{1}{2\pi\sqrt{L \times 33\text{nF}}} \tag{3.1}$$

The difference in the resonant peak locations of the two circuits determines the stripline inductance, pictured in the right panel of Figure 3.2. The stripline inductance is measured to be 21 $\pm$1 nH, and the total parasitic inductance due to the stripline, connectors, and wiring on the SQUID mounting PCB is measured to be 46 $\pm$1 nH.

The thermal conductivity of the striplines impacts the millikelvin stage heat load. For cryogenic experiments, an important quantity to note is the product of the thermal conductivity k and the stripline cross-sectional area A, which describes the heat load for this specific application. This product is readily fit by a power law with normalization A_0 and exponent α.

$$kA = A_0 T^{\alpha} \tag{3.2}$$

To measure the stripline thermal conductivity, eight striplines are stacked, and both sides of the stack are thermally sunk to 525 mK. A heater and thermometer are attached at the suspended center of the stack, and an additional thermometer is attached at the edge of the stack. This experimental setup is shown in Figure 3.3. The heater deposits power P onto the suspended center of the stripline. Temperature T_1 is measured at the center where the power

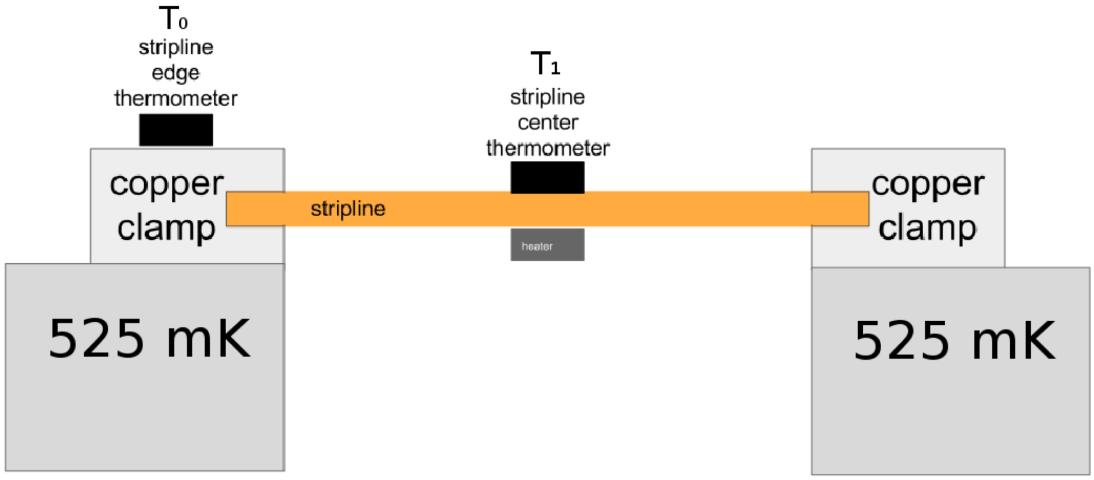

Figure 3.3: Diagram of the stripline thermal conductivity measurement. A stack of 8 striplines is thermally sunk at each edge to 525 mK, and a heater is applied at the suspended center of the stack. Power is applied at the center, and the temperatures T_1 and T_0 are measured at the center and edge, respectively. Figure from [10]

is deposited, and temperature T_0 is measured at the edge. This is repeated for a variety of applied powers, and the relation between the power applied and the edge temperature measured can be fit to the integral of the power law described in Equation 3.2, with the fit shown in Figure 3.3. These data are best described by the fit $kA = 6.0 \pm 0.3\ T^{0.92\pm0.04}\mu$W mm K^{-1}. This results in wiring thermal loading of 0.48 μW at the UC stage, 3.3 μW at the IC stage and 11 μW at the 1 K stage, which is tolerable for our thermal budget.

The total resistance of the stripline and solder joints is measured via a 4-point measurement with a Picowatt AVS-47 resistance bridge operating at 13.7 Hz. Liquid helium was used to cool the stripline below its critical temperature. This measurement results in an upper limit on the resistance of $< 0.0001\ \Omega$.

Constraining Cold Readout Performance with Crosstalk : At the component level

For frequency-division multiplexed systems, careful control of stray inductances and capacitances are crucial to mitigate crosstalk. Two forms of crosstalk dominate frequency-division multiplexed readout systems—bias carrier leakage and non-zero wiring impedance. There is

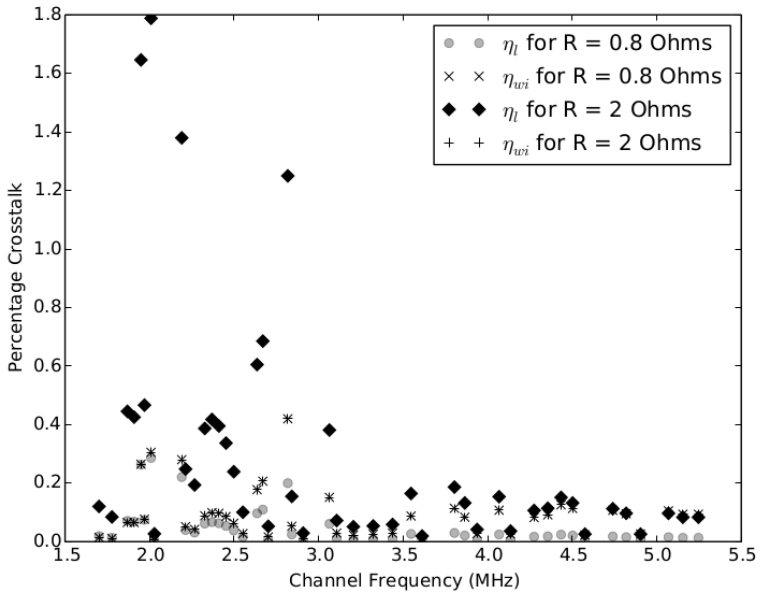

Figure 3.4: Projected crosstalk from measured parameters of a readout module in the SPT-3G receiver. Two resistances are plotted, to compare to previous simulations of design specifications (0.8 Ω), and representative SPT-3G bolometers (2 Ω). The outlier points that scatter above the design specification of 0.5% crosstalk are due to fabrication scatter in frequency peaks and increased bolometer resistance. Figure from [10]

a third form of crosstalk from the mutual inductance of inductors that are close in channel frequency and physically close on-chip. SPT-3G has diminished this mechanism by fabricating neighboring channels' inductors physically well-separated on the chip [32] [52]. The ratio of crosstalk from bias carrier leakage, $\eta_{\rm l}$, for a bolometer with resistance $R_{\rm bolo}$, in series with inductor L, and with spacing in frequency to its nearest neighbor, $\Delta\Omega$, can be described by Equation 3.3.

$$\eta_{\rm l} = \frac{R_{\rm bolo}^2}{2\Delta\Omega L} \tag{3.3}$$

The wiring impedance crosstalk, $\eta_{\rm wi}$, is described in terms of the current at frequency Ω_i on channel i, $I_{{\rm Ch}i}^{\Omega_i}$ with stray impedances $L_{\rm stray}$ by Equation 3.4.

$$\eta_{\rm wi} = -\frac{I_{{\rm Ch}i\pm1}^{\Omega_i}}{I_{{\rm Ch}i}^{\Omega_i}} \frac{\Omega_i}{\Delta\Omega} \frac{L_{\rm stray}}{L} \tag{3.4}$$

See Dobbs 2012 [21] for further discussion and derivation of these crosstalk terms. For the SPT-3G system, a network analysis measures peak locations and frequency spacing for one

module. As mentioned above, the stray inductance is 46 nH and each inductor in the LC board is 60 μH. The bolometers in the SPT-3G receiver are conservatively described by $R_{\rm bolo}$ = 2 Ω. Crosstalk calculated using a resistance of 0.8 Ω is additionally displayed to compare to the crosstalk simulations in Bender 2016 [13]. Figure 3.4 shows the projected crosstalk from both mechanisms as a function of frequency using these measured parameters. For $R_{\rm bolo} = 2$ Ω, the median value of percentage crosstalk from leakage current is 0.22%, and from wiring impedance is 0.09%. Outlier channels that show crosstalk above the design specification of 0.5% crosstalk [13] are due to fabrication scatter in resonant frequency locations and increased bolometer resistance.

Constraining Cold Readout Performance with Crosstalk : At the system level

Crosstalk is measured for SPT-3G using observations of the galactic HII region RCW 38. SPT-3G regularly observes RCW 38 as part of its calibration scheme, raster scanning the telescope such that every detector in the focal plane sees the source. RCW 38 is slightly extended compared to a true point source. Therefore, a template for the expected flux distribution is constructed from the average for all detectors within a given observing band (95/150/220 GHz) and detector wafer. A map of RCW 38 is then made for each detector individually and the associated template is used to measure the flux at the expected source position (the primary signal from that detector). Flux is also measured at the known offsets for all detectors within the same readout module. The ratio of these two flux measurements quantifies the crosstalk coefficients for each detector. The procedure is also applied to a region of the map outside the source region to generate a noise expectation. Figure 3.5 shows the resulting crosstalk distribution and the noise expectation. A preliminary investigation suggests that the crosstalk level is stable over time, consistent with the expectation that the primary sources are driven by geometries of LC components within the system.

There are several subtleties present in the crosstalk analysis. First, this technique measures the total crosstalk in SPT-3G, including any optical contribution. However, negative crosstalk coefficients can only originate in the readout. Next, this analysis is unable to separate the individual crosstalk coefficients from each of the bolometers within the same pixel. Consequently, the crosstalk coefficient is assigned to the detector with the bias frequency closest to that of the primary detector. As mentioned previously, RCW 38 is slightly extended. Spatial neighbors in the focal plane often fall within the source envelope, confusing the crosstalk measurement. There is no correlation between focal plane position and relative spacing of bias frequencies in SPT-3G. Therefore, detector pairs separated by less than 20 arcminutes are excluded in this characterization of readout crosstalk ($\sim$ 25% of available pairs). There is a small excess of positive crosstalk in Figure 3.5, which could be residual from this source envelope effect or non-readout crosstalk. Finally, as described previously, crosstalk coefficients are only calculated between detectors within the same readout module. When the measurement is expanded to include wafer-level crosstalk coefficients, there is no

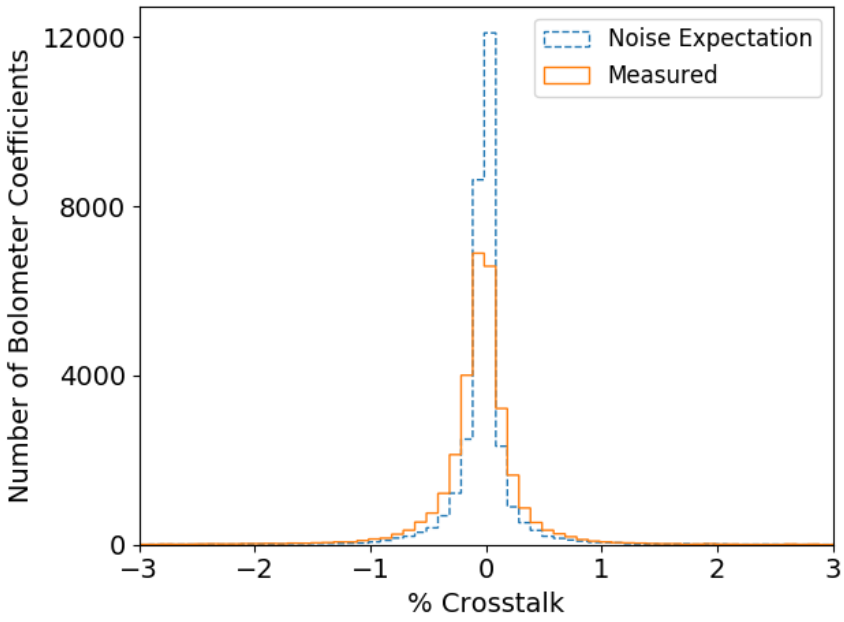

Figure 3.5: The measured distribution of crosstalk coefficients in the SPT-3G receiver (orange line). The blue dashed line shows the noise expectation for the measurement. Figure from [14]

additional crosstalk significant in comparison to the noise expectation.

The cryogenic readout components for SPT-3G were designed to maintain crosstalk at a level of 0.5% or below, assuming zero scatter in the resonant frequencies [13]. There is a tail in the distribution of crosstalk components shown in Figure 3.6 that exceeds this specification. To understand this deviation, the median crosstalk level across multiple RCW 38 observations is plotted as a function of the bias frequency separation between the detectors (shown in Figure 3.7). The vertical dashed line denotes the minimum frequency spacing in the design. The crosstalk coefficients in excess of 0.5% clearly correlate with bias frequencies that are closer together than designed (a result of small deviations from design in the fabricated capacitors). Future fMux systems with improved control of this frequency scatter or other design changes that mitigate the mechanisms by which crosstalk depends on bias frequency spacing will suppress this excess.

3.3 Current Sharing Noise

When SPT-3G was first deployed, there were unknown sources of readout noise limiting the array's performance. To understand this noise source, consider Figure 3.7. Any noise that

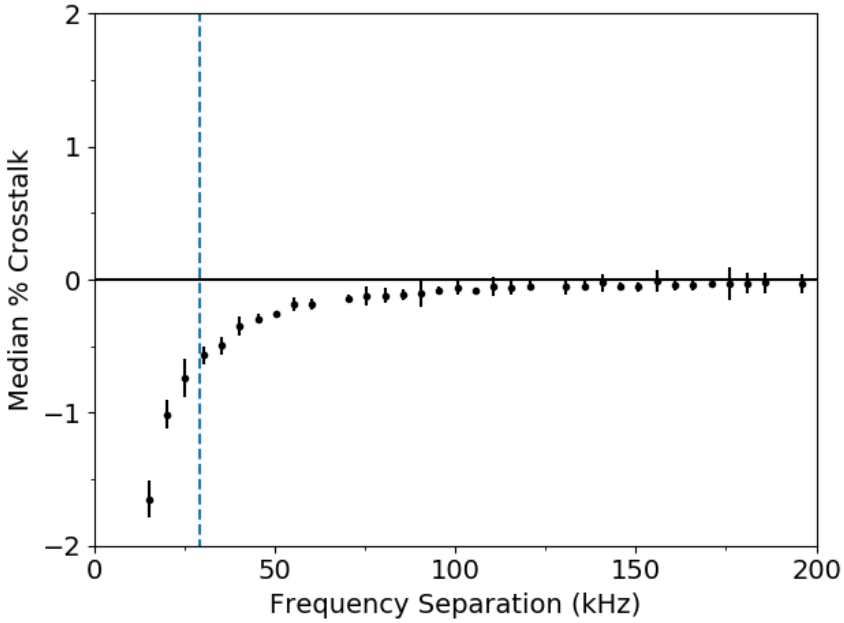

Figure 3.6: The dependence of the crosstalk coefficients on the spacing between the two AC bias frequencies. The points are the median value across 14 observations with the error bars showing the uncertainty in the mean of the distribution. The blue dashed line represents the designed minimum frequency spacing that predicted crosstalk coefficients $< 0.5\%$. Figure from [14]

exists in the cold (the .25 K with the dashed line around it) part of the circuit will simply show up as noise in the data. The nuller will perfectly replicate it and the nulling point right before the SQUID amplifier will be exactly zero. This is all an understood part of the design. However, there was unexpected trouble with sources of noise that effect the part of the circuit highlighted in lime green. These are sources of noise that come in after the SQUID amplifier. This noise will still be replicated by the nuller, since the nuller is agnostic to whether the noise originates in the cold or warm part of the circuit. However, when the replication reaches the nulling point, it will be unmatched by anything coming from the cold circuit. So instead of seeing a virtual ground at the nulling point, it will have two paths to ground – the red path and the blue path – through the comb, and through the squid input coil. This then amplifies the noise as the nuller tries harder to correct for this divided residual. This noise will be amplified by the ratio of the impedance of the SQUID to the impedance of the cold circuit, as seen in Equation 3.5.

$$Noise \propto \frac{Z_{\text{SQUID Input}}}{Z_{LCR}} \tag{3.5}$$

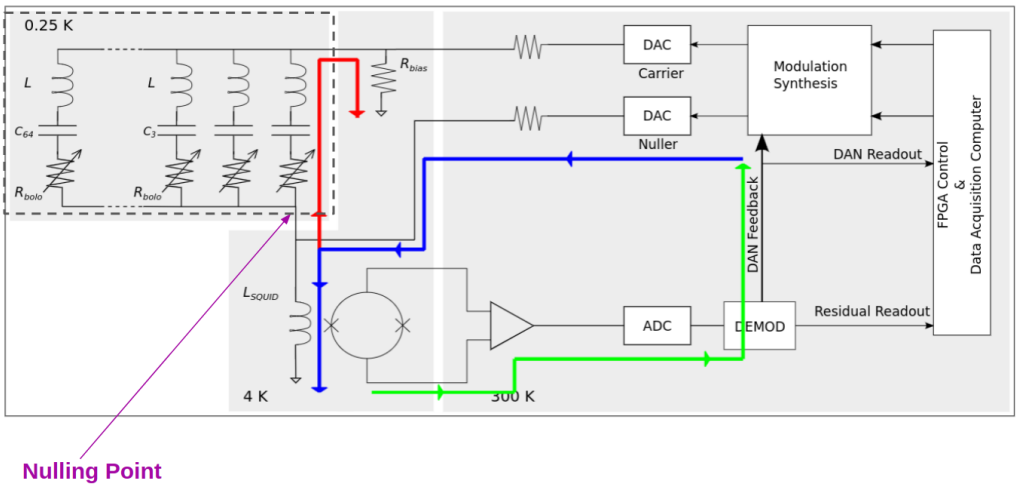

Figure 3.7: A schematic of the SPT-3G readout highlighting different parts of the circuit – the green line shows the circuit after the SQUID, the blue line shows the path of the nuller, and the red and blue line at the nulling junction show two paths to ground. Figure from Amy Bender

To make this multiplicative noise source diminish, we made the numerator of the fraction on the right hand side of equation 3.5 smaller by decreasing the input impedance of the SQUID. In the winter 2017-2018 season we replaced all of the SA4 SQUIDs (∼300 nH) with SA13 SQUIDS (∼60-80 nH). The result of this can be seen in Figure 3.8 – the readout noise was improved by roughly a factor of 2.

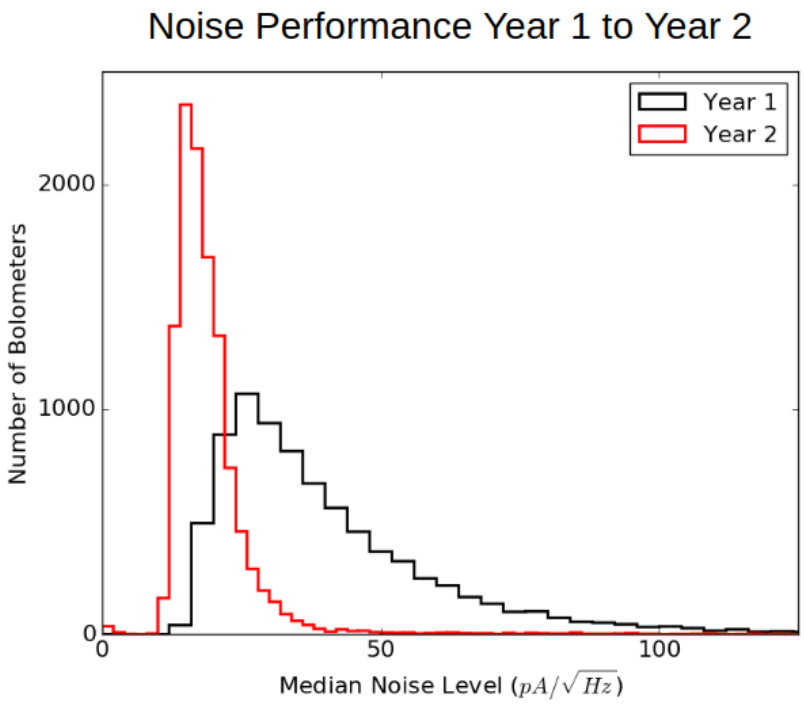

Figure 3.8: Noise improvements in the SPT-3G Receiver from Year 1 to Year 2 due to the replacement of the SQUID amplifiers.

Chapter 4

CMB Mapmaking

4.1 SPT-3G Survey

With all of the readout problems from Chapter 3 solved, I present the final readout performance for SPT-3G. One common way of quantifying noise performance is the Noise Equivalent Temperature (NET), which is the quadrature sum of all noise sources, referred back to the sky in units of fluctuation temperature. Put another way, it's what amplitude of fluctuation could be detected at 1σ in 1 second.

Figure 4.1 shows NET histograms for the 3 bands of the SPT-3G receiver. The achieved NETs are within our goals to be able to achieve low noise science over the course of the survey. The numbers for projected full survey map depth are listed in Table 4.1.

The 2019-2020 SPT-3G B-mode Angular Power Spectrum uses data from the 2019 and 2020 winter observing seasons of the SPT-3G experiment. The survey area covers approximately 1500 deg^2 (3.76% of the full sky) between -42° to -70° declination and from $20^{\mathrm{h}}40^{\mathrm{m}}0^{\mathrm{s}}$ to $3^{\mathrm{h}}20^{\mathrm{m}}0^{\mathrm{s}}$ right ascension, as depicted in Figure 4.2 in orange. The reason for selecting this

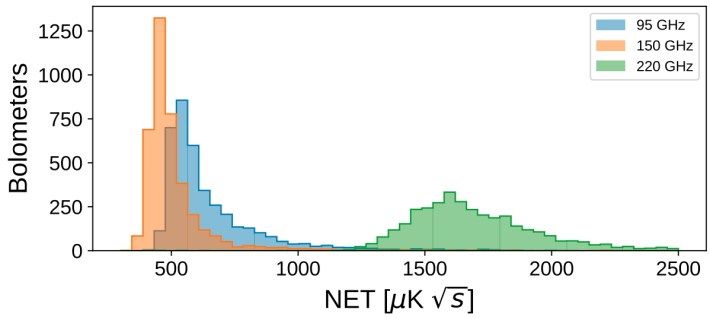

Figure 4.1: Noise Equivalent Temperature for the 90, 150, and 220 GHz bolometers in the SPT-3G focal plane. Figure from [54]

	95 GHz	150 GHz	220 GHz
Temperature	3.0 μK-arcmin	2.2 μK-arcmin	8.8 μK-arcmin
Polarization	4.2 μK-arcmin	3.1 μK-arcmin	12.4 μK-arcmin

Table 4.1: Full survey noise projections for SPT-3G [54]

field is evident when comparing to the dashed yellow line in Figure 4.2, the BICEP3 field. Having maximum overlap with the two experiments allows for SPT-3G data to be used to effectively delens BICEP3 data. Additionally, this patch is picked to be a relatively clean patch of sky visible from the South Pole, outside of the galactic plane to minimize astrophysical foregrounds. The full-field patch is broken up into four overlapping subfields with increasing declination. These subfields are centered at -44.75°, -52.25°, -59.75°, and -67.25° and are scanned using a raster scan pattern. The telescope makes sweeps across the full azimuth range of each subfield at constant elevation, then steps in elevation. The telescope scans at 1 deg/sec on the bearing (about 104 seconds to cover one scan) which means that it takes $\sim$ 2.5 hours to observe one subfield. The observing cadence is broken up into 16 hour "days" after which the cryogenics must be cycled.

4.2 Calibration

Other than the subfield observations, there are three different calibration sources that are also observed to calibrate the data from arbitrary counts units to celestial units.

RCW 38/MAT 5a

We observe two galactic star-forming HII regions, RCW 38 and MAT 5a (NGC 3576). RCW 38 is located at RA $8^{\mathrm{h}}59^{\mathrm{m}}5^{\mathrm{s}}$ and Dec 47°30'39", which makes it optimal for calibrating the two lower elevation subfields, from -56° to -42°. MAT 5a is located at RA $11^{\mathrm{h}}11^{\mathrm{m}}53^{\mathrm{s}}$ and Dec 61°18'47", which makes it optimal for calibrating the two higher elevation subfields, from 70° to 56°. We do two different kind of observations of the HII regions:

- **Weekly Dense Observation (1.5 hours):** Each week, we do a dense raster of each HII region. With these observations, each individual detector makes a complete map of the source. These maps are then used to calibrate our detectors in temperature units by comparing them to flux-calibrated maps from SPT-SZ and the Planck satellite.
- **Per-subfield Sparse Observation (10 minutes):** Before each subfield is observed, a quick scan of the HII region is done to correct for day-to-day variation in sky opacity.

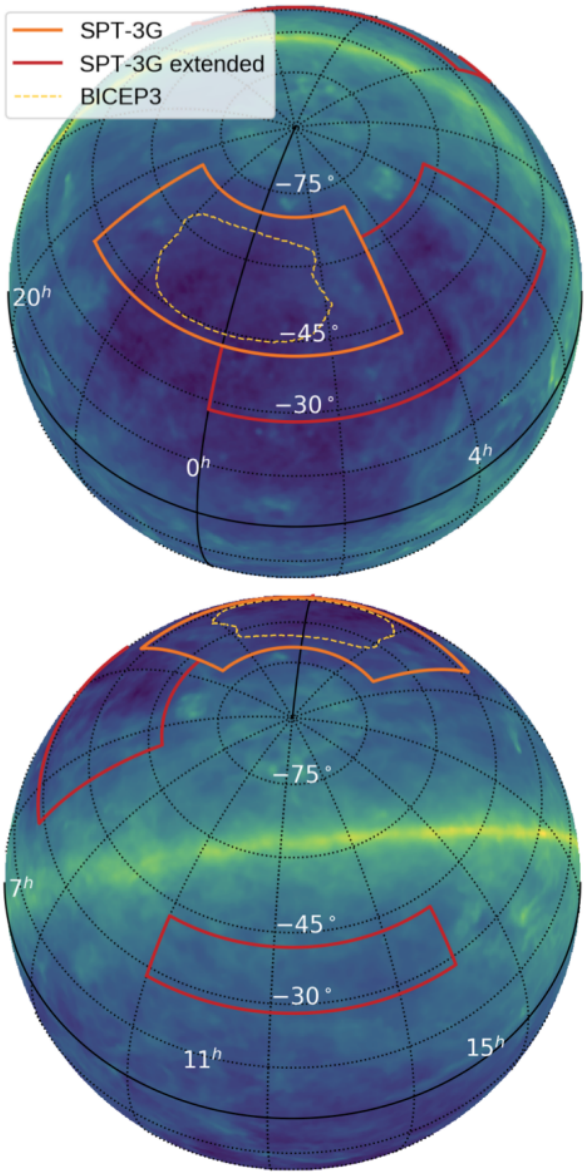

Figure 4.2: The SPT-3G survey patch, with the BICEP3 patch highlighted as well to show the overlap. Figure from [54]

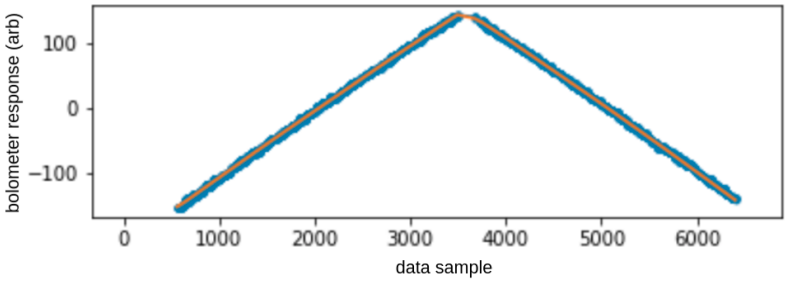

Figure 4.3: Detector response to an elevation nod

Elevation Nod

Before each observation, the telescope does an $\sim 2^\circ$ slew in elevation which we refer to as an elevation nod, or, "elnod". As seen in Figure 4.3, the change in atmospheric loading creates a large signal seen by the detector. For all SPT-3G maps, this is use to decouple the in-phase and quadrature components of the frequency demodulated time streams. For the maps used in the SPT-3G B-mode power spectrum analysis, the elnod is also used to improve the detector gains, which is explained further in Section 4.3.

Chopped Thermal Source

A chopped thermal calibration source is a necessary addition to astrophysical sources since the detector response changes as a function of sky loading. The thermal source is modulated at 4 Hz and is mounted behind the secondary mirror. For each observation, we scale the response of the detector to the calibrator at the subfield's elevation to the response to the calibrator at MAT 5a or RCW 38's elevation.

We expect the combination of these three calibration sources to be accurate to a few percent. This is good enough to set relative gains between detectors before they are combined into maps. However, we also perform a final absolute calibration to our full-field maps to foreground-subtracted Planck maps for each frequency.

4.3 Time-Ordered Data Processing

For SPT-3G data analysis, we use a mapmaker based on the MASTER "filter and bin" method [35] [42]. In this section, I will describe the filtering operations that are done to the data, how the data are weighted, and how the data are binned into maps.

Data Cuts

The time-ordered data (TOD) from these observations is at a native rate of 152.6 Hz, which is then downsampled to 76.3 Hz to conserve bandwidth for northern transfer from the South Pole via satellite. When making maps, there are a number of reasons that TOD from detectors get cut during our data quality checks:

- Response with a Signal-to-Noise < 20 to the chopped thermal source
- Detector missing in a calibration observation
- NaNs in the TOD
- Detector missing identifying information
- Detector has an unphysically low variance
- If there is an excess of glitches (deviations from a rolling average)
- Detector's readout is beyond the dynamic range
- Detector is not biased in it's superconducting transition
- TES resistance is out of an allowable range

Filtering

For the detectors that pass these data quality checks, we then subtract a 10th-order polynomial from each detector TOD to mitigate low-frequency noise sources on scales bigger than $\sim 10^\circ$. Additionally, we implement a low-pass filter at $\ell = 3000$ to eliminate aliasing of high-frequency noise beyond the spacial Nyquist frequency of the map pixel size. This transfer function over the relevant range for this analysis can be seen in Figure 4.4. Even in the lowest ℓ bins, it is not drastically attenuating the signal.

Elnod Gains

For the SPT-3G 2019-2020 B-mode analysis, the detector gains are recalibrated off the elnods instead of just using RCW 38 or MAT 5a or setting the gains by minimizing noise in the TOD (a method used in SPTpol's B-mode analysis [53]). There are a number of reasons for this:

1. **Better Signal-to-Noise:** As seen in Figure 4.3, the signal-to-noise is extremely high on an elnod, usually about a factor of 700. This is dramatically higher than the range for typical atmospheric noise (the signal that you would be matching off of) in the TOD, which has a signal-to-noise ratio of $\sim$1-100.

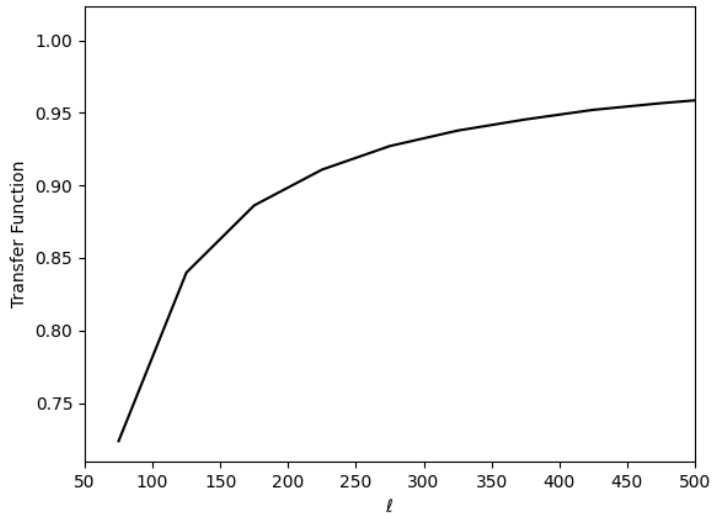

Figure 4.4: Transfer Function showing the roll-off from the 10th-order polynomial filter

2. **Less Contamination from Readout 1/f:** As opposed to minimizing the TOD to set gains, using the atmosphere elevation slews ensures that the most dominant component is the atmosphere, preventing accidentally gain matching off a different noise component.

3. **Linearity/Bias:** Calibrating off of the elnods is independent information to the science field observation data, so there is no worry about linearity or bias.

4. **Well-matched to Atmosphere:** Using the gains that come out of the calibration pipeline, the detectors are calibrated to the spectrum of RCW 38 or MAT 5a. However, the spectrum of the atmosphere is different than the spectrum of RCW 38 or MAT 5a, so to be able to most effectively minimize atmospheric noise, calibrating to elnods (the atmospheric signal) should give better cancellation.

The actual implementation of the elnod gain matching is as follows. We start with a bolometer pair (two bolometers with orthogonal polarizations in the same pixel) which we will label X and Y, and assume our data to be one scan of noiseless, temperature-only TOD. We will define g_x and g_y to be the slope of the detector's elnods, and A_x and A_y the gain-matching coefficients we hope to find.

We enforce two requirements. The first is that the signals are matched between X and Y after applying a gain-matching coefficient.

$$A_x X = A_y Y \tag{4.1}$$

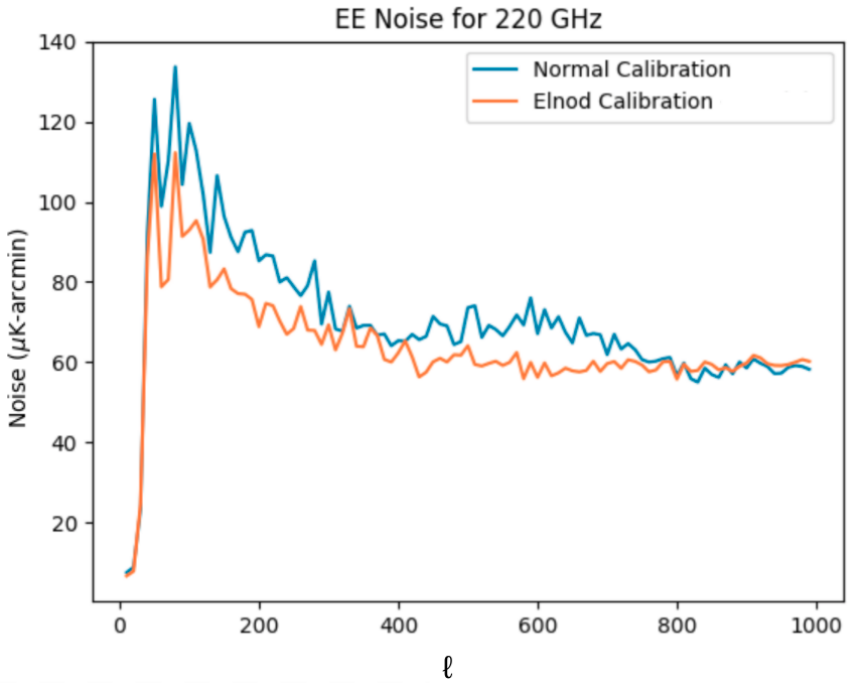

Figure 4.5: This plot was created as a quick test of the elnod gain matching. It uses ∼half of the 2019 winter season's data, and calculates the noise by using the difference between the left-going and right-going scans. The 220 GHz detectors see ∼20% improvement in noise.

The second preserves the temperature signal.

$$A_x X + A_y Y = X + Y \tag{4.2}$$

We also assume:

$$\frac{X}{g_x} = \frac{Y}{g_y} \tag{4.3}$$

which is the assumption that the elnod slopes are a good measurement of the DC detector response.

When you take these requirements into account and solve for the gain-matching coefficients, this is the solution:

$$A_x = \frac{g_x + g_y}{2g_x} \tag{4.4}$$

$$A_y = \frac{g_x + g_y}{2g_y} \tag{4.5}$$

When these new elnod gain-matching coefficients are applied to each detector, the noise is improved by up to ∼20% as shown in Figure 4.5.

One thing to note – this method does enforce a strict pair-cut. This is to say that if we cut one detector from a pixel pair in the first step, we will cut the other detector here. This does cause some loss in data volume, though not enough to outweigh the reduction in noise caused from these new gains, as evidenced by the broadband improvement in Figure 4.5.

Pair-Difference Weights

In essence, a sky map is simply a weighted average of individual detector maps. To make the lowest-noise map, a relative weighting scheme between detectors must be carefully chosen. The standard weighting scheme for SPT analyses is to weight each detector by the inverse of the power spectral density of the 1-4 Hz regime of each TOD [23]. The thought behind this frequency range is that it's a measurement of a detector's temperature white noise. For an analysis such as the SPT-3G B-mode analysis, however, the crucial thing to minimize is *polarization* noise over low-ℓ. Therefore, for this analysis, a pair-difference timestream is constructed for each pixel pair. This is just $X - Y$ for each scan using the same naming convention as before. Then, the detector is weighted by the inverse of the power spectral density of the 0.1-1 Hz regime of each pair-difference timestream. This then is constructing a weighted average of detectors that minimizes the polarization noise over the low-ℓ regime, which is the scientifically interesting one for this analysis. The improvements to noise from this method can be seen in Figure 4.6.

There are a few things to note about this method. First, it reduces data volume compared to a temperature-based weighting scheme since, like the elnod gain-matching, it drops detectors that don't have a partner in their pixel that passed data quality cuts. This can be seen in the far left panel of Figure 4.6. For the 90 GHz detectors, the noise is already so low (due to the atmosphere being less bright at lower frequencies, and therefore leaking less noise into polarization), that once out of the regime where the weight is strictly being enforced (.1-1 Hz, which roughly translates to $\ell \sim 200$), the noise actually gets *worse* by doing the pair-difference weighting scheme. This is due to the loss in data volume from enforcing the explicit pair cut. This being said, since there is so much atmosphere leaking in from low-ℓ, this *does* still help the 150 GHz and 220 GHz bands all the way up to $\ell \sim$1000.

Second, again I want to highlight the trend of increasing noise/increasing improvements from this method with band. This is highly suggestive that SPT-3G's noise problems have to do with a source that increases steeply with observing frequency band, such as the atmosphere, as a source of polarization noise. There is more discussion of the specifics of this noise source in chapter 5.

4.4 Mapmaking with HEALPix

Once the TOD are calibrated and have weights assigned to them, they can be binned into a map. In this analysis, I use the same mapmaking algorithm implemented for SPTpol and the previous SPT-3G analyses [19] [43] [33] [23] and described in [40]. We decompose the

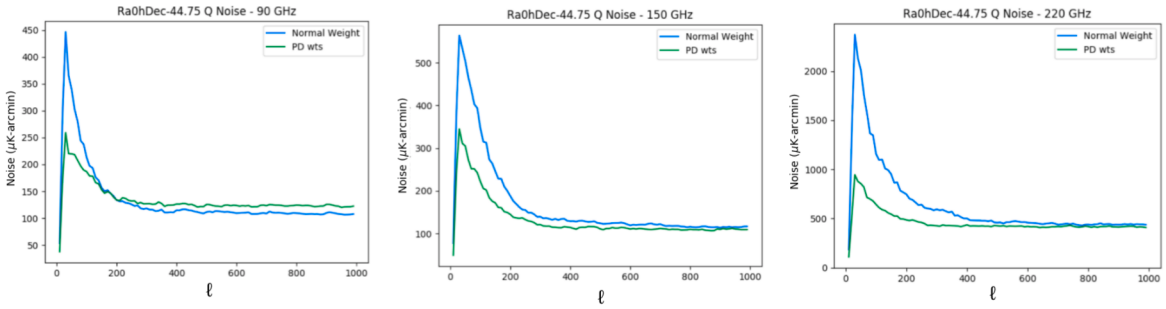

Figure 4.6: This plot was created as a quick test of the pair-difference gain matching. The three different bands are shown for the lowest subfield (where the atmosphere should be brightest, so any leakage should manifest strongest). Blue is labeled "Normal Weight" which is weighting detector timestreams by the inverse variance of the 0.1-1 Hz regime. In green is plotted "PD wts", the pair-differenced weighting scheme described in this section. This figure shows the dramatic improvement in noise from changing to a pair-difference weighting scheme.

polarization field into stokes Q and U defined by the local coordinate system such that $+Q$ corresponds to a horizontal polarization state. Each observation therefore has three maps, corresponding to stokes T, Q, and U, which can then be decomposed into E and B. They are natively stored weighted, meaning that each pixel for T, for example, is stored at $T \times w_T$ where w_T is the weight for that pixel. This is for ease in making a weighted average of all the individual observations to construct the full-field science map with all of the data.

This analysis uses HEALPix [26], which stands for **H**ierarchical **E**qual **A**rea iso**L**atitude **Pix**elation. In all previous SPT analyses, the maps were pixelized on a flat surface, however as the field gets bigger, approximating the sky as a flat patch breaks down. Problems such as E-mode to B-mode mixing and projection distortion become bigger as the patch of sky gets bigger. We use HEALPix in this analysis because we want to have a mathematical structure which supports discretization of functions on a sphere at high resolution. There are three properties that makes HEALPix quite good for this type of analysis – they are pixelated on a sphere hierarchically tessellated into curvilinear quadrilaterals. This is shown in the top image of Figure 4.7 that the lowest resolution partition is made of 12 base pixels. Resolution increases by breaking each pixel into four more, and the areas for all pixels at a given resolution are close to identical. Moving clockwise around Figure 4.7 are the first three steps from base level – 12 to 48, 192, 768. The second important property is that areas of all pixels at a given resolution are identical. The third is that pixels are distributed on lines of constant latitude. This is important because the speed of computation for spherical harmonics goes as $\mathrm{N}^{\frac{1}{2}}$ for iso-latitude as opposed to N for non iso-latitude.

Once maps are made, they are assembled into a final full-field map using the weighted average of the maps. However, care must be taken with the maps that go into the final full-

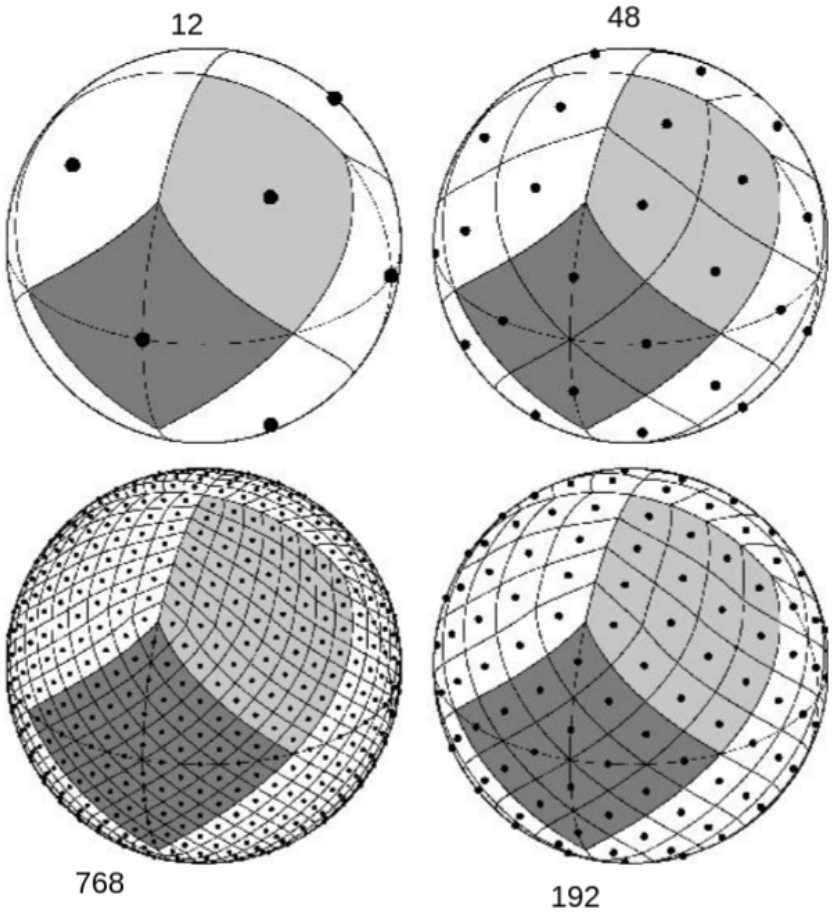

Figure 4.7: Partitions of the first three steps of HEALpix resolutions. Figure from [27]

field map. If the map weights are not perfect representations of the noise, they elevate the noise of the final full-field map by contributing to the weighted average with a higher-than-representative weight. Some ways this can happen are if there is correlated noise between detectors, or if there is non-Gaussian noise in the map. However, those two things are difficult to directly test for, so the anomalous ones are identified on a few criterion: the number of scans, the temperature weight, the temperature noise, the temperature variance, and the temperature pixel variance normalized to weight. These are then cut, and do not go into the final map.

Chapter 5

Polarized Atmosphere

When we made the maps for the SPT-3G B-mode analysis, we noticed some unexpected features in the noise. Most notable, we observed an asymmetry between the noise of the Q (horizontal and vertical) and U (+/- 45 degree) polarization states. One observation of a single subfield is shown in Figure 5.1, where this can be seen quite clearly. The 150 GHz Q map on the left side is noisy, yet the 150 GHz U map looks clean despite the identical color scale of both plots. This isn't an isolated observation; it is a commonly reoccurring phenomenon through a year of data, as seen in Figure 5.2. This is alarming because the orientation of Q and U is effectively arbitrary – any global rotation would be an equally legitimate polarization decomposition. Additionally, there is nothing astrophysical that should cause preference along one polarization state. Likewise, atmospheric temperature signals manifest in the data, but have no known mechanism to cause net polarization and fail to explain the data. In this chapter, I will present an explanation – that this asymmetry is due to noise from polarized atmosphere and explain how we mitigate this noise source in SPT-3G data. Additionally, I will provide alternative mitigation techniques that can be used by future experiments both for polarized atmosphere and for other unknown sources of polarized noise.

5.1 Characterization of Polarized Atmosphere

The Q/U asymmetry and preferential polarization aligned with the horizon is highly suggestive that the source of the noise is polarized atmosphere. Figure 5.3 shows how polarized atmosphere can manifest in telescope data. Ice crystals in the atmosphere scattering thermal radiation from the ground should produce a horizontally-polarized signal, which aligns with Q. The ice crystal size is much less than our observation wavelength, so this behaves like Rayleigh scattering. In a pure Rayleigh scattering case, this gives a frequency dependence for polarized power, P_Q:

$$P_Q = \propto \nu^{\alpha}; \alpha = 4 \tag{5.1}$$

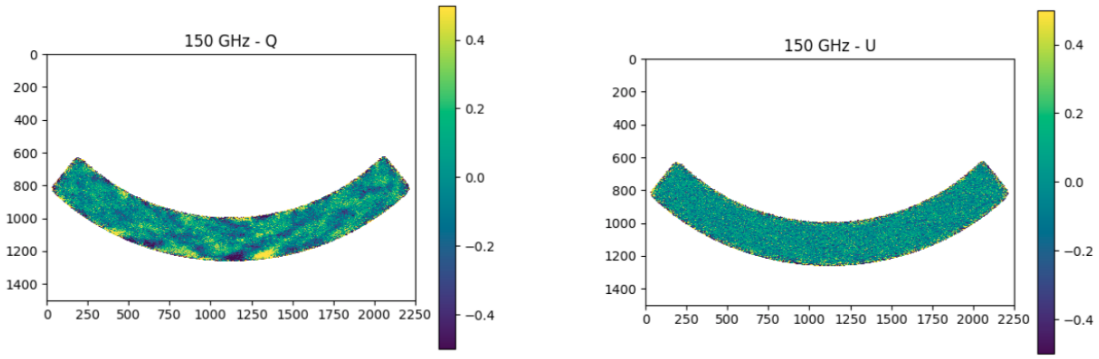

Figure 5.1: One observation that is a great example of the discrepancy between the Q and U noise – both plots are on the same (arbitrary power) color scale, yet U looks like pristine white noise, while Q is extremely noisy, especially on large angular scales.

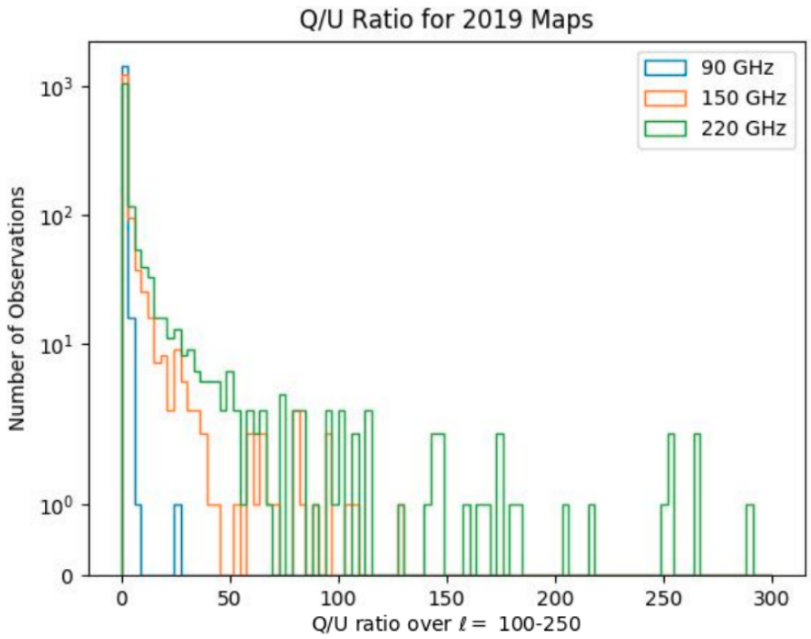

Figure 5.2: The "smoking gun" plot that something funny was up with our noise. There is no a-priori reason that we expect polarized noise to be asymmetric for a CMB experiment – nothing astrophysical should be preferentially in one polarization state. To see this level of asymmetry (Q/U ratios of 200!!) is a red flag, especially with such a strong band dependence.

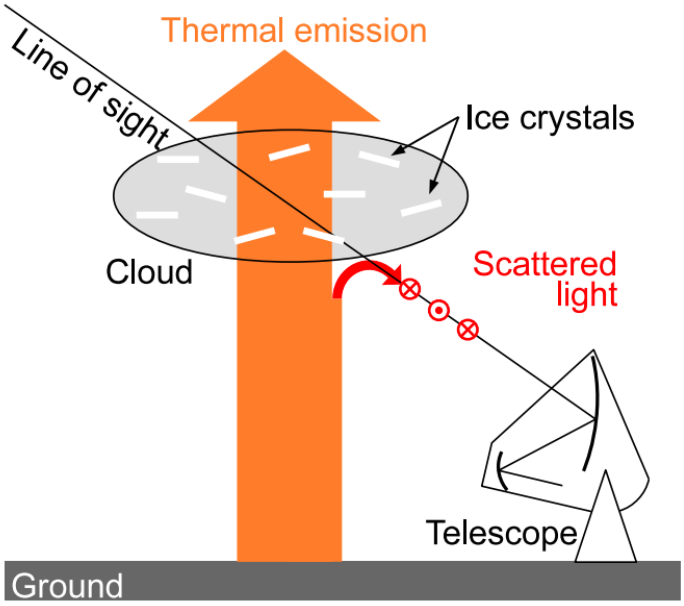

Figure 5.3: Ice crystals in the atmosphere scattering thermal radiation from the ground should produce a horizontally-polarized signal, which aligns with Q. Figure from [56]

There are a number of predictions that Rayleigh scattering by ice crystals as a noise source in our data should produce.

1. **High Q/U Power Ratio:** As seen in Figure 5.2 we expect this asymmetry between Q and U noise, since the polarized atmosphere signal is horizontally polarized.

2. **Strong Band Dependence:** As seen in Figure 5.2 this effect gets worse at higher frequencies. This is due to the steep frequency dependence seen in equation 5.1.

3. **Strong Elevation Dependence:** The atmosphere thickness increases as $\frac{1}{sin(elevation)}$. As seen in Figure 5.4, this noise asymmetry is much larger at lower elevations, where the atmosphere is thicker than higher ones.

4. **Q/U Ratio Doesn't Linearly Scale with T Power:** As seen in Figure 5.5, high Q/U doesn't show strong T dependence. This proves that temperature leakage is not the dominant source of polarized noise, exonerating many instrumental or calibration effects.

5. **Strongly ℓ Dependent:** As seen in Figure 5.6, this noise source is extremely red, causing a much higher Q/U ratio at lower ℓ. This is expected for a distribution of ice crystals determined by atmospheric turbulence [16].

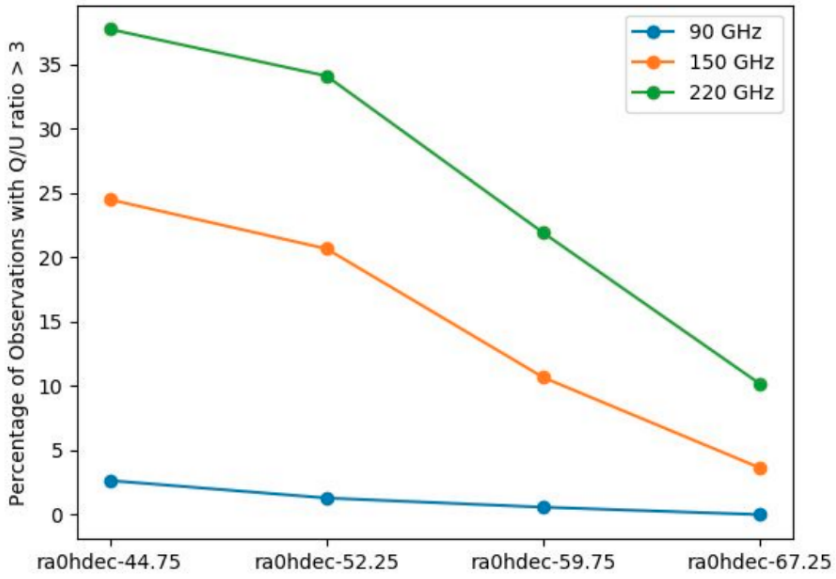

Figure 5.4: Polarized high Q noise as a function of elevation, showing higher Q/U ratios as a function of atmosphere thickness.

6. **Burst-like Structure:** Figure 5.7 shows the Q/U ratio as a function of scan, which is a proxy for time. In this figure, as the telescope scans, the polarized atmosphere signal increases and then decreases in intensity, echoing the burst-like structure previously seen in [56].

7. **Spectral Index:** As seen in Figure 5.8, the spectral index of the polarized atmosphere signal cuts off at 4, the index that would reflect pure Rayleigh scattering. This implies that the signal we see in our data is most likely some combination of thermal emission and Rayleigh scattering.

Additionally, revisiting Figure 5.6, it is important to note how diminished this effect is by $\ell = 300$. This is why this noise source hasn't been crippling to things like SPT-3G's first E-mode analysis [23], which had an effective high-pass filter around $\ell = 300$.

5.2 Removal of Polarized Atmosphere

To mitigate this noise in our data, the key is the high level of correlation between bands. This can be seen in Figure 5.9. On the top of the left side is the 150 GHz Q map for a single observation, and on the bottom of the left side is the 220 GHz Q map for the same observation. The spatial pattern is very similar, resembling two copies of an identical map.

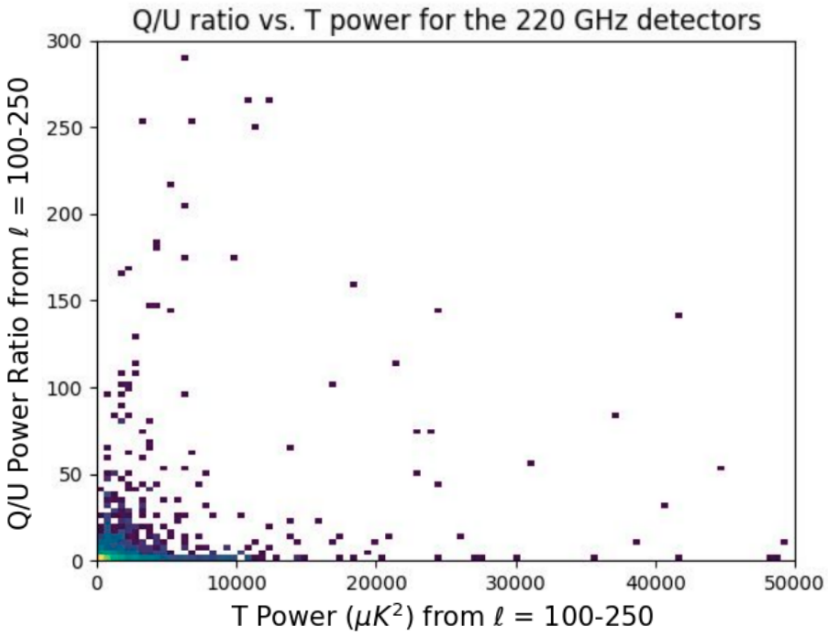

Figure 5.5: Low-ℓ T power as a function of Q/U ratio. High Q/U does not show a pattern of T dependence. This exonerates temperature leakage as the dominant source of polarized noise.

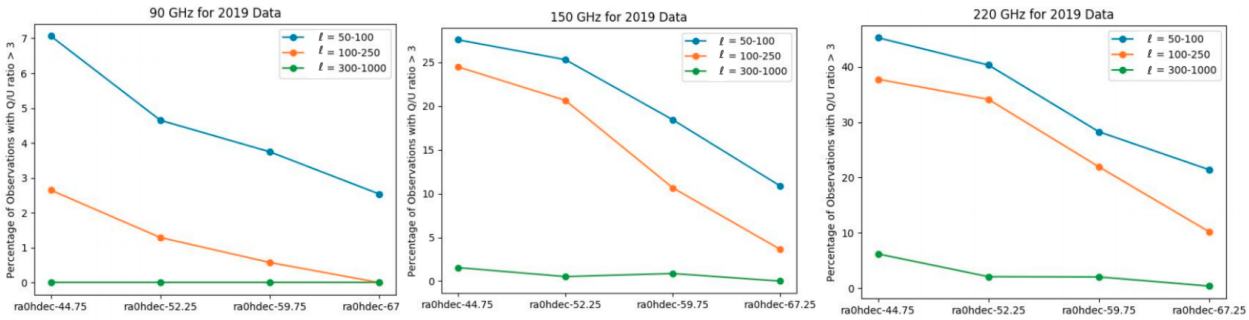

Figure 5.6: Percentage of high Q/U ratio observations as a function of ℓ range and band, showing that this noise source shows up strongest at low-ℓ and high frequency.

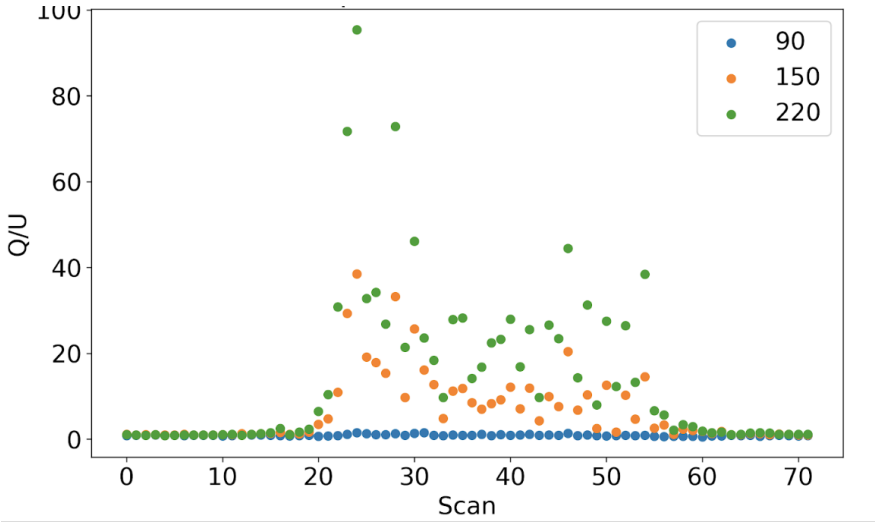

Figure 5.7: Q/U ratio as a function of scan (proxy for time) and band for one observation, showing the "burst-like" structure of the noise, and highlighting how little a dramatic "burst" in the 150 GHz and 220 GHz data can effect the 90 GHz data, underscoring the strong frequency dependence of this noise source.

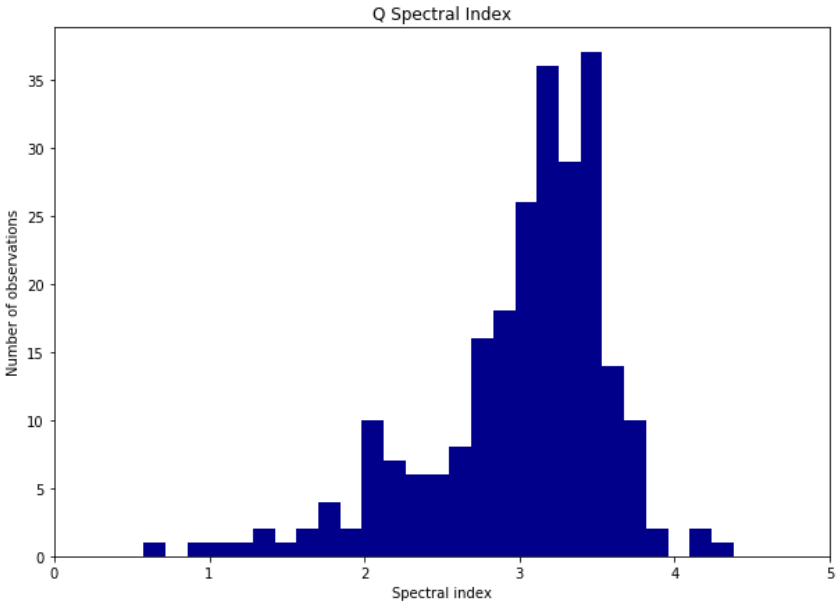

Figure 5.8: Spectral index of the Q noise for observations with a Q/U ratio > 3. Figure from Anna Coerver

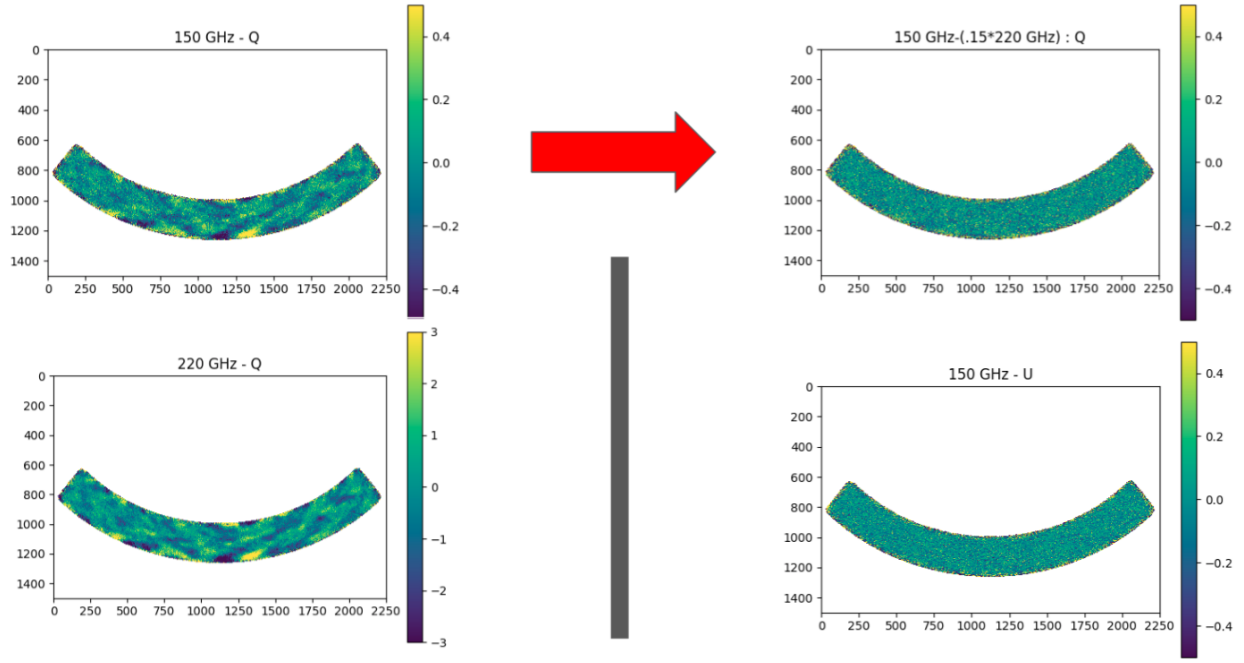

Figure 5.9: *Left Top and Bottom:* The level of correlation between SPT-3G frequency bands during high Q/U ratio days is obvious from this figure. The color scale is different, but the spatial anisotropy is the same. *Right Top and Bottom:* Once the scaled 220 GHz map has been subtracted from the 150 GHz map, the Q noise can be seen to be visibly much reduced, and very similar to the U noise below.

However, the color scale differs by almost a factor of 10 due to the steep frequency dependence of this noise. This is advantageous. Since the same underlying atmospheric signal is present in both maps, we can use the 220 GHz map to remove this signal from the 150 GHz map by subtracting a scaled version of the 220 GHz map out of the 150 GHz map. This works quite well, as can be seen on the right panel of Figure 5.9. The 150 GHz Q (top right) map is now by-eye as clean as the 150 GHz U map (bottom right). This is all done without affecting our sky signal because the sky is constant while the atmosphere changes rapidly. While deceptively simple, this implementation requires care with numerical stability. The technical details of the algorithm are described below.

There are a few ingredients that go into the polarized atmosphere subtraction code:

A 220 GHz full-season "coadd" – a weighted average of all of the observations we have in the 220 GHz band. This is a high signal-to-noise map of the 220 GHz component of the CMB[1].

[1]Although this map also contains polarized atmosphere, it is a) suppressed by the square root of the number of maps (3036), and b) even further downweighted since the maps containing polarized atmosphere

Each Individual Subfield Observation – Each subfield observation has a map file that includes T, Q, and U maps. They are natively stored weighted. As a result, when the map is loaded, each pixel in the T map is $T \times w_T$. To isolate just the signal, the weights must be divided out.

The following process is done one-by-one on every observation. The observation is then saved to disk for future use in making final science coadds:

First, a 220 GHz noise-only map is constructed.

1. Reweight the full season 220 GHz coadd by the weights for the observation 220 GHz map.

2. Subtract the reweighted full season 220 GHz coadd from the individual observation 220 GHz map to create a 220 GHz "noise-only" map for that observation. This is "noise-only" because the 220 GHz CMB signal has been subtracted, leaving only that observation's noise. This will allow for only subtracting the single observation's noise from the 150 GHz map, with no risk of biasing the CMB result.

Next, baseline power spectra are computed, and the 220 GHz "noise-only" template is subtracted from the 150 GHz map to see if it improves the map noise:

1. Compute a (heavily apodized) power spectrum for the 150 GHz map. This is the blue line in Figure 5.10, the baseline case for the 150 GHz map. The apodization addresses uneven edge coverage, and ringing from the edge of the map.

2. Multiply the 220 GHz Q "noise-only" template by an empirically determined scaling factor of 0.15. I fit the scaling factor for a random selection of maps. The power in the subtracted maps has a broad minimum near 0.15, so there is little benefit to fitting the coefficient for each observation, as can be seen in Figure 5.11. Moreover, fixing the coefficient ensures that the filtering is linear and can be easily modeled in simulations.

3. Subtract the scaled 220 GHz Q "noise-only" template from the 150 GHz Q map.

4. Recompute the power spectrum of the 150 GHz map post-subtraction. This is the orange line in Figure 5.10.

5. If the mean power in the ℓ = 50-250 range is less with the subtraction, then the subtraction is implemented on that observation. If not, the map is left as found. The rate of this can be seen in Table 5.1 – about ∼70% of the maps are found to be aided by subtracting polarized atmosphere. This doesn't mean that 70% of SPT data looks as dire as Figure 5.1; instead, it means that there is some amount of polarized atmosphere present in 70% of SPT data such that subtraction helps.

tend to be the lowest weight maps

Note the ℓ where the subtracted (orange line in Figure 5.10) and not-subtracted (blue line in Figure 5.10) power spectra cross because the rescaled 220 GHz map has a higher white noise level than the 150 GHz map. So at some point, where there are no longer any components of real polarized atmosphere to subtract above the white noise level, then doing the subtraction process elevates the noise. The solution is to low-pass filter the 220 GHz map with an ℓ cutoff of the noise crossover (labeled in the figure), so the subtraction only acts over the regime where it is helpful.

If the subtraction helps, the 220 GHz map is low-pass filtered at the crossing point so as to not elevate the 150 GHz map's high-ℓ noise:

1. Manually cut pixels in the 220 GHz map with less than 0.5% of the peak weight to avoid numerical problems with the low-pass filter.

2. Apply a Butterworth filter with the previously determined ℓ cutoff from the crossover point to the 220 GHz noise map. We use a Butterworth filter to have a maximally flat response below the stopband. See Figure 5.12 for the distribution of crossover points for one year of data (2019). This plot is illuminating because the crossover point is related to the ℓ knee, and looking at the distribution of them shows a combination of the spatial dependence of the ice signal and the relative S/N of the ice and instrument noise.

3. Multiply the Butterworth filtered 220 GHz map by the scaling factor of 0.15 and the 150 GHz weights.

4. Subtract the filtered and reweighted 220 GHz Q from the weighted 150 GHz maps.

Finally, the maps are reweighted according to the total data power in its ℓ = 50-250 range. This reweighting of the maps takes into account the difference between correlated and uncorrelated noise between detectors better than the timestream-determined weights (correlated noise will add coherently, resulting in more power, whereas uncorrelated will not). Correlated noise sources, such as polarized atmosphere, fit perfectly into this category. Note that it's not just the subtracted 150 GHz maps that are being re-weighted, but all the 90 GHz, subtracted 150 GHz, and 220 GHz maps.

1. Compute the average QQ and UU autospectrum over the ℓ = 50-250 range.

2. Rescale the weighted maps and map weights by the "map power spectrum weight" $\frac{1}{N_\ell}$ between ℓ = 50-250 of that observation.

This method is remarkably effective, as can be seen in Figure 5.13. The black dashed line, with the help of polarized atmosphere subtraction and renormalization, is brought to the orange line, demonstrating that by using these methods the 150 GHz data can be cleaned to almost the 90 GHz noise levels, despite 70% of the maps being affected at some level by polarized atmosphere. This is nearly an order of magnitude improvement in noise.

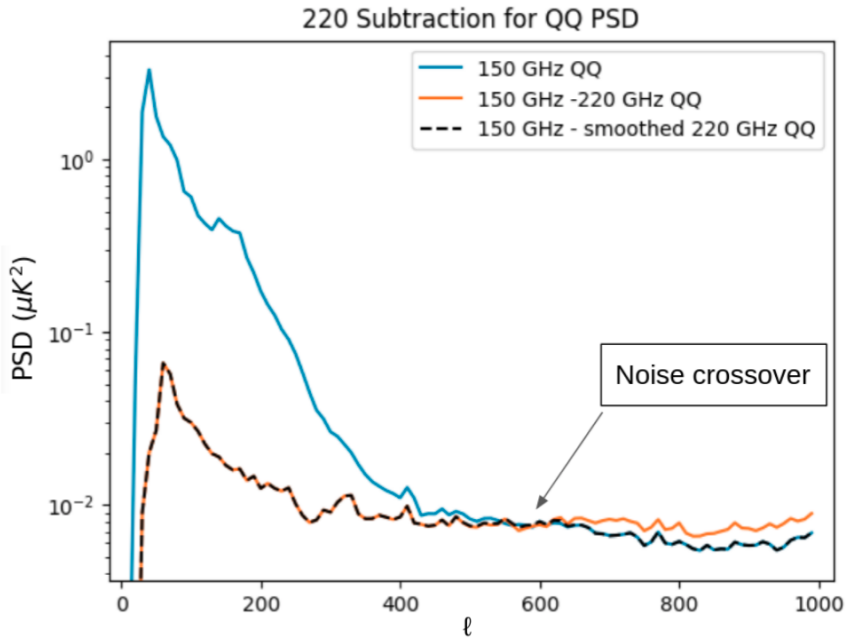

Figure 5.10: The effect the 220 subtraction (both with the Butterworth filter and without) has on the 150 GHz Q noise. The black dashed line, labeled "smoothed" refers to the Butterworth filter being applied.

Number of maps that are subtracted	1744 (70%)
Number of maps that aren't subtracted	720 (30%)

Table 5.1: Number of 150 GHz maps that are 220 GHz subtracted

5.3 Alternate Mitigation Methods

Each SPT-3G pixel has one antenna connected to six detectors, two each of 95/150/220 GHz as seen in Figure 2.5. The beams are therefore co-pointed, and two of each frequency detector see the exact same sky. We can take advantage of this, allowing us to precisely subtract maps from each other. However, many experiments do not have co-pointed beams (BICEP/Keck, for instance, or the current plans for CMB-S4). Additionally, the map subtraction technique is never a solution for the highest frequency band. This is because using the 150 GHz data to clean the 220 GHz data requires multiplying the maps by .15 instead of dividing by .15. This would have the sub-optimal effect of imprinting 6 times the noise floor of the 150 GHz data into the 220 GHz data.

In this section, I present some alternative mitigation techniques to minimize the effect of polarized atmosphere. None work as well as the map-based subtraction in terms of effec-

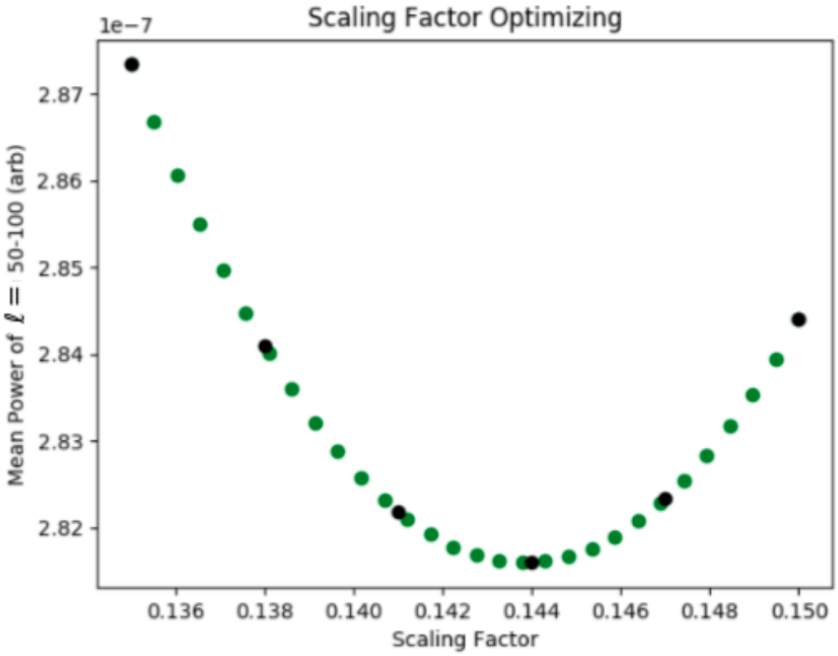

Figure 5.11: For one observation, the scaling factor with which the 220 GHz map was subtracted was optimized by sweeping around the minimum. The resulting noise power for each sweep can be seen on the y-axis. This figure shows that the optimization is quite a soft minimum (in this case, only a 1% difference from the true minimum), and that .15 works for most cases.

tiveness and computational efficiency, but they all work better than nothing!

Q Common Mode

Instead of removing excess Q power after maps are made, it can be removed from the TOD. For each scan, the excess Q noise can be isolated by solving the MASTER mapmaking equation [34] for the Q or U common mode signal on a scan-by-scan basis. This mode can be subsequently removed from the data. Here, P is a matrix encoding pointing information for each detection, $C_n =< nn^T >, n =$ noise, $y =$TOD, ψ is polarization angle of the detector.

$$\begin{pmatrix} T \\ Q \\ U \end{pmatrix} = (P^T C_n^{-1} P)^{-1} P^T C_n^{-1} y \tag{5.2}$$

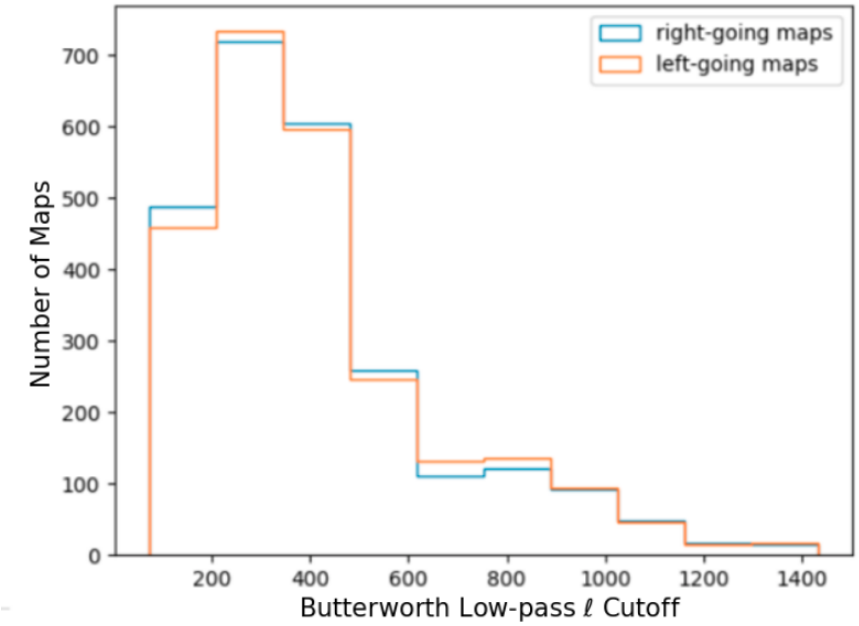

Figure 5.12: This figure shows the distribution of crossover points for all of the 2019 data. An example for one observation is shown in figure 5.10.

Limiting to only detectors with pixel-pairs:

$$\begin{pmatrix} T \\ Q \\ U \end{pmatrix} = \begin{pmatrix} \sum 1 & 0 & 0 \\ 0 & \sum_i cos^2(2\psi_i) & 0 \\ 0 & 0 & \sum_i sin^2(2\psi_i) \end{pmatrix} \begin{pmatrix} \sum_i y_i \\ \sum_i y_i cos(2\psi_i) \\ \sum_i y_i sin(2\psi_i) \end{pmatrix} \tag{5.3}$$

Solving for the Q, U, and T common mode for a scan gives results seen in Figure 5.14.

There are two physically motivated scales to calculate the common mode signal – *wafer-by-wafer*, or one common mode for the whole *array*. There are physical differences between wafers that could allow for them to have slightly different common mode signals. For example, bandpasses of one wafer might be fabricated slightly differently than of another wafer, allowing for different atmospheric response.

The performance of these two methods can be seen in Figure 5.15. As expected, subtracting the Q common mode, either by-wafer, or by-array, shows no change to U. This is good, since it demonstrates a true polarized signal and not just a leakage from temperature. Figure 5.15 also demonstrates that both subtracting a wafer-by-wafer-based common mode and an array-based common mode improves overall noise power. However, the Q common mode also filters signal as well. When correcting for the signal transfer function, the array-based common mode performs better.

In Figure 5.16 the improvement over the baseline (no common mode subtraction) case is evident. The results are shown here for the 220 GHz data for all of the 2019 observations.

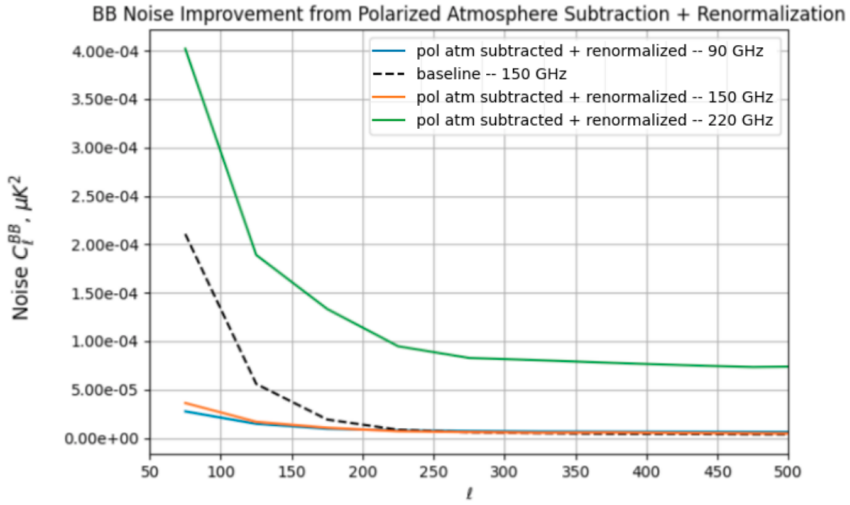

Figure 5.13: The three colored curves are the final map noise for the 2019-2020 SPT-3G BB analysis. The 90 GHz and 150 GHz curves are almost identical, proving the success of the combination of polarized atmosphere subtraction and map-based renormalization. The black dashed line shows the 150 GHz data before polarized atmosphere subtraction and map-based renormalization, which highlights the almost order of magnitude improvement by using these techniques.

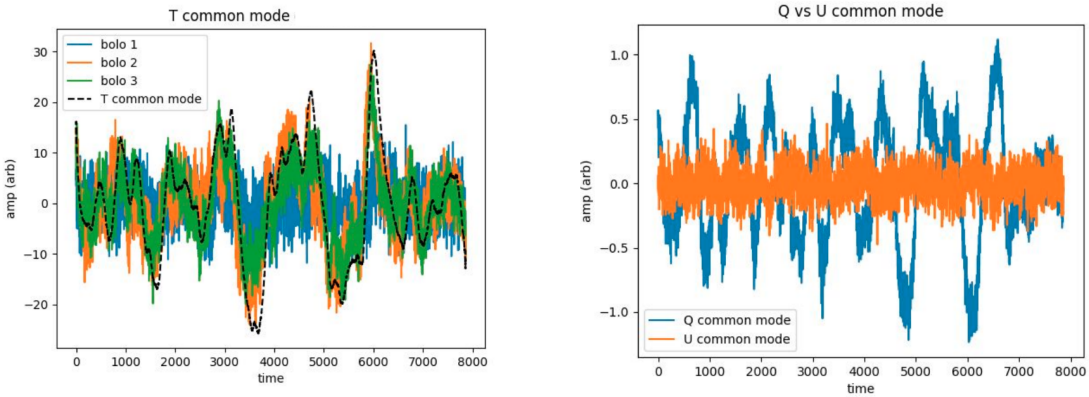

Figure 5.14: *Left:* Three bolometer's TOD are plotted. The T common mode solution solved with all the detectors in that scan scan neatly lines up, as expected. *Right:* The Q and U common mode for this scan is shown. The difference in amplitude between the Q common mode, where the polarized atmosphere signal manifests, and the U common mode is apparent. An additional thing to note – the Q common mode does not have the same structure as the T common mode, again proving that this polarized signal is not leakage.

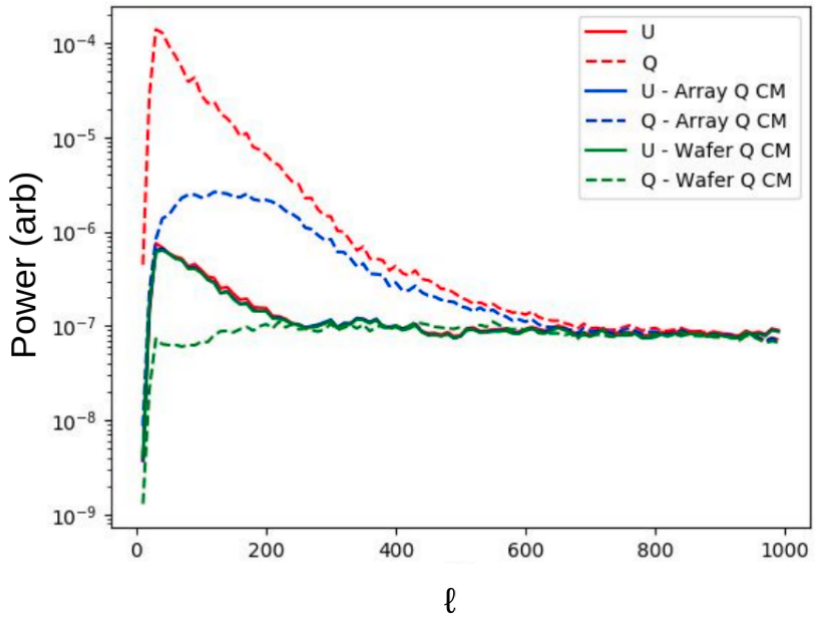

Figure 5.15: The effect of Q common mode subtraction for one observation of 220 GHz data.

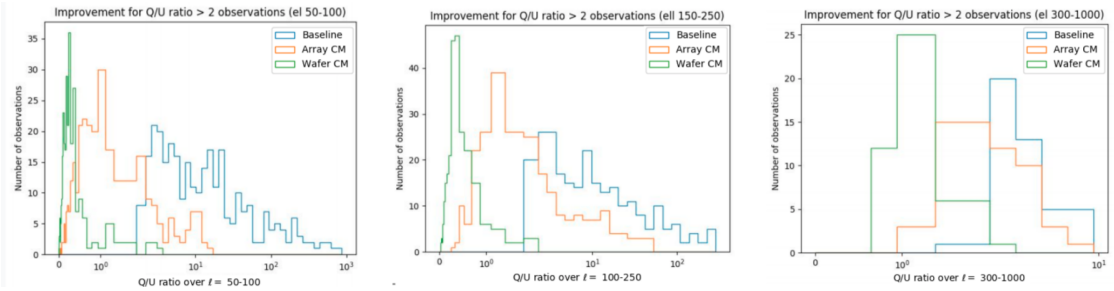

Figure 5.16: The effect of Q common mode subtraction for 220 GHz 2019 data.

As you would expect, this is a strongly band-dependent improvement.

Despite these seemingly promising results, the map-based Q-power removal works better, as evidenced in Figure 5.17. Additionally, doing a common mode is a filtering step that removes signal power, since there is no added step of removing the CMB from the data before filtering.

This may lead to the question: why did we not do Q-common mode subtraction in the SPT-3G 2019-2020 BB analysis for the 220 GHz data? Frankly, the noise of the 220 GHz detectors is so high, they wouldn't be significantly adding to the r constraining power to the point that it was worth the computational expense of calculating a different transfer

ℓ range	Baseline	Array	Wafer
50-100	301	64 (78% reduction)	3 (99% reduction)
100-250	250	113 (53% reduction)	2 (98% reduction)
300-1000	44	26 (40% reduction)	1 (97% reduction)

Table 5.2: Observations with $Q/U > 2$ for the baseline (no common mode) case, an array-based common mode, and a wafer common mode over different ℓ ranges

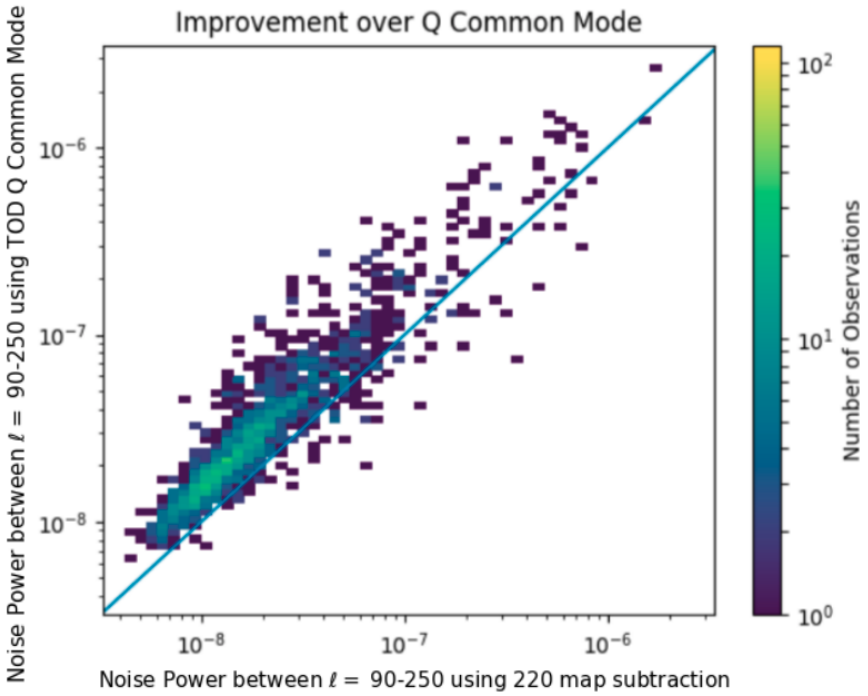

Figure 5.17: The effect of Q array-based common mode subtraction for 220 GHz 2019 data vs map-based subtraction. In both cases, the filtering transfer function has been accounted for.

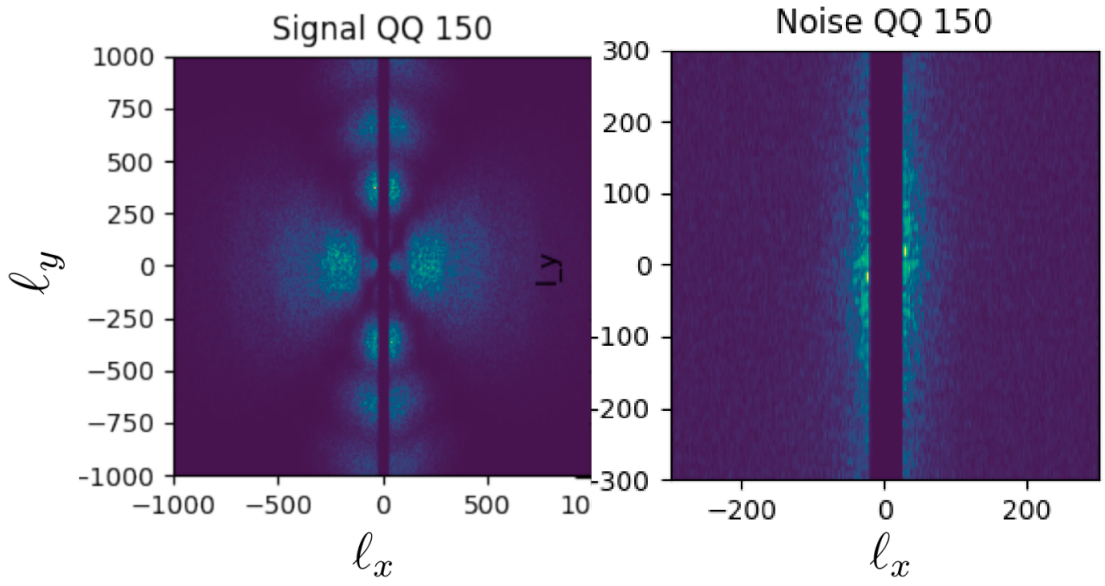

Figure 5.18: The Signal and Noise of Q data shown in 2D Fourier space.

function. Since this power removal happens at the TOD level, it has to be accounted for in simulations to properly de-bias the spectrum, and we lacked the resources to do so without serious scientific justification.

Masking in 2D Fourier space

Another interesting way to mitigate noise in power spectra analyses is to take advantage of the fact that noise sources don't appear isotropically in the 2D Fourier plane. The 1D power spectrum is formed by averaging the 2D Fourier Transform in annuli of constant ℓ centered on (0, 0). However, the noise within an annulus can vary, as seen in Figure 5.18. By weighting the contributions in each annular average, we can reduce the noise in the final 1D power spectrum.

The 2D Fourier transform shown in Figure 5.18 is made in a Cartesian projection that maps scan direction to ℓ_x and elevation to ℓ_y, and this can be used to interpret the rich structure in the plot. The signal Q map is shown on the left side of 5.18. The deep notch down the middle at $\ell_x = 0$ is the 10th order polynomial filter that kills signal at lower ℓ, and the bright spots are the EE CMB acoustic peaks. The plus structure comes from the fact that this is the Q map – the U map would show an X, and the two of them would give the full circle of polarization power. The noise Q map is on the right – note the difference in ℓ range. It is zoomed in to show where the action is happening. There are a few notable features. First is the obvious one – the fact the noise is a vertical stripe around low-ℓ, but there is no matching horizontal stripe. This is because noise terms that have a strong time dependence

show up in the scan direction, be that a cloud drifting across the focal plane, Nick Huang hitting on the cryostat with a hammer as the telescope slews causing thermal fluctuations on the focal plane, or even thermal drift of the electronics boards changing detector gains. This leads to uneven noise in all of the 2D modes that contribute to each 1D power spectrum bin. We can reduce the 1D power spectrum noise by weighting each mode in the 2D Fourier Transform.

We tested this for a subset of SPTpol data. We first made 2D Fourier transforms for both the filter transfer function (signal) and the noise. We constructed the 2D filter transfer function (signal 2D Fourier transform) by filtering white noise. To construct the noise 2D Fourier transform, we first took the 2D Fourier transform of each individual observation, followed by the variance of all the observations for each pixel in the 2D Fourier plane. When calculating the power spectrum, we weighted each bin in 2D Fourier space by the Signal-to-Noise ratio. The results can be seen in Figure 5.19. This gives a $\sim$30% improvement at $\ell = 100$ for this subset of SPTpol data. However, this plot is pessimistic, since these weights were calculated and the power spectrum estimated in the Lambert azimuthal equal-area projection, which doesn't perfectly separate ℓ_x from ℓ_y as a pure Cartesian projection. The choice to do it in Lambert azimuthal equal-area projection was simply because the flat-sky projection distortions are less in the Lambert azimuthal equal-area projection than in a pure Cartesian projection, but this is something that can be overcome through simulations and some careful power spectrum estimation code.

As maps have larger footprints in the next generation of experiments, projections such as these on the flat-sky will fall out of vogue, and everything will move to HEALpix. In this case, instead of weighting ℓ_x and ℓ_y modes, it will be weighting different a_{lm}. Eric Hivon has done some preliminary work on this for an extension to PolSpice[2] for this to be possible.

Lessons Learned from SPTpol Low-ℓ Explorations

When doing preliminary explorations of the SPTpol data set to try to understand how low in ℓ a LAT could feasibly have good performance, we found two methods to be most successful: vector cleaning and singular value decomposition. One thing to note is that these techniques were not specifically tailored to target polarized atmosphere. They were developed to be a catch-all for any source of unknown polarized noise. However, the singular value decomposition could help with mitigating polarized atmosphere since it falls into the category of (then) unknown polarized noise.

Vector Cleaning

This technique hinges on the premise that any mode that shows up stronger in Q-modulation (out of phase) data than in I-modulation (in phase) data must not be a real optical signal. This is not targeting sources of sky-based noise such as polarized atmosphere, but rather phenomenon like readout noise or other instrumental effects.

[2]http://www2.iap.fr/users/hivon/software/PolSpice/

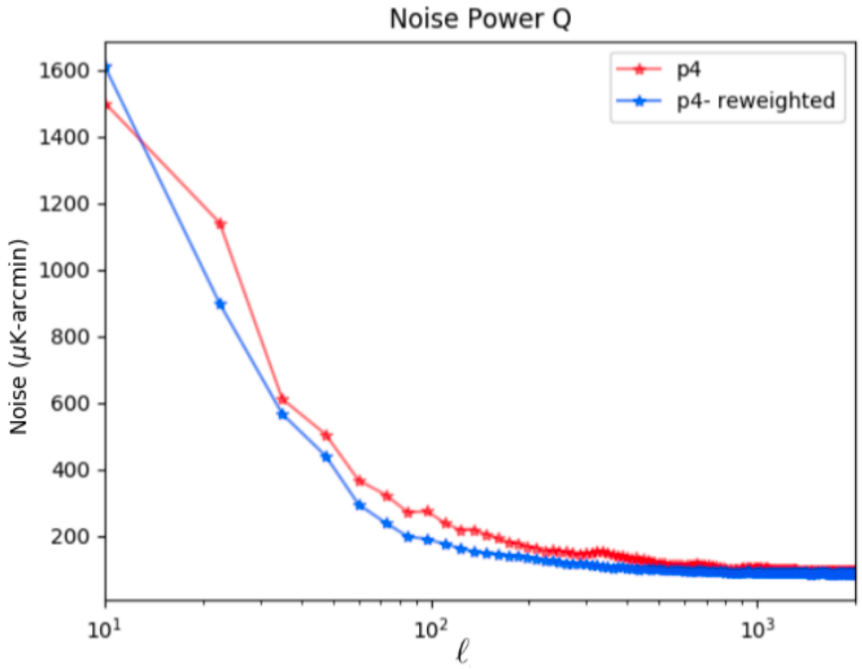

Figure 5.19: Improvements to the noise power in Q from reweighting the 2D Fourier modes based on their signal to noise when doing power spectrum estimation. The red line, p4, refers to the data having a 4th order polynomial subtracted from it as the time-domain filter. The blue line is also 4th-order-polynomial subtracted, but additionally includes the 2D reweighting of the modes before power spectrum estimation.

To isolate these modes, we first take an eigenmode decomposition of the Q-modulation (out of phase) data from all detectors in each scan. Modes in any detector with amplitude $\sqrt{I^2 + Q^2}$ greater than 3σ from zero and with a phase angle $\arctan(\frac{Q}{I})$ greater than 10° from the elnod-determined maximum responsivity phase angle are cut.

Additionally, we flag all detectors to be cut with total Q-modulation variance more than five times the I-modulation (in-phase) variance.

Principal Component Analysis/Singular Value Decomposition

This technique posits that there are also noise sources in the I-modulation data; however their correlations will be stable with time.

We use a single throw-away training observation to identify recurring low-frequency common-mode response patterns on the focal plane. The spatial pattern on the focal plane of these modes is stored, and any of the 15 largest modes from the training observation occurring later are deprojected. Because these modes have particular, white-noise-esque patterns on the focal plane, they seem to have a limited effect on the transfer function, in particular in

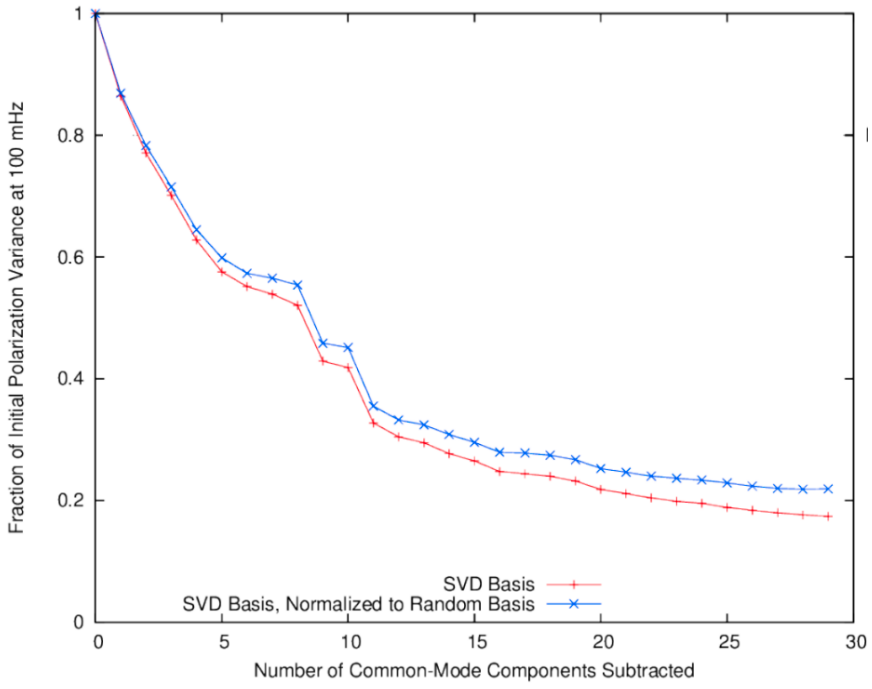

Figure 5.20: Polarization variance as a function of the number of subtracted common mode components This plot shows that there is substantial improvement in continuing to subtract modes up to about 15 modes, after which the improvement has diminishing returns.

polarization. As can be seen in Figure 5.20, one of the interesting things to note is that there is improvement in cutting up to about ∼15 modes. This implies that for SPTpol data, there isn't just one major dominant noise mode, but a number of smaller phenomenon that all contribute to the overall polarization noise. One known problem with SPTpol is clock drift, which could show up and be picked out by an SVD. However that would be only one mode. This method was originally developed to target just the clock drift, and then it worked much better than anticipated due to there seemingly existing multiple sources of noise.

For each individual observation, the deprojection procedure first uses a few (∼100) sacrifice detectors on the focal plane to fit for time-domain modes corresponding to the spatial modes in the templates. Then it deprojects those time-domain modes from each detector pair-difference timestream. This reduces the polarization variance – which pure spatial deprojection does not – while maintaining a linear and unbiased filter. If the detectors used to fit the time-domain modes are included in mapmaking, this induces a slight (4%) nonlinearity. Sacrificing these detectors preserves the linearity of the filtering.

This works quite well, as can be seen in Figure 5.21. However, it is extremely computationally expensive, and it scales with the number of detectors. When using the SPT-3G dataset, with a factor of 10 more pixels, each map's processing time would go from a few

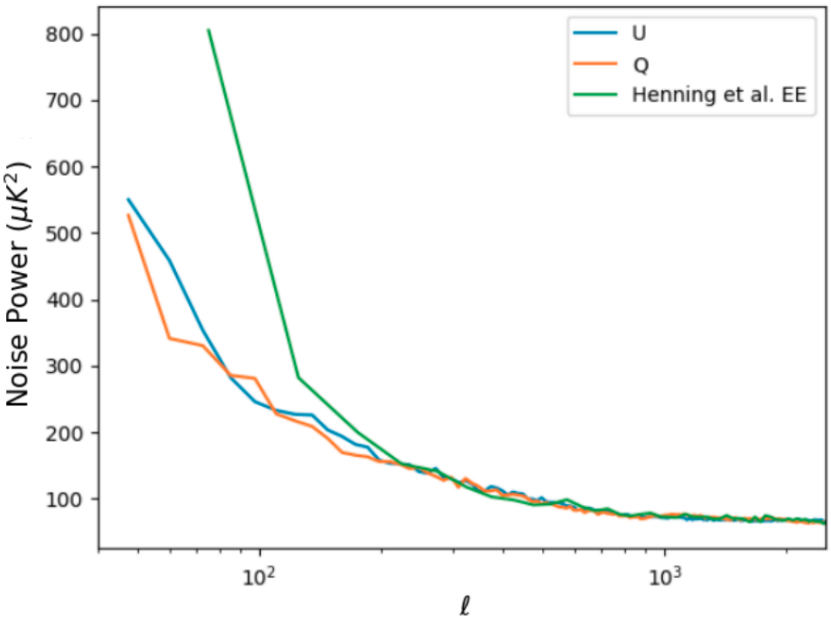

Figure 5.21: This plot compares the previously published SPTpol E-mode power spectrum noise to the noise levels achieved for this same dataset in this exploratory work. [33]

hours to days. Therefore, this method was always seen as a last resort for use with SPT-3G, and only to be implemented if we couldn't solve the noise in other ways.

Chapter 6

Null Tests

Null tests are consistency checks between different subsets of data in a given analysis to check for data systematics. We make null bundles of the individual observation maps that go into Figure 6.1 on 5 criteria:

- Moon Up or Down: The data is split based on whether the moon is above or below the horizon. This is designed to check for beam sidelobe contamination.
- Sun Up or Down: The data is split based on whether the sun is above or below the horizon. This is designed to check for beam sidelobe contamination.
- Chronological: The data is split chronologically. This is designed to check for long-term drifts in the calibration or the instrument.
- Azimuth: The data is split based on the azimuth of the field. This is designed to check ground-synchronous signals.
- Left-going versus Right-going Scans: The data is split based on the direction of motion of the telescope. This is designed to check for variations in telescope motion and temporal effects like timing offsets or errors in very long time constants.

We chose these tests to mirror the choices made for the SPT-3G E-mode power spectrum [23] based on our best guesses for what systematics could manifest in SPT-3G data. There are two tests that were done in the E-mode analysis that are not done for the B-mode analysis: a test splitting on average number of detectors flagged as saturated during an observation and a test splitting the data based on detector wafer. These tests are omitted because the SPT-3G E-mode power spectrum uses data taken in 2018, whereas the SPT-3G B-mode power spectrum uses data taken in 2019 and 2020. In 2018, there were different wafers in the focal plane which were less homogeneous and saturated more easily during field observations. The focal plane wafers were changed during the 2018-2019 austral summer season. Accordingly, for the 2019 and 2020 data used in the B-mode analysis, it is not expected that there should be data systematics correlating to wafers that were troublesome with the 2018 focal plane.

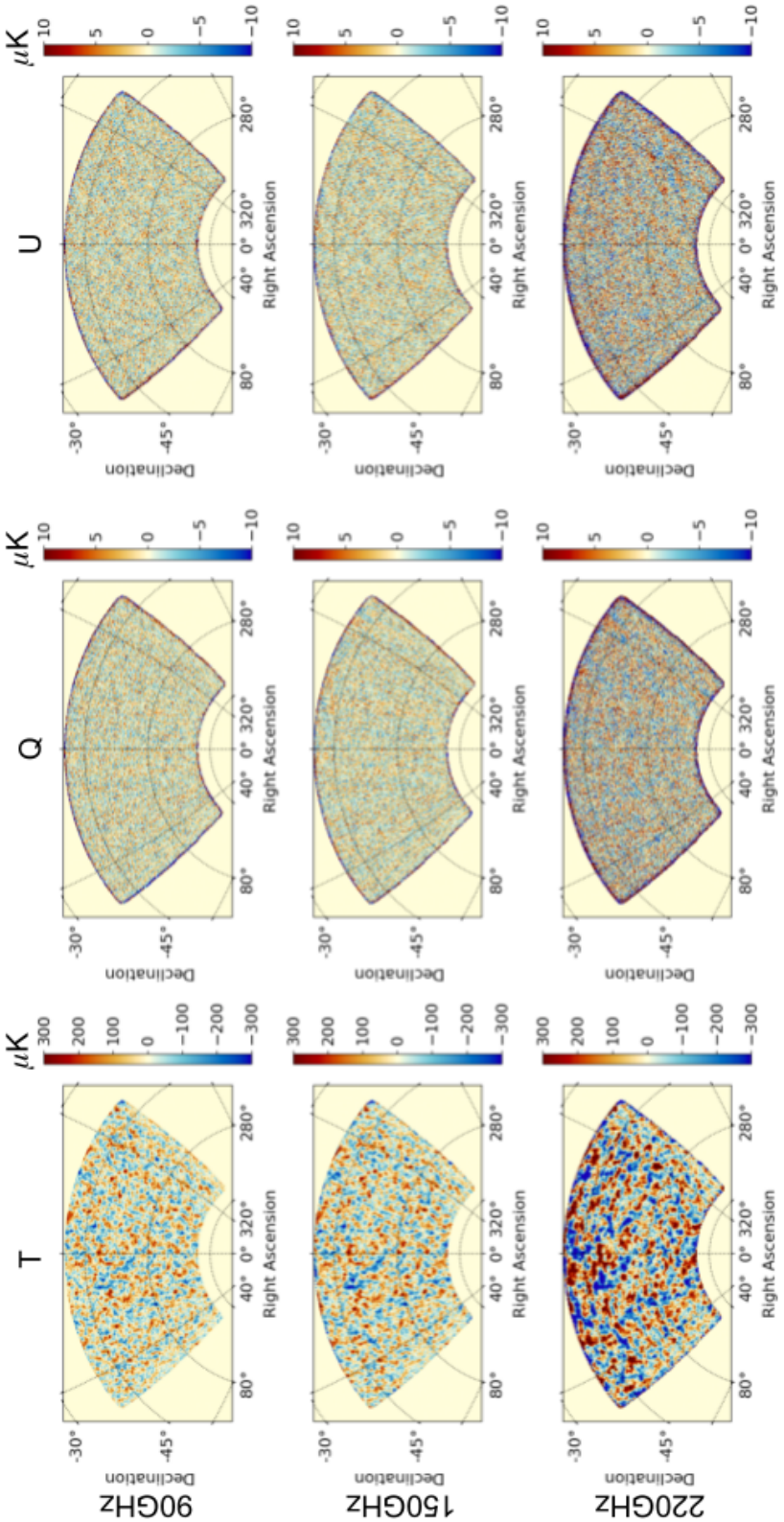

Figure 6.1: The final T, Q, and U maps for 90, 150, and 220 GHz for this analysis.

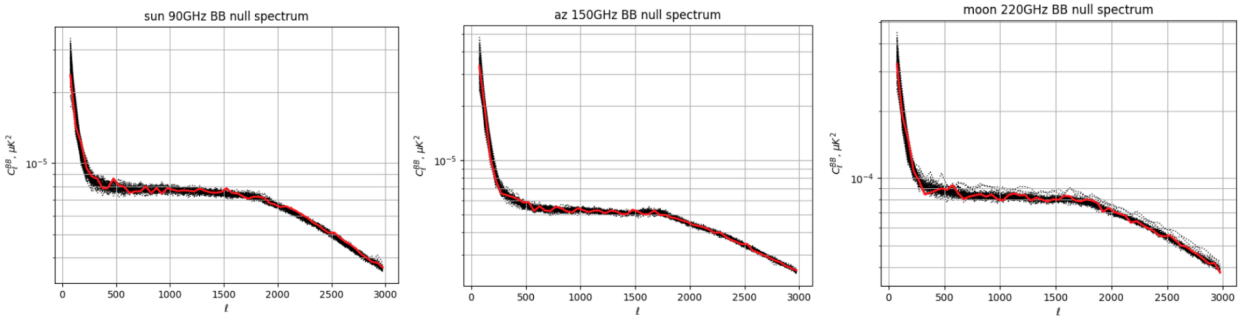

Figure 6.2: An example of a null tests for each band. *Left:* Sun Up or Down null spectrum (red) and expectation spectra (black), for the 90 GHz detectors. *Center:* Azimuth null spectrum (red) and expectation spectra (black), for the 150 GHz detectors. *Right:* Moon Up or Down null spectrum (red) and expectation spectra (black), for the 220 GHz detectors.

To construct a null test,

1. Sort maps into two bundles depending on the specific test. For example, with the moon null test, all the observations where the moon is above the horizon go into bundle 1, and all the maps where the moon is below the horizon go into bundle 2.

2. Coadd the bundles into one bundle 1 map and one bundle 2 map.

3. Subtract the bundle 1 map from the bundle 2 map to make a null map that is maximally sensitive to the specific test

4. Take the power spectrum of this map to get the null spectrum, the red lines seen in Figure 6.2.

5. To construct the expectation spectra (the black lines in Figure 6.2), randomly multiply maps in both bundles by + or -1, then subtract. Repeat 100 times.

The overarching idea with null tests is to test whether the null spectrum significantly deviates from the mean of the expectation spectra. This would be proof of a persistent data systematic that could bias the science result. To do this, we calculate the χ^2 compared to the expectation spectra:

$$\chi^2 = \sum_i \left(\frac{d_i - \langle m_i \rangle}{\sigma_{m_i}} \right)^2 \tag{6.1}$$

where d_i is the the null spectrum bandpower values, $\langle m_i \rangle$ is the mean of the expectation spectra, and σ_{m_i} is the standard deviation of the expectation spectra.

We then compute the probability to exceed (PTE) this χ^2 value given the degrees of freedom using the cumulative distribution function (CDF):

$$\text{PTE} = 1 - \text{CDF}(\chi^2, \text{dof} = \text{number of } \ell \text{ bins}) \tag{6.2}$$

One anomalously low PTE is not cause for concern, but we test to make sure that the distribution of PTE values is in good agreement with a uniform distribution.

The passing criteria for these null tests were also adopted from the SPT-3G E-mode power spectrum analysis [23]. This has two advantages: consistency with results published on the same instrument, and choosing passing criterion before looking at the table of PTEs to avoid confirmation bias. The criterion to pass are as follows:

1. The entire table of PTE values is consistent with a distribution between 0 and 1 with a Kolmogorov-Smirnov (KS) test p-value > 0.05

2. Individual PTE values are larger than $\frac{0.05}{N_{tests}}$, where N_{tests} is the number of bands $\times$ number of null tests $\times$ number of polarization combinations.

3. The combination of PTEs across each band for BB/EB/TB for each test using Fisher's method has a PTE above $\frac{0.05}{N_{rows}}$ where N_{rows} is the number of null tests.

These PTEs can be seen in Table 6.1. In this table, I have added in EE PTEs, and have shown that this analysis still passes null tests if you include all the polarized data.

Passing Criterion 1:

The first passing criteria is satisfied because without EE there is a KS test p-value of 0.24, and with EE there is a KS test p-value of 0.12. Both pass.

Passing Criterion 2:

Without EE there are 45 tests, so criterion 2 is that all of the PTE values must be larger than 0.001, which they are.

With EE, there are 60 tests, so all of the PTE values must be larger than 0.001, which they are.

Passing Criterion 3:

Whether there is EE or not, there are still 5 rows. So the combination of PTEs across each band for BB/EB/TB for each test using Fisher's method must have a PTE above .01. The results are presented in Table 6.2. All pass.

Null Test 90 GHz	BB	EB	TB	EE
azimuth	0.19	0.9	0.33	0.37
chronological	0.79	0.27	0.45	0.11
moon	0.62	0.27	0.96	0.1
left vs. right scan	0.15	0.14	0.17	0.36
sun	0.48	0.28	0.65	0.03
Null Test 150 GHz	BB	EB	TB	EE
azimuth	0.8	0.43	0.63	0.98
chronological	0.51	0.8	0.65	0.49
moon	0.42	0.42	0.36	0.6
left vs. right scan	0.65	0.29	0.67	0.79
sun	0.38	0.37	0.56	0.57
Null Test 220 GHz	BB	EB	TB	EE
azimuth	0.27	0.12	0.81	0.49
chronological	0.17	0.38	0.2	0.12
moon	0.34	0.39	0.26	0.75
left vs. right scan	0.51	0.27	0.79	0.18
sun	0.26	0.39	0.71	0.25

Table 6.1: PTE values for null tests for 90, 150 and 220 GHz data with and without EE. These values need to exceed 0.01 to pass, which they all do regardless of whether the EE data is included.

Null Test	Without EE	With EE
azimuth	0.61	0.75
chronological	0.61	0.37
moon	0.62	0.59
left vs. right scan	0.36	0.38
sun	0.66	0.37

Table 6.2: Values to satisfy passing criterion 3 for each null test, with and without the EE data.

Chapter 7

BB Power Spectrum

We can decompose the full sky of CMB temperature fluctuations using spherical harmonics, $Y_{\ell m}$ [58]. A temperature anisotropy field $\Theta(\hat{n}) = \delta T(\hat{n})/T_o$ can be expressed as:

$$\Theta(\hat{n}) = \sum_{\ell=1}^{\infty} \sum_{m=-\ell}^{\ell} a_{\ell m}^{T} Y_{\ell m}(\theta, \phi) \tag{7.1}$$

where $\hat{n}$ refers to a sky location, and $a_{\ell m}^{T}$ refers to the mode amplitudes. From this we can average over all m modes to get the power spectrum. Since the CMB is expected to be isotropic and Gaussian, all the statistical information of a given CMB map can be described by its power spectrum C_{ℓ}^{TT} given by:

$$\left\langle \Theta(\hat{n})\Theta(\hat{n'}) \right\rangle = \frac{1}{4\pi} \sum_{\ell=1}^{\infty} (2\ell+1) C_{\ell}^{TT} P_{\ell}(\hat{n} \cdot \hat{n'}) \tag{7.2}$$

Here $P_{\ell}(\hat{n} \cdot \hat{n'})$ is a Legendre polynomial of order ℓ. This is for the temperature spectrum, but as motivated in previous chapters, we need the polarization power spectrum to get inflationary constraints from CMB data. In chapters 1 and 5, we introduced Stokes Q and U, however they are not invariant under rotation. We can instead construct a new quantity that is invariant under rotation of angle ϕ

$$(Q \pm iU)(\hat{n}) = e^{\pm 2i\phi}(Q \pm iU)(\hat{n}) \tag{7.3}$$

This is a spin-2 function, so the spin weighted spherical harmonics, ${}_{s}Y_{\ell m}$ for $s = \pm 2$ [41] can be used to express the E and B mode coefficients as

$$a_{\ell m}^{E} = -({}_{2}a_{\ell m} + {}_{-2}\, a_{\ell m})/2 \tag{7.4}$$

$$a_{\ell m}^{B} = -i({}_{2}a_{\ell m} + {}_{-2}\, a_{\ell m})/2 \tag{7.5}$$

These can then be used in the same way as equation 7.1 to calculate C_{ℓ}^{EE}, C_{ℓ}^{BB} and any combination of cross-spectra.

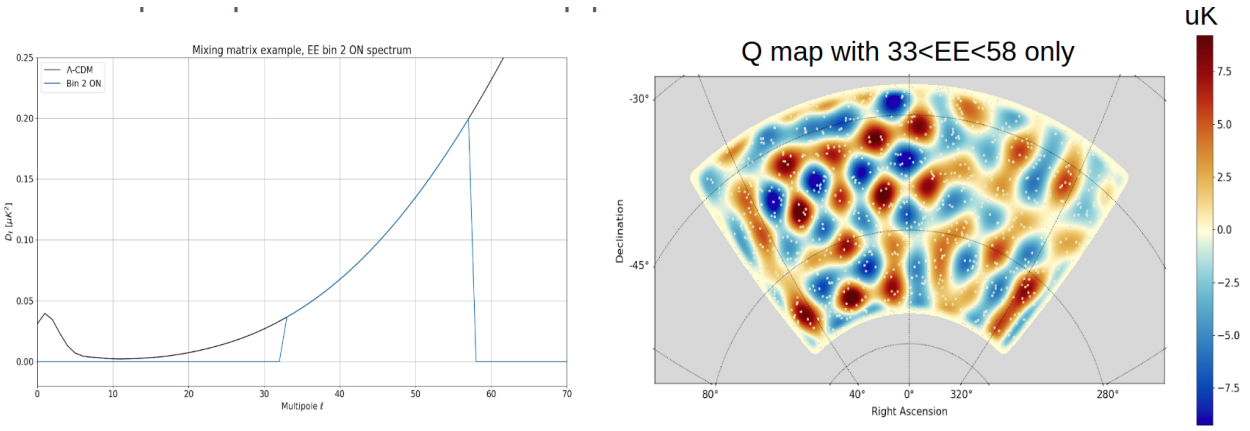

Figure 7.1: One input bin of the mode mixing matrix. *Left:* The spectrum of one bin of the mode mixing matrix. *Right:* One simulated realization of the spectrum on the left. Both figures from Riccardo Gualtieri.

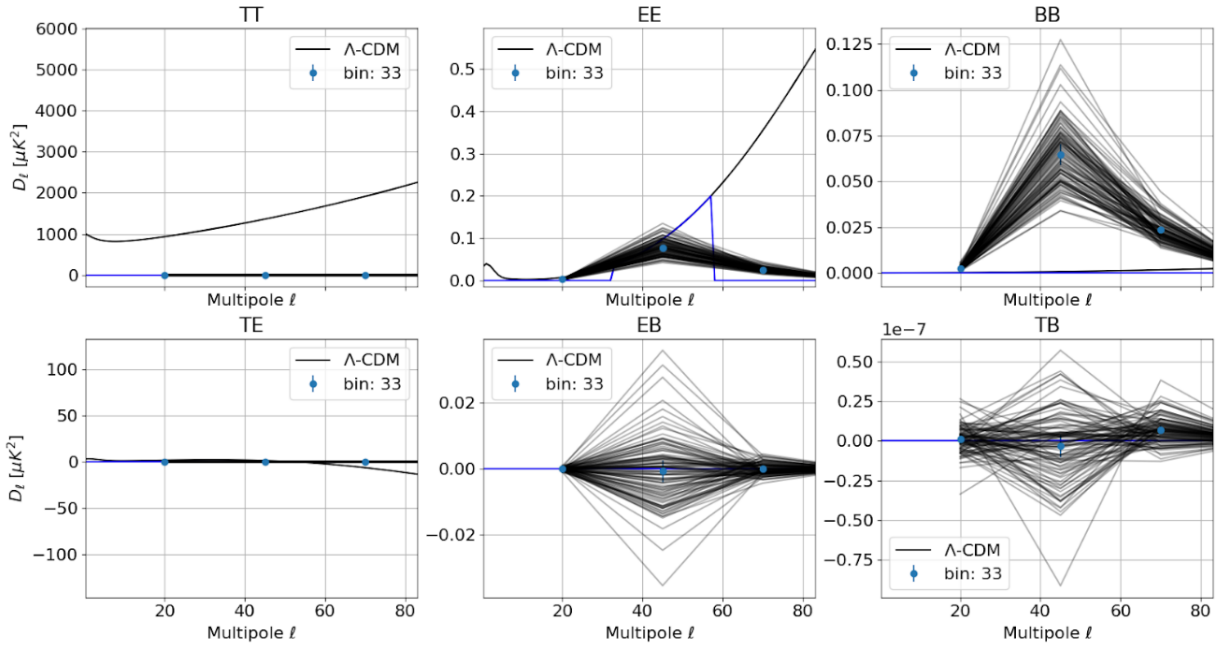

Figure 7.2: Output of mock observations of the $E-$mode input ℓ = 33-58 bin of the mixing matrix. The input is only the ℓ = 33-58 bin EE ΛCDM theory spectrum, seen in black in the top middle panel, and all the resulting power in the rest of the spectra are from mode-mixing. Figure from Riccardo Gualtieri

Additionally, power spectra of the CMB are often plotted as

$$D_\ell^X = \frac{\ell(\ell+1)}{2\pi} C_\ell^X \tag{7.6}$$

where the superscript X corresponds to a temperature-polarization combination (TT, TE, TB, EE, EB, BB).

7.1 Bandpower Estimation with PolSpice

As established in previous chapters, the maps for the SPT-3G BB analysis have sufficiently low noise and do not fail the canonical set of null tests. The remaining tasks involve taking the power spectra of the maps, debiasing them, and getting cosmological constraints. To compute power spectra from maps we use PolSpice[1] [18] [55]. We chose this code for a few reasons. First, it is computationally efficient for calculating power spectra from HEALpix maps. Second, CMB experiments, such as BICEP1 [17] or Planck [2], have used it before, so the code is well-supported for CMB analysis. Finally, Eric Hivon, one of the main developers, is part of the SPT collaboration. The observed power spectra are approximated as [35] :

$$\hat{C}_\ell^X = \sum_{\ell'} M_{\ell\ell'}^X F_{\ell'}^X B_{\ell'}^2 C_{\ell'}^X + \hat{N}_\ell^X \tag{7.7}$$

$\hat{C}_\ell$ is what PolSpice outputs. This is referred to as the "pseudo-C_ℓ" because it is a biased version of the C_ℓ, the true spectrum. To get from $\hat{C}_\ell$ to C_ℓ the other terms in the equation must be carefully characterized and removed. $M_{\ell\ell'}^X$ is a matrix that describes coupling of power between different ℓ modes due to the 3G field being a finite patch of the full sky. $F_{\ell'}^X$ is the effective filter transfer function induced by the time-domain filtering of the TOD. $B_{\ell'}^2$ takes into account instrument beam and the pixelization of the map. $\hat{N}_\ell^X$ is the noise in the map. The next few sections will go over each term in detail.

$M_{\ell\ell'}^X$ and $F_{\ell'}^X$: Mode Mixing Matrix

Each ℓ mode of the CMB is independent. However, the filtering, masking, and apodization that are a regular part of CMB data analysis on a cut patch of sky generate couplings between different ℓ modes both from the same spectrum, and from different spectra. This "mode-mixing" needs to be characterized and accounted for to reverse the effect in the final C_ℓ spectrum. For this analysis, we adapted a method developed in [46] to build up a matrix of mode mixing to invert and apply to our final power spectra. The method that we use is pretty brute force – if you want to know exactly where in the T, E, and B spectra one ℓ bin of power mixes, make a map where the input is only that bin of power, "mock-observe"

[1] `http://www2.iap.fr/users/hivon/software/PolSpice/`

[2] `https://wiki.cosmos.esa.int/planck-legacy-archive/index.php/Main_Page`

it, and then see what the output is. One example of this input is seen in Figure 7.1. This is the second lowest bin, ℓ = 33-58. In the left panel of the figure, the canonical ΛCDM spectra is in black, and the blue line shows what goes into the input map. It can be seen that between ℓ = 33-58 the input map follows the ΛCDM spectra for the E spectrum, and everywhere else is 0 (including the whole spectrum of B and T). This spectrum is then turned into a map using the synfast function in the HEALpix package [27]. One such map is shown on the right side of Figure 7.1. 100 of these maps are made for each bin, each with a random seed to lead to a different spatial realization of the same underlying power spectrum. These maps are then mock-observed. Mock-observing is a process that takes simulated skies and real recorded detector pointing information from an observation to generate simulated detector data. These simulated TOD are then processed with the same pipeline as the real data, which captures the effect of the TOD filtering, the apodization mask, and the power spectrum estimation parameters. Figure 7.2 shows the output power spectra for all the combinations of T, E, and B, where each black line is one realization. Looking first at the middle top panel, the EE spectrum, the results are as expected over the bins where we input power. The output spectrum, on average, is a slightly attenuated version of the blue input spectra. This is expected from filtering. Beyond that, however, it's evident why we need to calculate this mixing matrix. The ℓ = 68 bin has non-zero power. Additionally, the effect of E-to-B manifests in the non-zero BB spectrum. Thankfully, since this effect can be measured, it can be inverted.

So, the mode mixing matrix, pictured in Figure 7.3, is constructed. Each block consists of 21 bins, spanning ℓ = 8-508. This gives a $\Delta\ell = 25$. For each ℓ bin, 100 simulations are run with power in only T, E, or B, to make a total of 300 simulations per ℓ bin. The cross-spectra components of TE, EB, and TB are calculated as the geometric mean of $TT \times EE$, $EE \times BB$, and $TT \times BB$, respectively[3]. For each bin, the matrix is populated with the ratio between the mock observed bin average and the input bin mean value. The real sky spectra is recovered multiplying the observed spectra with the inverse of the mode mixing matrix.

The transfer function $F_{\ell'}^X$, as seen in Figure 7.4 shows the effect of filtering described in section 4.3 on the CMB signal. This is simply the diagonal of the mode mixing matrix and is included there.

$B_{\ell'}^2$: Beams

The CMB sky maps from the SPT are a convolution of the true CMB sky and the instrument's beam. The beam is the response to a point source on the sky. This is also called the point spread function. For SPT-3G, the beam is calculated using both point sources in CMB observations and raster scans of planets. The high signal-to-noise of a planet observation can characterize the beam response out to a large angular diameter ($\sim$1 degree), however detectors saturate and are potentially nonlinear when they scan too close to the planet.

[3]To account for any additional T to E leakage that is underestimated by the geometric mean, we additionally subtract the T to polarization leakage in map space.

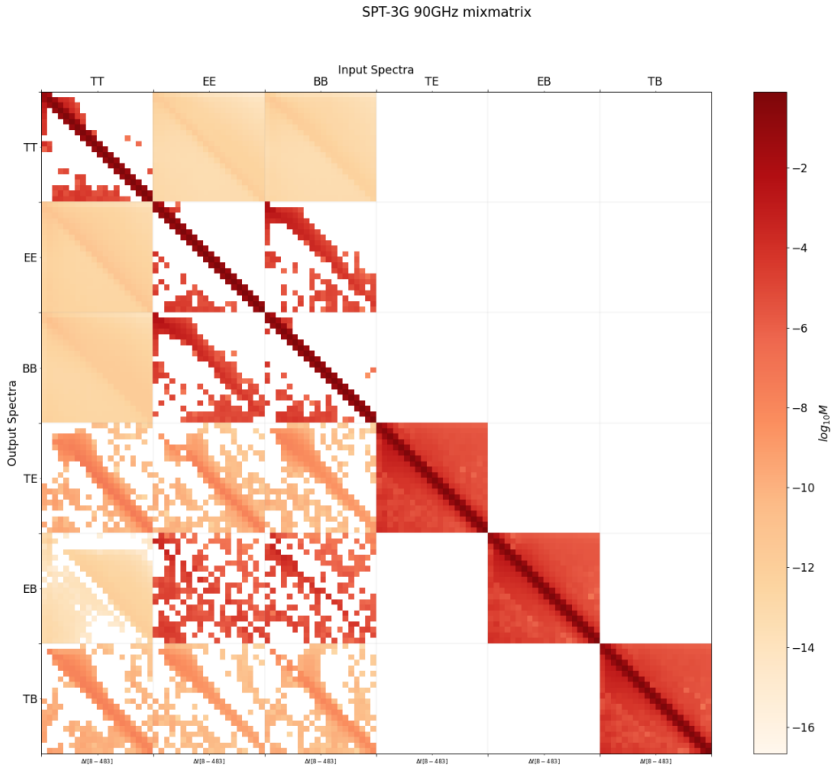

Figure 7.3: Preliminary Mode Mixing Matrix for the 90 GHz band. Figure from Riccardo Gualtieri

The point sources in the CMB fields do not saturate the detectors, but they alone don't have the signal-to-noise to measure the extended beam structure. So, a hybrid method of both point sources and planets is used. In Figure 7.5 the stitched-together beam response is shown utilizing the region where detectors aren't saturated for the planet raster, and where there is sufficient signal-to-noise on the point sources. The Fourier transform is then taken of this map, and the beam is azimuthally averaged. Additional correction is done for the finite pixelization of the map and for the planet disk. The result of this is shown in Figure 7.6 where the beam response is presented as a function of ℓ. The beam is normalized by convention to unity at $\ell = 800$. The effect of the beam can be removed from the CMB power spectra using this characterized response. The choice of normalization at $\ell = 800$ is merely conventional, but it is degenerate with the absolute calibration of the spectra.

$\hat{N}_\ell^X$: Noise Bias

For this analysis, the noise bias is calculated using "signflips," a technique utilized by previous SPT [57] and BICEP[5] analyses to characterize noise. To make one noise realization,

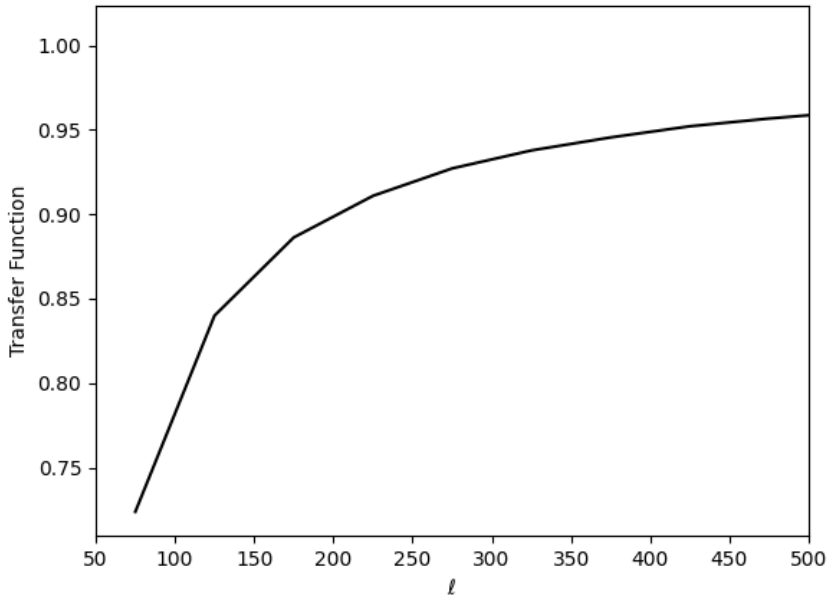

Figure 7.4: Preliminary Transfer Function

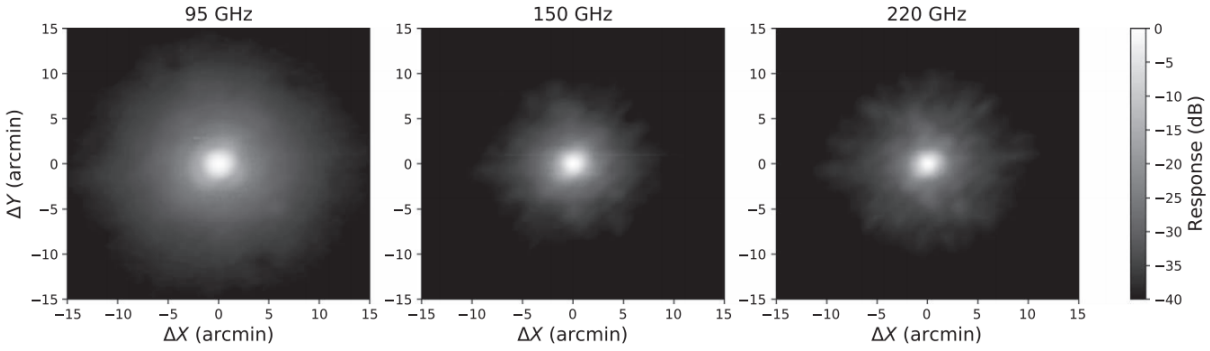

Figure 7.5: SPT-3G beam, as stitched together from both planet rasters and point sources in the field observations. Figure from [54]

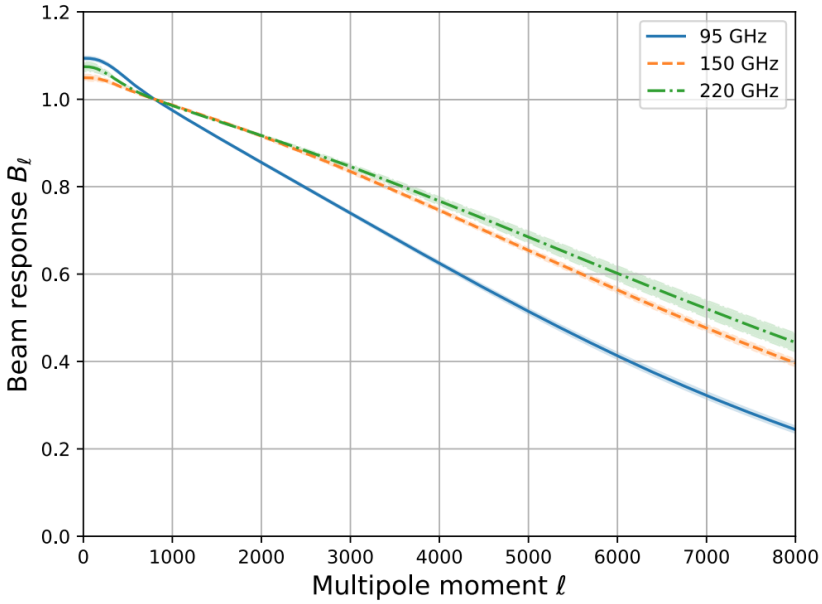

Figure 7.6: Beam response as a function of ℓ, normalized to 1 at $\ell = 800$. Figure from [54]

the data is separated randomly into two equally-weighted bundles. Then, one bundle is multiplied by -1, and the two bundles are coadded. This exactly nulls the CMB signal, and creates a noise-only "signflip" map. This process is then repeated 100 times, and the average noise map spectra can be subtracted off of the pseudospectrum to remove the noise bias.

7.2 Foreground Removal

The last detail to wrap up is to describe our treatment of foregrounds. As discussed in Chapter 1, primordial gravitational waves are not the only contribution to B-mode polarization at mm-wavelengths. As displayed in Figure 7.7, the amplitude of foregrounds are larger than the best constraints on the amplitude of r. There are two main foregrounds that we deal with for B-mode polarization – galactic synchrotron emission, synchrotron emission from polarized point sources, and polarized dust[4]. There are two ways to deal with foregrounds in data – subtracting off the contribution from foregrounds from the debiased B-mode power spectrum, or subtracting a dust map from the data maps before computing the power spectrum. The dust spectrum, as seen in Figure 7.7, increases in amplitude with frequency. We construct a template from the Planck 353 GHz maps, which are described in [6]. We

[4]Asymmetric dust grains are aligned with the ambient galactic magnetic field, and they produce polarized emission from two mechanisms. First, they absorb preferentially to their long axis, which makes the starlight backlighting them net polarized. Second, this absorbed light emits thermally on their long axis.

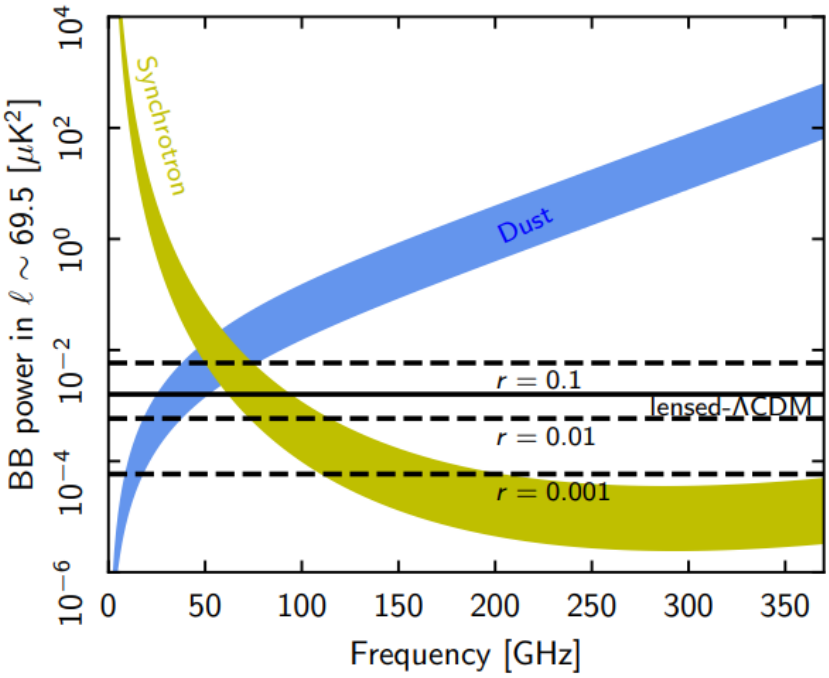

Figure 7.7: Galactic dust and synchrotron BB power at from a bin centered at $\ell = 69.5$ for the mm-wave band. Figure from [8]

choose this band because it is close enough in frequency space to avoid decorrellation, but high enough in frequency space to ensure high signal-to-noise on the dust modes. We want a template that is purely dust, so we remove the CMB from the Planck 353 GHz map by subtracting the Planck 100 GHz map. We then mock-observe this template to include the effects of this analysis' TOD filtering choices. We fit this dust-only template to our Q and U maps, and subtract this contribution from our data.

7.3 Power Spectrum

To understand our constraints on primordial gravitational waves, in Figure 7.8 I compare our spectrum error bars to theory curves for lensing B-modes and for gravitational wave B-modes with $r = 0.1$. This figure is very heartening– the maps pass null tests, they don't show spurious features, and their error bars are small. The error bars from this analysis are very small compared to the different components of B-mode emission in the mm-wavelengths, implying strong inflationary constraints from this spectrum, the most stringent from a large aperture telescope.

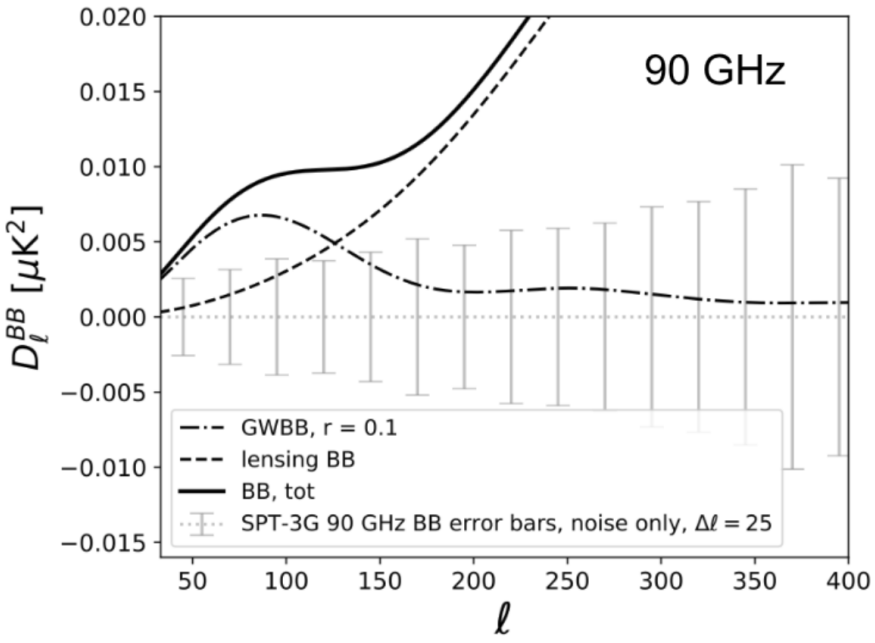

Figure 7.8: A comparison between the BB error bars and a gravitational wave BB theory curve, showing the constraining power of this data set.

7.4 Discussion

Looking back at this whole thesis, I set out to prove that a large aperture telescope could competitively constrain r. When considering the strategy for the CMB field going forward, the knowledge that with 2 years of data a LAT has this noise performance is powerful proof that LAT data can be used in r constraints for CMB-S4. That being said, this noise performance was only achieved through careful mitigation of noise sources and the analysis tools developed in this thesis. In order for CMB-S4 to be able to harness the power of the LAT for inflationary constraints (and to maximize the constraining power of the SATs, both at the South Pole and in Chile), mitigating polarized atmosphere is going to play a big role. Strategies for mitigating polarized atmosphere that could be applied to CMB-S4 include: 1) designing observation strategies so that multiple telescopes observing the same field are not pointed at the same part of the field simultaneously, thereby decreasing the signal-to-noise of any one realization of atmosphere in the final maps, 2) scanning telescopes as fast as possible to reduce the signal-to-noise of a given atmospheric realization, 3) fabricating detectors with co-pointing beams for multiple frequency bands to take advantage of the subtraction methods I outlined in chapter 5, and 4) having dedicated high-frequency channels to monitor polarized atmosphere. The impact of all of these choices can be calculated with careful forecasting to understand noise trade-offs, a project I hope to work on in the near future.

It has been a question of active discussion within the community whether a LAT could

ever achieve the low-ℓ performance of a SAT. This work has shown that with careful characterization and mitigation of noise sources, a LAT can achieve high sensitivity at low-ℓ. The techniques presented here combat sources of noise that can limit the constraining power of both SATs and LATs. This work serves both as demonstration of a LAT achieving high sensitivity at low-ℓ and as a study of atmospheric noise that will inform the design and operation of future LAT and SAT telescopes.

Bibliography

[1] Kevork N Abazajian et al. "CMB-S4 science book". In: *arXiv preprint arXiv:1610.02743* (2016).

[2] S Adachi et al. "A Measurement of the Degree-scale CMB B-mode Angular Power Spectrum with POLARBEAR". In: *The Astrophysical Journal* 897.1 (2020), p. 55.

[3] PAR Ade et al. "Improved constraints on primordial gravitational waves using Planck, WMAP, and BICEP/Keck observations through the 2018 observing season". In: *Physical review letters* 127.15 (2021), p. 151301.

[4] Peter Ade et al. "The Simons Observatory: science goals and forecasts". In: *Journal of Cosmology and Astroparticle Physics* 2019.02 (2019), p. 056.

[5] Peter AR Ade et al. "Detection of B-mode polarization at degree angular scales by BICEP2". In: *Physical Review Letters* 112.24 (2014), p. 241101.

[6] Nabila Aghanim et al. "Planck 2018 results-I. Overview and the cosmological legacy of Planck". In: *Astronomy & Astrophysics* 641 (2020), A1.

[7] Simone Aiola et al. "The Atacama Cosmology Telescope: DR4 maps and cosmological parameters". In: *Journal of Cosmology and Astroparticle Physics* 2020.12 (2020), p. 047.

[8] Y Akrami et al. "Planck 2018 results-XI. Polarized dust foregrounds". In: *Astronomy & Astrophysics* 641 (2020), A11.

[9] Donald H Andrews et al. "Attenuated superconductors I. For measuring infra-red radiation". In: *Review of Scientific Instruments* 13.7 (1942), pp. 281–292.

[10] JS Avva et al. "Design and assembly of SPT-3G cold readout hardware". In: *Journal of Low Temperature Physics* 193.3 (2018), pp. 547–555.

[11] Daniel Baumann et al. "Probing inflation with CMB polarization". In: *AIP Conference Proceedings*. Vol. 1141. 1. American Institute of Physics. 2009, pp. 10–120.

[12] Amy N Bender et al. "Digital frequency domain multiplexing readout electronics for the next generation of millimeter telescopes". In: *Millimeter, Submillimeter, and Far-Infrared Detectors and Instrumentation for Astronomy VII*. Vol. 9153. SPIE. 2014, pp. 430–444.

[13] AN Bender et al. "Integrated performance of a frequency domain multiplexing readout in the SPT-3G receiver". In: *Millimeter, Submillimeter, and Far-Infrared Detectors and Instrumentation for Astronomy VIII*. Vol. 9914. SPIE. 2016, pp. 321–331.

[14] AN Bender et al. "On-sky performance of the SPT-3G frequency-domain multiplexed readout". In: *Journal of Low Temperature Physics* 199.1 (2020), pp. 182–191.

[15] B Assa Benson et al. "SPT-3G: a next-generation cosmic microwave background polarization experiment on the South Pole telescope". In: *Millimeter, Submillimeter, and Far-Infrared Detectors and Instrumentation for Astronomy VII*. Vol. 9153. SPIE. 2014, pp. 552–572.

[16] RS Bussmann, WL Holzapfel, and CL Kuo. "Millimeter wavelength brightness fluctuations of the atmosphere above the South Pole". In: *The Astrophysical Journal* 622.2 (2005), p. 1343.

[17] H Cynthia Chiang et al. "Measurement of cosmic microwave background polarization power spectra from two years of BICEP data". In: *The Astrophysical Journal* 711.2 (2010), p. 1123.

[18] Gayoung Chon et al. "Fast estimation of polarization power spectra using correlation functions". In: *Monthly Notices of the Royal Astronomical Society* 350.3 (2004), pp. 914–926.

[19] AT Crites et al. "Measurements of E-Mode Polarization and Temperature-E-Mode Correlation in the Cosmic Microwave Background from 100 Square Degrees of SPTpol Data". In: *The Astrophysical Journal* 805.1 (2015), p. 36.

[20] Robert H Dicke et al. "Cosmic black-body radiation." In: *The Astrophysical Journal* 142 (1965), pp. 414–419.

[21] MA Dobbs et al. "Frequency multiplexed superconducting quantum interference device readout of large bolometer arrays for cosmic microwave background measurements". In: *Review of Scientific Instruments* 83.7 (2012), p. 073113.

[22] Scott Dodelson. *Modern cosmology*. Elsevier, 2003.

[23] D Dutcher et al. "Measurements of the E-mode polarization and temperature-E-mode correlation of the CMB from SPT-3G 2018 data". In: *Physical Review D* 104.2 (2021), p. 022003.

[24] Tom Essinger-Hileman et al. "The Atacama B-Mode Search: CMB Polarimetry with Transition-Edge-Sensor Bolometers". In: *AIP Conference Proceedings*. Vol. 1185. 1. American Institute of Physics. 2009, pp. 494–497.

[25] DJ Fixsen et al. "The cosmic microwave background spectrum from the full cobe* firas data set". In: *The Astrophysical Journal* 473.2 (1996), p. 576.

[26] Krzysztof M Gorski et al. "HEALPix: A framework for high-resolution discretization and fast analysis of data distributed on the sphere". In: *The Astrophysical Journal* 622.2 (2005), p. 759.

[27] Krzysztof M Gorski et al. "The healpix primer". In: *arXiv preprint astro-ph/9905275* (1999).

[28] Alan H Guth. "Inflation and the new era of high precision cosmology". In: *Physics@ MIT* (2002), pp. 28–39.

[29] Alan H Guth. "Inflationary universe: A possible solution to the horizon and flatness problems". In: *Physical Review D* 23.2 (1981), p. 347.

[30] M Chiara Guzzetti et al. "Gravitational waves from inflation". In: *La Rivista del Nuovo Cimento* 39.9 (2016), pp. 399–495.

[31] Dongwon Han et al. "The Atacama Cosmology Telescope: delensed power spectra and parameters". In: *Journal of Cosmology and Astroparticle Physics* 2021.01 (2021), p. 031.

[32] K Hattori, POLARBEAR collaboration, et al. "Frequency domain multiplexed readout of kilopixel arrays of transition edge sensor bolometers". In: *Society of Photo-Optical Instrumentation Engineers (SPIE) Conference Series], Society of Photo-Optical Instrumentation Engineers (SPIE) Conference Series*. 2014.

[33] JW Henning et al. "Measurements of the temperature and E-mode polarization of the CMB from 500 square degrees of SPTpol data". In: *The Astrophysical Journal* 852.2 (2018), p. 97.

[34] Eric Hivon et al. "Master of the cmb anisotropy power spectrum: a fast method for statistical analysis of large and complex cmb data sets". In: *Arxiv preprint astro-ph/0105302* ().

[35] Eric Hivon et al. "Master of the cosmic microwave background anisotropy power spectrum: a fast method for statistical analysis of large and complex cosmic microwave background data sets". In: *The Astrophysical Journal* 567.1 (2002), p. 2.

[36] Wayne Hu and Martin White. "A CMB polarization primer". In: *arXiv preprint astro-ph/9706147* (1997).

[37] Edwin Hubble. "A relation between distance and radial velocity among extra-galactic nebulae". In: *Proceedings of the national academy of sciences* 15.3 (1929), pp. 168–173.

[38] Kent D Irwin and Gene C Hilton. "Transition-edge sensors". In: *Cryogenic particle detection*. Springer, 2005, pp. 63–150.

[39] Kent D Irwin et al. "Thermal-response time of superconducting transition-edge microcalorimeters". In: *Journal of Applied Physics* 83.8 (1998), pp. 3978–3985.

[40] William C Jones et al. "Instrumental and analytic methods for bolometric polarimetry". In: *Astronomy & Astrophysics* 470.2 (2007), pp. 771–785.

[41] Marc Kamionkowski, Arthur Kosowsky, and Albert Stebbins. "Statistics of cosmic microwave background polarization". In: *Physical Review D* 55.12 (1997), p. 7368.

[42] Elina Keihänen et al. "Making cosmic microwave background temperature and polarization maps with MADAM". In: *Astronomy & Astrophysics* 510 (2010), A57.

[43] R Keisler et al. "Measurements of sub-degree B-mode polarization in the cosmic microwave background from 100 square degrees of SPTpol data". In: *The Astrophysical Journal* 807.2 (2015), p. 151.

[44] Samuel Pierpont Langley. "The bolometer and radiant energy". In: *Proceedings of the American Academy of Arts and Sciences*. Vol. 16. JSTOR. 1880, pp. 342–358.

[45] Georges Lemaıtre. "126. A Homogeneous Universe of Constant Mass and Increasing Radius accounting for the Radial Velocity of Extra-Galactic Nebulae". In: *A Source Book in Astronomy and Astrophysics, 1900–1975*. Harvard University Press, 2013, pp. 844–848.

[46] JS-Y Leung et al. "A simulation-based method for correcting mode coupling in CMB angular power spectra". In: *The Astrophysical Journal* 928.2 (2022), p. 109.

[47] John C Mather et al. "A preliminary measurement of the cosmic microwave background spectrum by the Cosmic Background Explorer (COBE) satellite". In: *The Astrophysical Journal* 354 (1990), pp. L37–L40.

[48] Lorenzo Moncelsi et al. "Receiver development for BICEP Array, a next-generation CMB polarimeter at the South Pole". In: *Millimeter, Submillimeter, and Far-Infrared Detectors and Instrumentation for Astronomy X*. Vol. 11453. SPIE. 2020, pp. 189–206.

[49] KA Olive. "Review of particle physics". In: *Chinese Physics. C, High Energy Physics and Nuclear Physics* 40.FERMILAB-PUB-16-568 (2016).

[50] Claudia Patrignani et al. "Review of particle physics". In: (2016).

[51] Arno A Penzias and Robert Woodrow Wilson. "A measurement of excess antenna temperature at 4080 Mc/s." In: *The Astrophysical Journal* 142 (1965), pp. 419–421.

[52] K Rotermund et al. "Planar lithographed superconducting lc resonators for frequency-domain multiplexed readout systems". In: *Journal of Low Temperature Physics* 184.1 (2016), pp. 486–491.

[53] JT Sayre et al. "Measurements of B-mode polarization of the cosmic microwave background from 500 square degrees of SPTpol data". In: *Physical Review D* 101.12 (2020), p. 122003.

[54] JA Sobrin et al. "The design and integrated performance of SPT-3G". In: *The Astrophysical Journal Supplement Series* 258.2 (2022), p. 42.

[55] István Szapudi et al. "Fast cosmic microwave background analyses via correlation functions". In: *The Astrophysical Journal* 548.2 (2001), p. L115.

[56] Satoru Takakura et al. "Measurements of tropospheric ice clouds with a ground-based CMB polarization experiment, POLARBEAR". In: *The Astrophysical Journal* 870.2 (2019), p. 102.

[57] A Van Engelen et al. "A measurement of gravitational lensing of the microwave background using South Pole Telescope data". In: *The Astrophysical Journal* 756.2 (2012), p. 142.

[58] Matias Zaldarriaga and Uroš Seljak. "All-sky analysis of polarization in the microwave background". In: *Physical Review D* 55.4 (1997), p. 1830.